

AD-A119 332

NAVAL POSTGRADUATE SCHOOL MONTEREY CA
AN INVESTIGATION OF ENERGY COUPLING IN VARIOUS ARC SUSCEPTIBLE --ETC(U)

F/G 20/5

JUN 82 R M METHENY

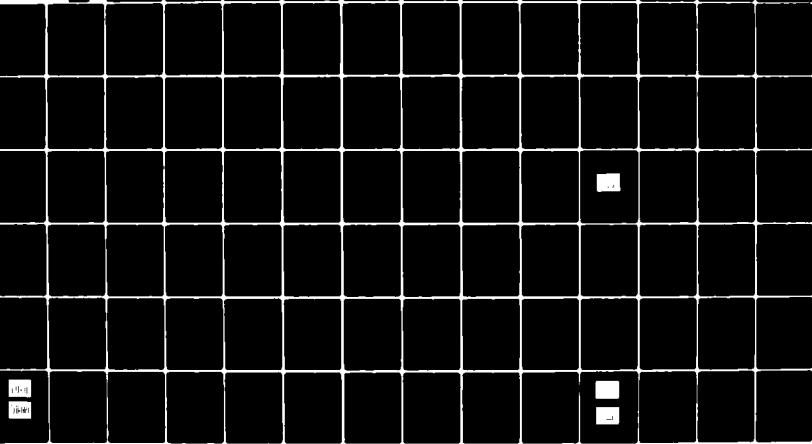
NL

UNCLASSIFIED

Lop 2

ADA

119332



119332
119332

AD A119332

NAVAL POSTGRADUATE SCHOOL
Monterey, California



THESIS

AN INVESTIGATION OF ENERGY COUPLING IN
VARIOUS ARC SUSCEPTIBLE AND RESISTANT
CONDUCTORS

by

Robert Morton Metheny

June 1982

Thesis Advisor:

F. R. Schwirzke

Approved for public release; distribution unlimited.

REPORT DOCUMENTATION PAGE		READ INSTRUCTIONS BEFORE COMPLETING FORM
1. REPORT NUMBER	2. GOVT ACCESSION NO.	3. RECIPIENT'S CATALOG NUMBER
		AD-A119332
4. TITLE (and Subtitle) An Investigation of Energy Coupling in Various Arc Susceptible and Resistant Conductors		5. TYPE OF REPORT & PERIOD COVERED Master's Thesis June 1982
7. AUTHOR(s) Robert Morton Metheny		6. PERFORMING ORG. REPORT NUMBER
9. PERFORMING ORGANIZATION NAME AND ADDRESS Naval Postgraduate School Monterey, California 93940		10. PROGRAM ELEMENT, PROJECT, TASK AREA & WORK UNIT NUMBERS
11. CONTROLLING OFFICE NAME AND ADDRESS Naval Postgraduate School Monterey, California 93940		12. REPORT DATE June 1982
14. MONITORING AGENCY NAME & ADDRESS (if different from Controlling Office)		13. NUMBER OF PAGES 123
		16. SECURITY CLASS. (of this report)
		17a. DECLASSIFICATION DOWNGRADING SCHEDULE
16. DISTRIBUTION STATEMENT (of this Report) Approved for public release; distribution unlimited.		
17. DISTRIBUTION STATEMENT (of the abstract entered in Block 20, if different from Report)		
18. SUPPLEMENTARY NOTES		
19. KEY WORDS (Continue on reverse side if necessary and identify by block number) Energy coupling, unipolar arcing, thermal coupling, momentum coupling, titanium-carbide coatings.		
20. ABSTRACT (Continue on reverse side if necessary and identify by block number) Thermal energy and momentum coupling to four target materials was investigated to determine what effect unipolar arcing had on the coupling process. A review of the various mechanisms of energy coupling to targets irradiated by laser energy, including unipolar arcing, is presented along with some previous experimental results. The experiments were conducted in a		

10^{-6} torr. vacuum using a neodymium-glass laser in the Q-switched mode.

Unipolar arcing was seen to occur on tantalum and SS 304 targets, but not on the TiC and TiN coated targets. Thermal coupling was higher in the arc prone targets, while the listing of materials in increasing order of momentum coupling varied through the intensity range under consideration. Unipolar arcing is proposed as a possible mechanism for the increased thermal coupling. The inability to determine accurately the amount of target material removed by the unipolar arcing process prevented any definitive statement of its effect on momentum coupling.

Approved for public release; distribution unlimited

An Investigation of Energy Coupling in Various
Arc Susceptible and Resistant Conductors

by

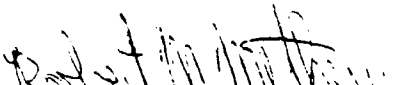
Robert Morton Metheny
Captain, United States Army
B.S., U.S. Military Academy, 1974

Submitted in partial fulfillment of the
requirements for the degree of

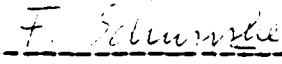
MASTER OF SCIENCE IN PHYSICS

from the
NAVAL POSTGRADUATE SCHOOL
June, 1982

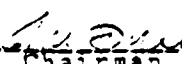
Author:


Robert Morton Metheny

Approved by:


F. Johnson Thesis Advisor


R. L. Berger Second Reader


C. D. Stumpf Chairman, Department of Physics


William M. Tolles Dean of Science and Engineering

ABSTRACT

Thermal energy and momentum coupling to four target materials was investigated to determine what effect unipolar arcing had on the coupling process. A review of the various mechanisms of energy coupling to targets irradiated by laser energy, including unipolar arcing, is presented along with some previous experimental results. The experiments were conducted in a 10^{-6} torr. vacuum using a neodymium-glass laser in the Q-switched mode.

Unipolar arcing was seen to occur on tantalum and SS 304 targets, but not on the TiC and TiN coated targets. Thermal coupling was higher in the arc prone targets, while the listing of materials in increasing order of momentum coupling varied through the intensity range under consideration. Unipolar arcing is proposed as a possible mechanism for the increased thermal coupling. The inability to determine accurately the amount of target material removed by the unipolar arcing process prevented any definitive statement of its effect on momentum coupling.

TABLE OF CONTENTS

I.	INTRODUCTION	11
II.	BACKGROUND AND THEORY	14
	A. ABSORPTION OF LASER ENERGY INTO MATERIALS . . .	14
	1. Surface Absorption	16
	2. Plasma Absorption	18
	B. THERMAL EFFECTS AND HEAT CONDUCTION	20
	1. Validity of Thermal Conduction Problem . .	21
	2. Solution to Heat Conduction Equation . . .	22
	3. Thermal Coupling Coefficient	25
	4. Previous Experimental Results	26
	C. PLASMA PRODUCTION	28
	1. Production From Vaporized Particles	30
	2. Production From Surface Particles	30
	D. MOMENTUM COUPLING	32
	1. Impulse Loading Processes	32
	2. Previous Momentum Measurements	37
	E. PLASMA-SURFACE INTERACTIONS	42
	1. Mechanisms of Plasma-Surface Interactions .	42
	2. Unipolar Arcing	43
III.	EXPERIMENTAL DESIGN	48
	A. EQUIPMENT	48
	1. Laser System	48
	2. Target Chamber	52
	3. Microscopes	52
	4. Temperature and Measuring Equipment	53
	5. Momentum Measurements	56
	6. Velocity Measurements	56
	B. PROCEDURES	59
	1. Sample Preparation	59
	2. Laser-Plasma Surface Interaction	60
	a. Temperature increases	60
	b. Recoil Momentum	60
	c. Velocity Measurements	61

3. Surface Damage Investigation	62
IV. EXPERIMENTAL RESULTS	63
A. THERMAL COUPLING RESULTS	63
1. Temporal Response	63
2. Thermal Coupling Coefficient	66
B. MOMENTUM COUPLING	81
1. Features of Photographic Results	81
2. Momentum Coupling	84
C. LASER PRODUCED PLASMA MEASUREMENTS	91
1. Oscilloscope Trace Characteristics	91
2. Trace Characteristic Results	93
D. SURFACE DAMAGE	104
1. Arc Resistant Materials	104
2. Arc Prone Materials	107
V. DISCUSSION AND CONCLUSIONS	110
A. RELIABILITY OF RESULTS	110
1. Thermal Coupling	110
2. Momentum Coupling	112
3. Velocity Measurements	113
B. COMPARISON OF ENERGY COUPLING OF TARGET MATERIALS	114
1. Thermal Coupling	114
2. Momentum Coupling and Plasma Pulse Characteristics	114
3. Role of Unipolar Arcing	116
VI. RECOMMENDATIONS	118
LIST OF REFERENCES	120
INITIAL DISTRIBUTION LIST	123

LIST OF TABLES

1. Thermal Coupling Results	80
2. Momentum Coupling Results	90
3. Electrostatic Probe Results.	103

LIST OF FIGURES

1.	Events diagram for laser-target interaction	15
2.	Time dependence of reflectivity.	17
3.	Decreasing reflectivity of metal with increasing irradiance. .	19
4.	Thermal coupling under varying pressure and energy for aluminum. .	27
5.	Thermal coupling of titanium over varying intensities. .	29
6.	Optimum momentum coupling to aluminum.	39
7.	Decreased impulse transferred in vacuum.	40
8.	Decreasing impulse transferred above LSD threshold. .	41
9.	Unipolar arc model.	45
10.	The laser system	49
11.	Typical laser pulse shape	50
12.	Diagram of scanning electron microscope	54
13.	Laser and test chamber arrangement for temperature measurement. .	55
14.	Layout of equipment for momentum measurements. . .	57
15.	Double probe circuit.	58
16.	Typical temperature pulse shape	64
17.	Back surface temperature rise for 30.0 cm. lens . .	67
18.	Thermal coupling of SS 304 targets.	68
19.	Thermal coupling of Tantalum targets.	69
20.	Thermal coupling of TiN coated targets.	70
21.	Thermal coupling of TiC coated targets.	71
22.	Comparison of thermal coupling of all target materials. .	72
23.	Back surface temperature rise for 40.0 cm. lens. .	73
24.	Thermal coupling of SS 304 targets (laser defocused). .	75
25.	Thermal coupling of TiN coated targets (laser defocused). .	76
26.	Thermal coupling of TiC coated targets (laser	

defocused)	77
27. Thermal coupling of tantalum targets (laser defocused)	78
28. Comparison of thermal coupling of all target materials with defocused laser.	79
29. Typical photographs of reflected reference beam. .	82
30. Momentum coupling of TiC coated targets.	85
31. Momentum coupling of TiN coated targets.	86
32. Momentum coupling of SS 304 coated targets.	87
33. Momentum coupling of tantalum targets.	88
34. Comparison of momentum coupling of all target materials.	89
35. Typical traces of probe signals.	92
36. Time of flight for TiC coated targets.	94
37. Time of flight for TiN coated targets.	95
38. Time of flight for SS 304 targets.	96
39. Time of flight for tantalum targets.	97
40. Time of flight for all targets.	98
41. Height of main plasma pulse from various targets. .	99
42. Comparison of temporal length of main plasma pulse from various targets.	100
43. Comparison of time of flight for fast plasma pulse from various targets.	101
44. Comparison of heights of fast plasma pulse from various targets.	102
45. Typical surface damage to TiC coated targets. . .	105
46. Typical surface damage to TiN coated targets. . .	106
47. Typical surface damage to SS 304 targets.	108
48. Typical surface damage to tantalum targets.	109

ACKNOWLEDGEMENTS

I wish to sincerely thank Technician Robert Sanders for his invaluable assistance in the Plasma Laboratory. He patiently explained the operation of all equipment, maintained it, and consistently obtained whatever supplies or diagnostic equipment required. Tom Kellogg deserves a similar note of thanks for his assistance in the Materials Science Laboratory. I also appreciate Professor Schwirzke's advice and guidance throughout the project.

My wife Linda, and children, Daniel and Rebecca, are also to be thanked for their patience with my absence and lack of attention during this project.

I. INTRODUCTION

The study of the interactions of a laser-produced plasma and various surfaces is receiving intense research from many disciplines. High energy laser technology has high potential in space and weapons applications and the inertial confinement fusion program. In both of these applications, the intense laser radiation rapidly forms a plasma above the surface of the target material. The problem then becomes one of plasma-surface interactions.

The need for alternate sources of energy makes the efforts for controlled thermonuclear fusion especially important. In the magnetic confinement fusion program, a continuing problem is the interaction of the hot plasma with the containment vessel. The containment vessel itself eventually erodes, but the immediate problem inherent in achieving the Lawson Criteria is the contamination of the plasma by wall material, resulting in radiation losses from high atomic number particles, cooling the plasma.

Several different processes can lead to this contamination. Sputtering [1] occurs when D, T, or He ions and neutrons strike the surface resulting in a collision cascade with the lattice atoms. These collisions often impart

sufficient energy to exceed the binding energy. Absorption of radiant heat can also lead to desorption and simple evaporation of the surface material into the plasma. Both of these mechanisms are fairly well understood. Another reaction which has been shown to cause significant contamination in DITE and Russian Tokamaks [2] as well as the PLT, LSX, and Macrotor Tokamaks [3] is unipolar arcing. This process was first described in 1958 [4] and has received considerable attention since then with the Schwirzke-Taylor model being one of the most recent [5].

The study of this process (which will be described more fully later) has been studied extensively at the Naval Post-graduate School recently. Lautrup and Keville [6] initially examined arcing from a laser produced plasma at NPS and found that TiC coatings were very arc resistant. Barker and Rush, Pyan and Shedd, and Hoover [7-9] all studied the occurrence of arcing on various conductors, semiconductors, insulators, and metallic glasses to further the search for arc resistant materials needed in various applications. Ulrich and Beelby [10] examined the actual mechanisms that lead to the initial breakdown and arc initiation on a material.

The study in this report dealt with the coupling of energy from the laser produced plasma to surfaces of SS 304,

thin TiC and TiN coated surfaces and Tantalum sheets and foil. Titanium coatings have proven to be arc resistant whereas arcing has been observed on the other surfaces. Research was performed to determine if this arcing process affected the amount of energy which was absorbed by the target or carried away as momentum by the blow-off plasma material. A neodymium-glass laser was operated in the Q-switched mode and fired into a vacuum chamber (10^{-6} Torr) containing the suspended targets. Thermal energy was measured using a thermocouple placed on the back surface of the target and measuring the temperature increase after laser interaction. Momentum coupling was examined using a simple pendulum device and photographic techniques. Further research on the blow-off material was performed using a dual-tipped electrostatic probe placed in the path of the expanding plasma cloud. Optical and Scanning Electron Microscopy were also used to observe the surface damage to the targets.

II. BACKGROUND AND THEORY

Coupling of laser energy to targets is a problem which has wide applications, both in the laser fusion program and in weapons and related military technology applications. The problem can be divided into coupling of laser energy onto materials and plasma-surface interactions after the laser has produced a plasma. Figure 1 is an events diagram of some of the occurring interactions. There is, of course, an overlapping of these interactions and no comprehensive model covering all materials, energy densities, pulse lengths, and ambient coditions has yet been forthcoming. The effect of unipolar arcing, one of these interactions, on energy coupling to a surface involves many processes which must be considered.

A. ABSORPTION OF LASER ENERGY INTO MATERIALS

As Figure 1 illustrates, the initial energy losses actually occur before the laser energy impinges on the target. Under laboratory conditions, however, atmospheric losses are negligible and reflection from optical surfaces is accounted for in the laser energy measurements.

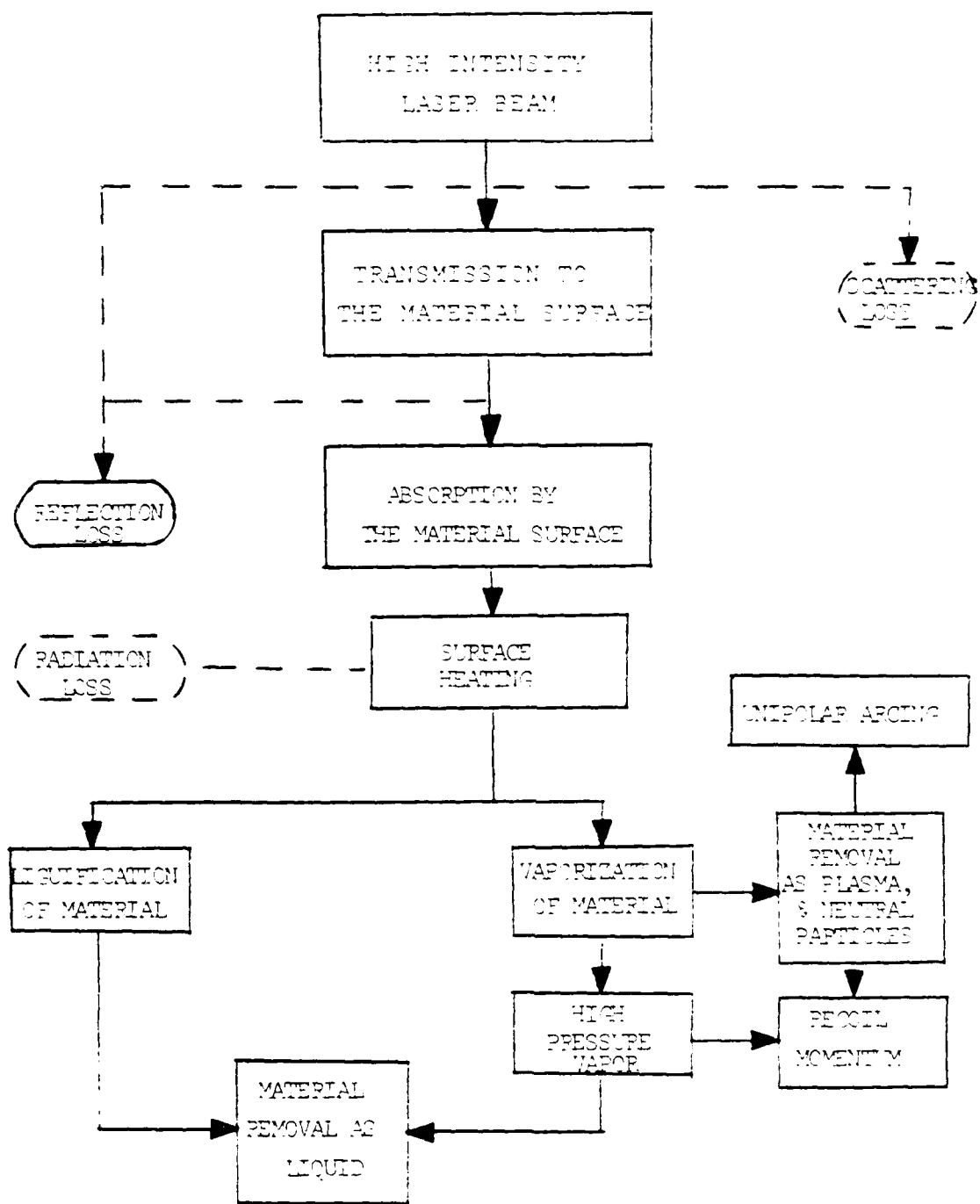


Figure 1. Events diagram for laser-target interaction. Dotted boxes are considered negligible or do not contribute to the study at hand. For simplicity, feedback mechanisms between processes are not included.

1. Surface Absorption

The first process to examine in accounting for the incident radiation is the absorption of the laser energy on the target surface. The atomic level process will be cited under thermal effects. Optical absorptivity can be expressed by $A = 1 - R - T$ where R is the reflectivity and T is the transmissivity, which is zero for the metal targets under consideration. Maxwell's wave equation for EM waves incident upon a conductive medium can be solved to show that:

$$R = \frac{(n-1)^2 + k^2}{(n+1)^2 + k^2} \quad (1)$$

where n is the index of refraction and k is the extinction coefficient. Schriempf [11] shows that n and k are functions of the incident wave frequency, the electron effective mass, the DC conductivity of the material, and the free electron concentration, the latter two having a temperature dependence.

Chun and Rose [12] demonstrated this temperature dependence with experiments on copper with 1.06 micron radiation. The time vs. reflectivity graph in Figure 2 shows a sharp drop in reflectivity as the surface temperature rises

REFLECTANCE VS. TIME

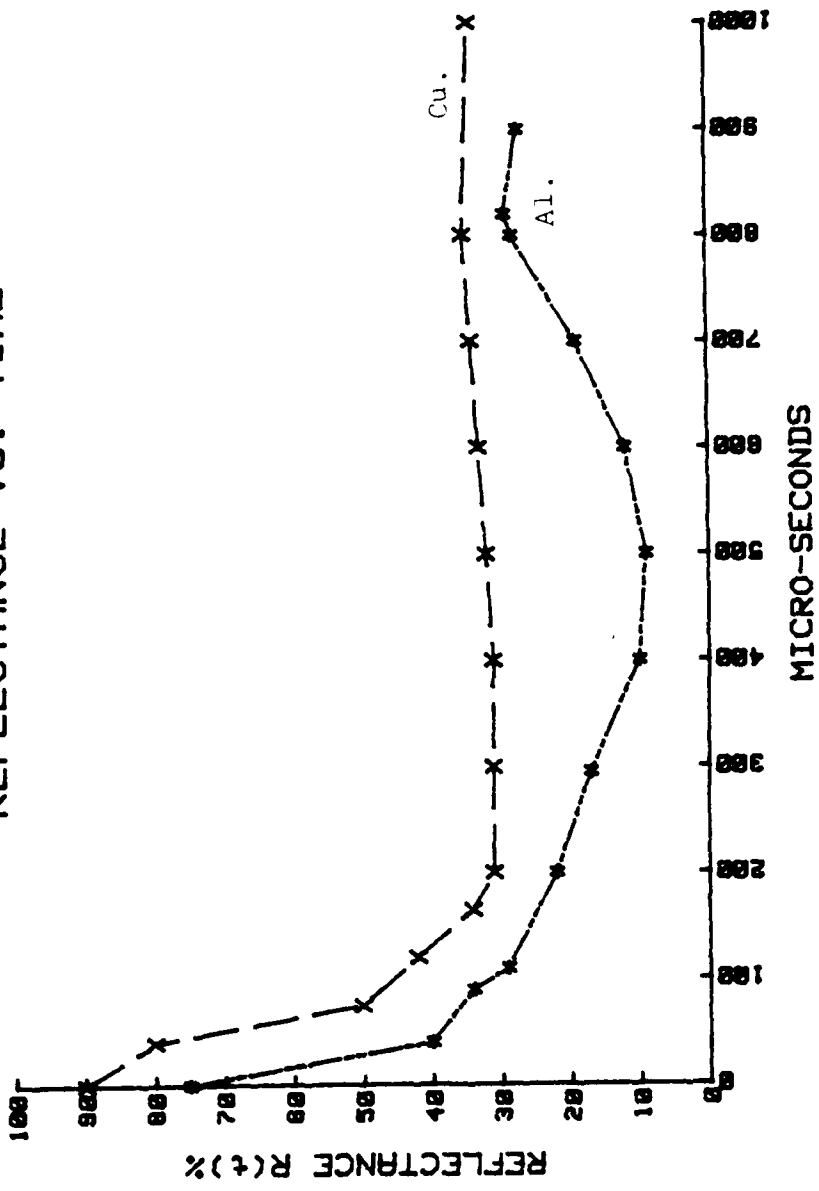


Figure 2. Time dependence of reflectivity. Incidence on aluminum and copper of normal pulsed laser (from reference 12).

to its melting temperature and a leveling as the melting wave propagates into the metal. A further drop has been observed as vaporization begins. Basov et al. [13] shows a similar dependence through a range of irradiances in Figure 3.

Randall and DeGroot [14] show the effect of laser formed craters within an underdense plasma increasing the absorption by approximately 20%. The concave crater walls refract the incident light within the plasma crater, enhancing the resonant absorption. These craters are formed by the variation of the ponderomotive force across the focal region.

2. Plasma Absorption

The absorbed radiation quickly increases T and a plasma is formed above the surface (the production mechanisms will be examined in section C). This plasma also has an absorption coefficient for the incident laser radiation, derived from several inverse-Bremsstrahlung absorption cross sections and optical resonant absorption. Hughes [15] gives an overall absorption for incident light upon a plasma as
(1-R) where:

$$R = \exp \left[-2 \int_{-\infty}^{z_c} a(z) dz \right] \quad (2)$$

REFLECTIVITY DEPENDENCE

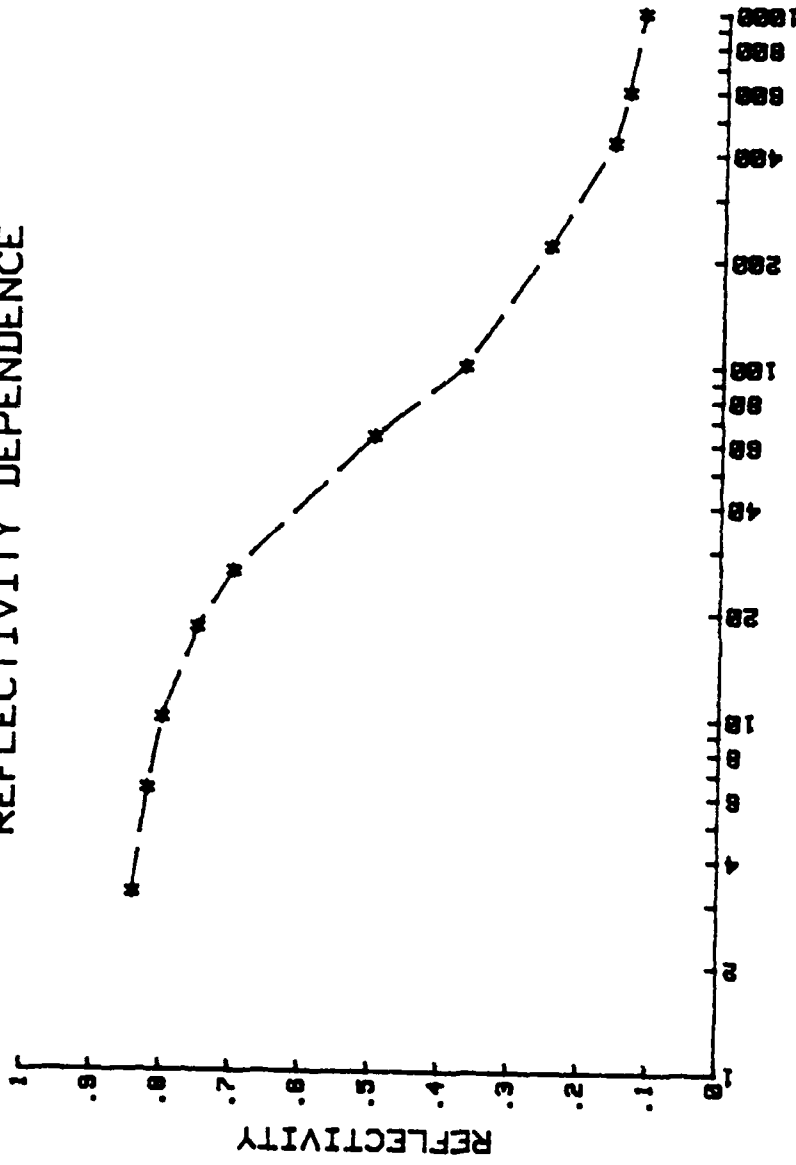


Figure 3. Increasing reflectivity of metal with increasing irradiance
(from reference 13).

and z_c = distance into plasma where electron density causes the plasma frequency to equal laser frequency (cutoff) and reflection to occur (Equation 15).

$a(z)$ = overall absorption function.

This absorption decreases slightly with higher plasma temperatures and densities. Anthes et al. [16] experimentally found that the absorptance within a plasma formed from planar metallic targets varied from 0.9 at 10^{13} W/cm² to 0.8 at 10^{14} W/cm². The absorption increases on the surface with increasing temperature, but decreases slightly within the plasma. Plasma cutoff will be discussed later.

B. THERMAL EFFECTS AND HEAT CONDUCTION

In the previous section, the changing nature of the material reflectivity was examined. The absorption of the laser radiation results in several processes. In the next section, the plasma production mechanisms will be reviewed. The heating of the target and the thermal coupling coefficient will now be presented and the results of some previous workers summarized.

1. Validity of Thermal Conduction Problem

When the intense radiation of the laser strikes the target surface, the optical energy is converted into thermal energy in a distance known as the radiation mean free path, or alternatively, in a distance given as the skin depth, δ defined as:

$$\delta = \sqrt{\frac{1}{c\pi\sigma\mu}} \quad (3)$$

where σ = conductivity of the material

μ = permeability of the material

ν = radiation frequency

For most metals, 1.06 micron radiation has a skin depth of approximately 10^{-6} cm. The Drude-Lorentz free electron model can then be used to describe the thermal response of the material. The excited electrons transfer their energy to the lattice in electron-phonon collisions with a relaxation time of approximately 10^{-13} sec. [17]. With nanosecond and longer pulses, this relaxation time is sufficiently long to consider the problem from a conventional thermodynamic viewpoint. With picosecond pulses other models have to be used.

With such a short skin depth, the initial absorption is essentially a surface phenomenon. The initial equation in considering the heat flow from a surface is the famous Fourier heat conduction equation:

$$\nabla^2 T(\vec{r}, t) = \left(\frac{\rho c}{\vec{K}} \right) \frac{\partial T(\vec{r}, t)}{\partial t} = -\frac{Q(\vec{r}, t)}{\vec{K}} \quad (4)$$

where: T = temperature

ρ = density of the material

c = specific heat of the target

\vec{K} = thermal conductivity tensor

Q = net energy per unit volume per unit time generated by absorbed photons

2. Solution to Heat Conduction Equation

The solution to this equation is quite complex in general, and many simplifying assumptions must be made. This thesis is primarily concerned with the heating of thin targets, and particularly with the temperature rise at the back surface of a target with a vaporizing front surface, under the influence of a short, Gaussian, high power (25 nsec FWHM, 10^9 W/cm²) laser pulse. Several authors treat portions of the problem, but Harrach [18] gives the solution

which best matches the present conditions. Several simplifying assumptions are made:

- a) The thermophysical constants are considered to be constant, independent of temperature.
- b) The calculations describe temperature variations in a single phase state, although the presence of a liquid phase is reflected in the boundary conditions and the averaged thermodynamic properties.
- c) Only longitudinal heat conduction is considered; convection, thermal radiation, and radiant heat flow are neglected. The conductivity tensor can be considered as a scalar constant.
- d) the deposition of laser energy occurs within an infinitesimal depth from the surface, ie. $Q(r,t)=0$.
- e) The blow-off plasma occurring for times greater than the time required for vaporization is assumed to be transparent to the laser radiation.

This last assumption is not valid in the range of power densities considered, but no comprehensive closed forms have been developed which consider the combined effects of initial laser heating, plasma development and cutoff of radiation, and subsequent thermal radiation and energy transport from the plasma to the surface.

Harrach uses the "heat balance integral method" of approximation in his solution. Some characteristic times are necessary in the development of a solution:

- a) the time required for vaporization to begin at the front surface $t_v = (k^2 T_v^2 / 4 \rho c K)$.
- b) the time required for heat to diffuse to the back surface, t_1 , on the order of $l^2 K / \tau^2$ where l is the thickness of the material and K is the thermal diffusivity=thermal conductivity/(density x specific heat)
- c) the time required for burnthrough to occur at the back surface, t_{BT} .

For $t_1 < t < t_{BT}$ and $t > t_v$, a variable Δt is defined as $\Delta t = 1 - T(l, t) / T_v$, where the vaporization temperature is also the instantaneous temperature of the front surface as it is receding due to vaporization (a Stefan problem). A solution is then given as a power series:

$$\Delta t = \frac{T_v - T(l, 0)}{T_v} \left(1 - \sum_{n=1}^{\infty} A_n (t - t_1)^n \right) \quad (5)$$

where the coefficients, A_n , are complicated functions of K , the absorptivity at T_v , the irradiance at t , density, and the combined latent heats of melting and vaporization.

Again, this solution does not consider the probable cutoff of surface irradiation by a dense plasma or thermal effects from the plasma.

3. Thermal Coupling Coefficient

In actual experimental research many workers are also concerned with the thermal coupling efficiency of the laser radiation to the surface. This is often given as the ratio of the incident laser energy to the energy absorbed thermally in the target. Metz, et al. [19] defines the thermal coupling coefficient as:

$$\alpha = \frac{l c T_m}{E} \quad (6)$$

where l = target thickness

T_m = maximum observed temperature rise at back surface above its initial value.

E = average energy per unit area in the central portion of the laser beam. c = specific heat of target material

This expression has been used over a wide range of incident power densities in which the ratio of laser spot size to target thickness allowed a one-dimensional thermal response.

It does not take into account radiative or convective heat losses from the target or any melting or vaporization of part of its surface. However, mass measurements indicate that energy loss measurements through vaporization and ionization of surface material are small.

4. Previous Experimental Results

Several studies have demonstrated an "enhanced thermal coupling" [20] to exist at fluences above the plasma production threshold. Figure 4 demonstrates this enhanced coupling for aluminum over a fluence and pressure range. At 760 torr., a laser supported absorption wave (LSA, to be discussed more fully in Section D) forms which couples the laser energy to the target more effectively through plasma thermal radiation and conduction. At higher energies, however, this LSA wave quickly separates from the surface, decoupling the energy. Marcus, et al. [21] state that at lower pressures, the expansion velocity of the LSA wave is reduced (apparently due to a decreasing ratio of c_p/c_v), allowing higher coupling coefficients at the increased fluences.

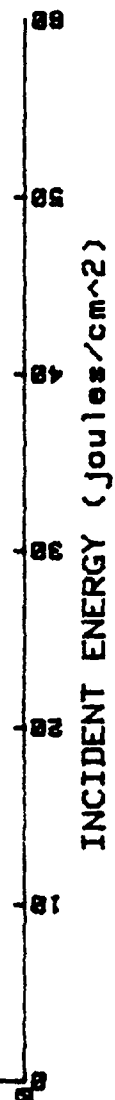
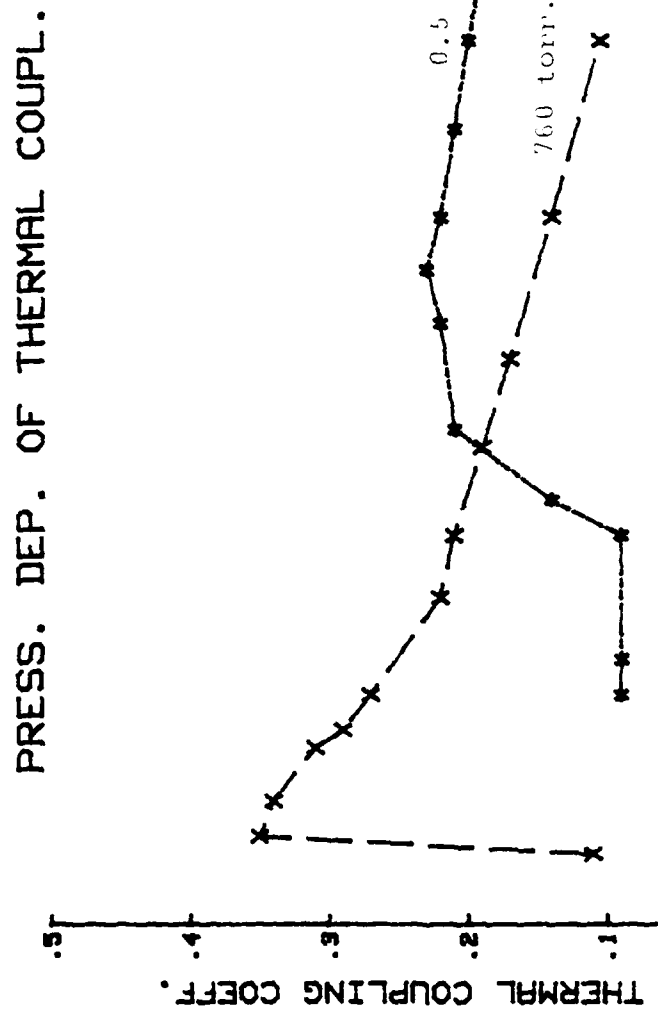


Figure 4. Thermal coupling under varying pressure and energy for aluminum (from Marcus, et al., Journal of Applied Physics, v. 47(7), p. 2967, July 1976).

This curve also has a peak since increasing energies continue to cause plasma separation times to shorten, decoupling the energy from the surface. Maher and Hall obtained similar results in their experiments on 304 stainless steel [22]. Figure 5 shows the results for titanium in a vacuum under 1.06 micron radiation. The slope again indicates the decreasing nature of alpha at higher intensities. McKay, et al. [20] investigated the plasma effects on enhanced coupling in air. By measuring the plasma temperature and assuming a 0.4 metal absorptance of the plasma thermal radiation at 0.22 micron, they concluded that radiation alone was insufficient to account for the increased coupling. Thermal conduction from the plasma was attributed as making a significant contribution to target heating. Unipolar arc-ing will be addressed later as a mechanism effecting this thermal conduction.

C. PLASMA PRODUCTION

The production of a hot, dense plasma above the target surface takes place through several mechanisms. Either neutral particles can be ejected from the material through vaporization and subsequently ionized or electrons and ions themselves can be emitted from the surface.

TITANIUM THERMAL COUPLING

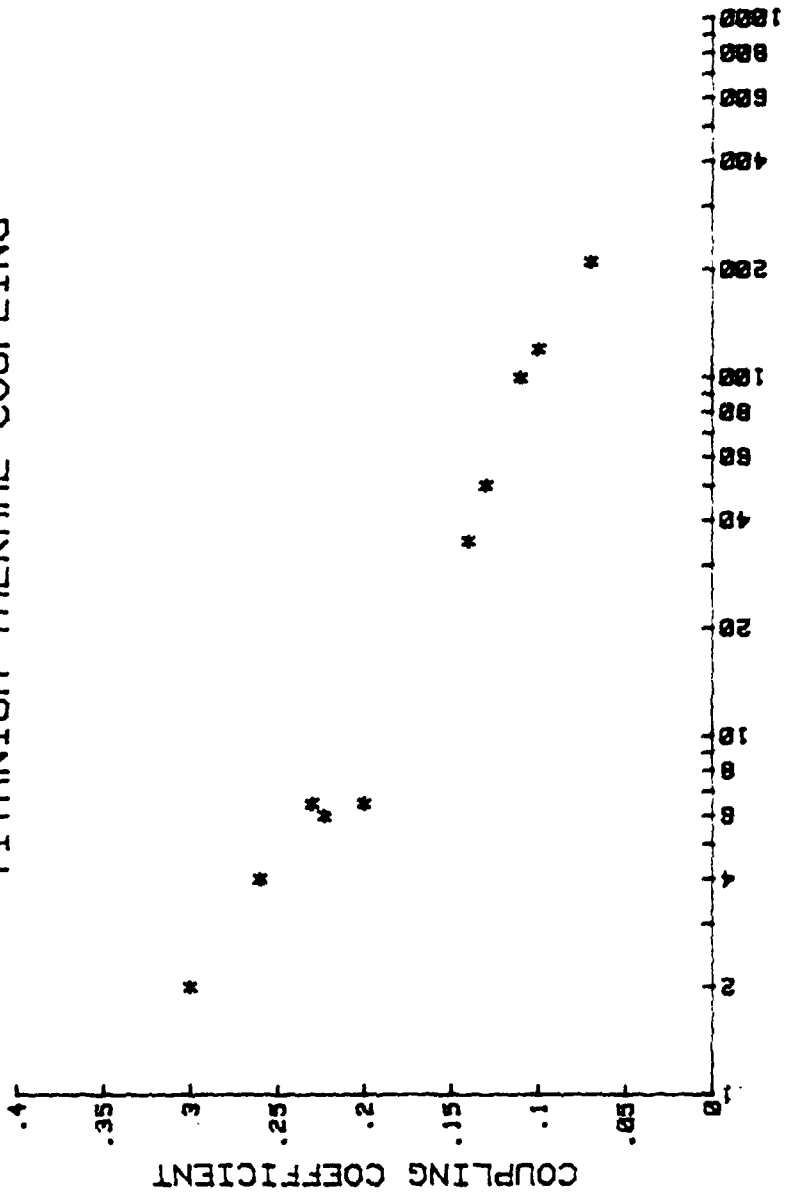


Figure 5. Thermal coupling of titanium over varying intensities
(from reference 30).

1. Production From Vaporized Particles

The Drude-Lorentz model for energy conversion has been used to explain the rapid rise in temperature over a short depth and eventual vaporization of surface material. This vaporized neutral gas will then continue to absorb radiation through the inverse Bremsstrahlung process. Ready [23] gives this absorption coefficient as:

$$k = 3.69 \times 10^8 \left(\frac{z^3 n z}{\sqrt{T} v^3} \right) \left[1 - \exp \left(\frac{-hv}{kT} \right) \right] \quad (7)$$

where z = charge

v = laser frequency.

This process involves the absorption of a photon by an electron in the presence of a heavier ion, further heating the electron.

2. Production From Surface Particles

It should first be stated that IR lasers do not produce photons of sufficient quanta to cause photoionization directly. Developement of X-ray or UV lasers would lead to direct photoionization. Multiphoton absorption, however, is a process involving the absorption of two or more photons by a surface atom. Ready [23] gives the resulting photoelectric current to be an involved expression with dependence

upon the work function, Fermi level, and free electron density of the material; and wavelength and photon density of incident radiation. This effect can exceed the thermionic effect in situations where the pulse length is very short (picosecond) or laser irradiance is relatively low.

In most situations thermionic emission of electrons and ions will be the dominant mechanism. This is a thermal process in which the surface temperature is sufficient for a direct emission of ions or electrons. These currents are expressed by the Richardson-Smith (ions) and Richardson-Dushman (electrons) equations [24]:

$$I_{+-} = A_{+-} T^2 \exp[-\phi_{+-}/kT] \quad (8)$$

where A_{+-} = constants

ϕ_{+-} = positive ion and electron work functions

The same reference also mentions plasma production as a thermomechanical response of the target to the rapid surface heating. A compression stress wave propagates into the surface as a shock wave producing spallation with vaporization and ionization of the emitted material. These and other less significant mechanisms combine to form rapidly (on the order of nanoseconds for Q-switched laser) a hot, dense plasma above the target surface.

D. MOMENTUM COUPLING

The momentum imparted to a target when a high energy laser impinges on its surface is an important consideration when looking at the overall energy coupling. This aspect takes on added importance when it is realized that the entire inertial confinement fusion program rests on the requirement to compress the solid fuel pellet to approximately ten thousand times its solid density through impulse and thermomechanical loading. A review of some of the appropriate processes and results of several previous authors will be given.

1. Impulse Loading Processes

The most obvious process for imparting momentum by a high energy light source is the impulse delivered by the photons themselves. The pressure exerted by a laser can be approximated by the equations:

$$E = hc/\lambda \quad (9)$$

$$\text{and } p = h/\lambda \quad (10)$$

where E = energy/photon

h = Planck's constant

c = speed of light

λ = wavelength of incident light

p = momentum/photon

The number of incident photons for a given energy can be determined by (9), and then (10) can be used to determine the momentum imparted for that pulse. For pulses in the range of 1.0-10.0 joules, this results in momentum on the order of 10^{-3} - 10^{-4} dyne-sec, in good agreement with that obtained by Gregg and Thomas [26]. This will turn out to be several orders of magnitude less than the impulse delivered by other processes.

The primary mechanisms for momentum transfer to the target surface are the recoil momentum from the vaporized and ionized materials flying off the surface, and the pressure exerted by the expanding plasma cloud above the surface. The concepts are straightforward, but the variables of pulse length, energy density, and ambient conditions play a significant role in the value of the coupling coefficient, usually given as the ratio of momentum imparted divided by the incident energy. The plasma production mechanisms and vaporization were covered earlier and we begin here with the material flying off the target surface. This material is in a given state of ionization, approximated by the Saha equation [27]:

$$\frac{n_i}{n_n} = 2.4 \times 10^{15} \frac{T^{3/2}}{n_i} \exp\left(\frac{-U_i}{kT}\right) \quad (11)$$

where n_i, n_n = ion/neutral density

T = temperature

k = Boltzmann Constant

U_i = ionization energy

The pressure from this vaporized portion of the material can be given by [28]:

$$P_v = P_0 \frac{\sqrt{cT_v/3}}{L_v + cT_v} \quad (12)$$

where P_v = pressure

P_0 = power density

c = specific heat

T_v = vaporization temperature

L_v = latent heat of vaporization

The pressure from the blowoff plasma is given as [29]:

$$P_p = \rho v^2 = k_p (a t_p) \phi^{3/4} \quad (13)$$

where ρ = plasma density

v = plasma velocity

k_p, a = constants

t_p = pulse duration

ϕ = light irradiance

The sum of (12) and (13) can then yield the recoil momentum by:

$$M = S \int_0^t (P_p + P_v) dt \quad (14)$$

where S = focal spot area

The degree of ionization will determine the relative importance of the two terms, and will also determine how quickly the plasma density achieves the plasma cutoff density, given as:

$$n_c = \frac{m \epsilon_0 \omega^2}{e^2} \quad (15)$$

where n_c = critical or cutoff density

m = electron mass

ω = radial frequency of radiation

When the plasma achieves the cutoff density, the plasma effectively decouples the laser radiation from the surface. The remainder of the pulse energy is absorbed within the plasma. As we will see later, little additional material is removed through surface interaction with the plasma, but unipolar arcing does provide a mechanism for material removal which will be explained further later.

The expanding plasma cloud now exerts an additional pressure upon the surface. The ambient conditions also play a significant role. Under conditions of >0.1 atmospheric pressure and laser irradiances of 10^5 - 10^6 watts/cm 2 , effects

classified as laser supported absorption (LSA) waves occur [30]. These are classified as laser supported detonation (LSD) waves if the outward expansion is supersonic, laser supported combustion (LSC) waves if subsonic, and plasmatrons if the plasma is at rest. The plasmatron does not separate from the target surface and thus exerts no recoil pressure on the surface. The LSC wave which expands at 1000cm/sec is very complex, has little mass transfer, and no closed hydrodynamic equations exist which describe its impulse effect accurately. Fortunately, most laser experiments have irradiances which produce shock fronts in the LSD wave regime. Application of energy, continuity, and hydrodynamic equations across a shock front indicate that the pressure transferred depends on the $2/3$ power of laser irradiance. Hettche, et al. [31] gives:

$$P = \frac{\rho_0}{\gamma+1} \left[\frac{2(\gamma^2-1) I_0}{\rho_0} \right]^{2/3} \quad (16)$$

where ρ_0 = initial air density

γ = ratio of specific heats of air behind LSD
wave

I_0 = laser irradiance

A similar treatment gives for the coupling coefficient [32]:

$$\frac{I_m}{E_0} = \frac{R_p^2 \rho_0^{2/3}}{2 R_t \gamma_p^{1/3} E_0^{2/3}} \quad (17)$$

where I_m = specific impulse

E_0 = energy per unit area

R_p, R_t = LSD plasma and target radii

At higher power densities (10^{10} W/cm² for 10.6 micron radiation with 10 nsec pulse, for example), air breakdown occurs which effectively decouples energy from the surface.

Hettche, et al. [33] point out that this minimum power density for breakdown is lowered significantly by electron emission from a target surface.

In a near vacuum, we do not have the LSA waves, but the plasma still does exert a pressure given by: $P = nkT = nmv^2/3$, since $mv^2/2 = 3kT/2$, where n = plasma density. This plasma pressure can increase with increasing plasma temperature or density. With a typical density of 10^{21} cm⁻³ and $kT = 100$ ev, we obtain a pressure of 10^5 atmospheres.

2. Previous Momentum Measurements

The above processes combine to make the momentum imparted to the surface a complex function of the target

material properties, the total pulse energy, power density, pulse length, and ambient pressure. Some results of previous workers will be given to present some typical values under varying conditions. Gregg and Thomas [25] used a ruby laser with 7.5 nsec pulse to produce power densities on the order of 10^8 - 10^{10} W/cm² on various materials in vacuum. Figure 6 shows the results of their shots on aluminum. They stated that significant energy is conducted away below the optimum coupling intensity and that the energy above the optimum coupling point goes into further ionization and ion energy. Metz [34] used a 250 psec Nd-YAG pulse of about the same power density, in vacuum and air, on aluminum targets. Figure 7 shows the effect of smaller impulses delivered in vacuum below the coupling optimum. Finally, Hettche, et al. [31], using a Nd-glass laser with 0.1 microsec pulse and 10^7 - 10^9 W/cm² beam in air, demonstrated (Figure 8) that the optimum coupling occurs at the threshold of LSD wave formation, 7.2×10^7 W/cm². Surface shock pressures of 10^3 - 10^4 bars were measured by several workers.

MOMENTUM TRANSFER TO ALUM.

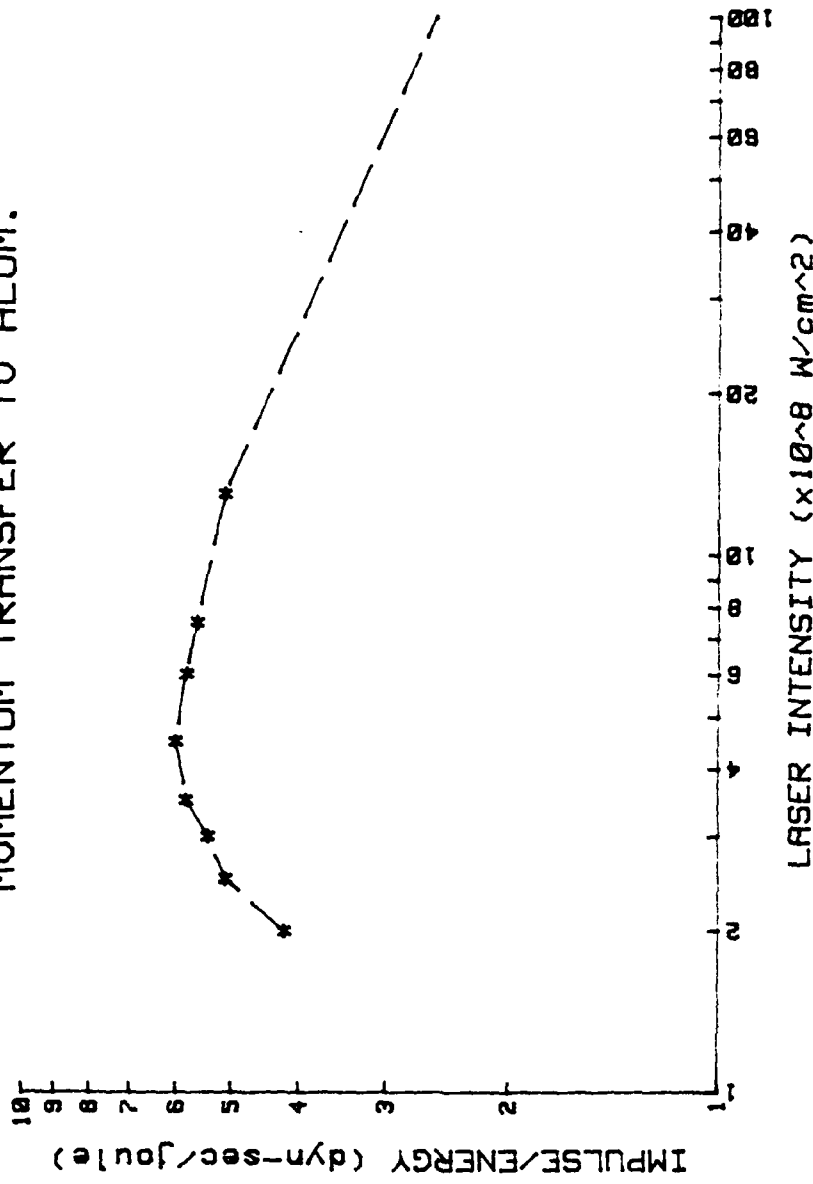


Figure 6. Optimum momentum coupling to aluminum (from reference 25).

IMPULSE VS. INCIDENT ENERGY (JUL.)

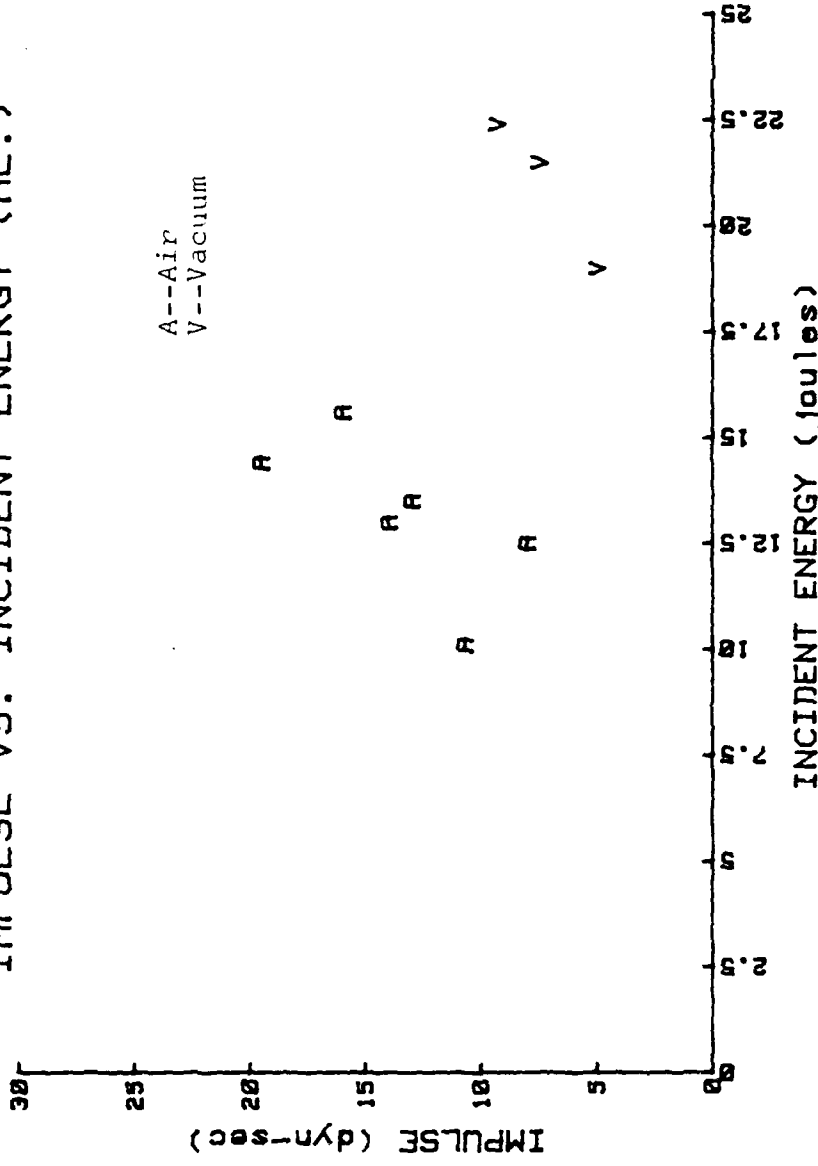


Figure 7. Decreased impulse transferred in vacuum (from reference 33).

COUPLING AT LSD THRESHOLD

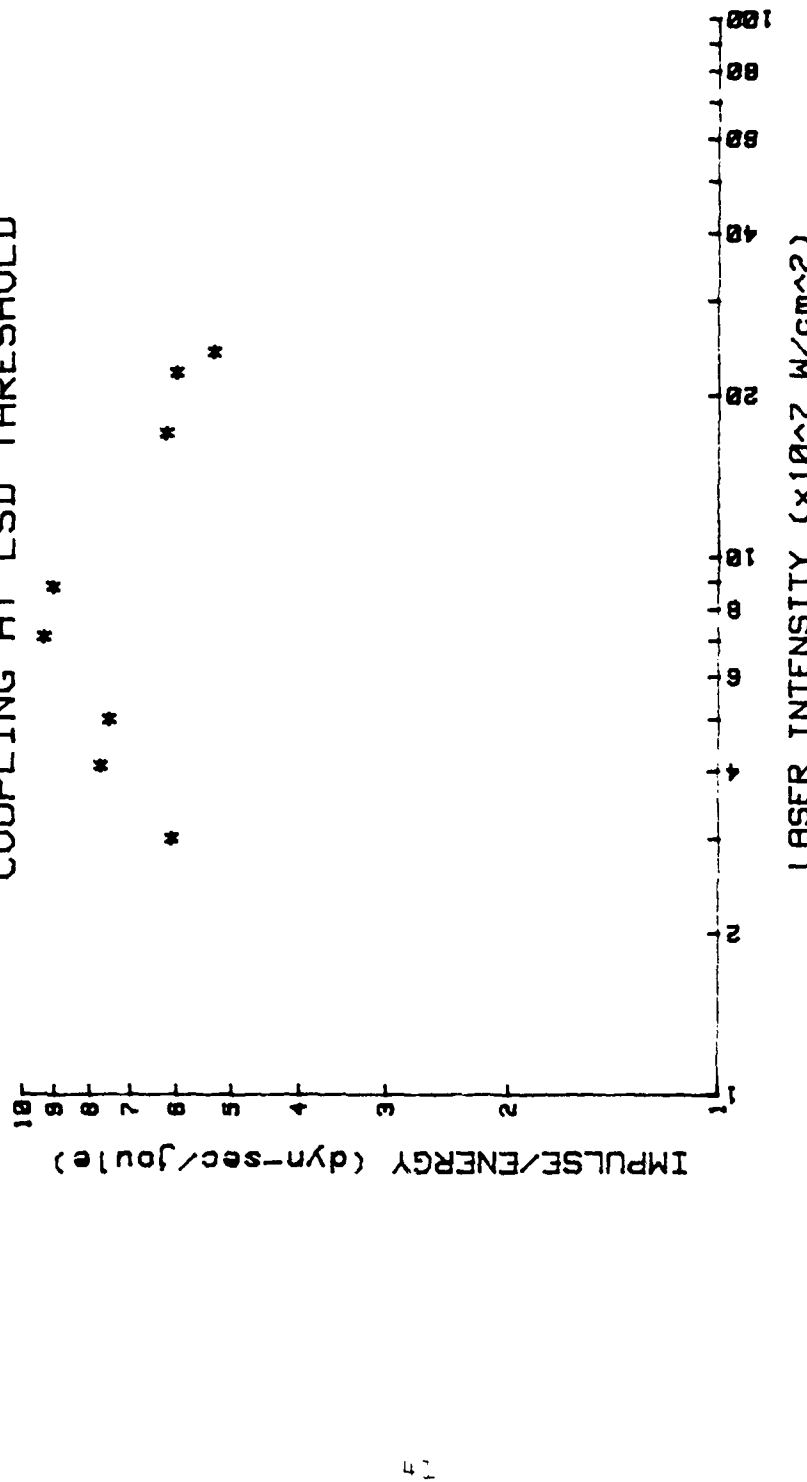


Figure 8. Decreasing impulse transferred above LSD threshold (from reference 30).

E. PLASMA-SURFACE INTERACTIONS

Some of the interactions between a plasma and the surface from which it was produced have already been discussed. Local pressures of several hundred atmospheres can be produced as well as thermal effects from plasma thermal radiation and conduction. The macroscopic effects are especially relevant in the consideration of coupling of laser energy onto a target and subsequent target damage. Several mechanisms are also important on a more microscopic level. These latter plasma-surface interactions have been primarily studied from the viewpoint of their impact on magnetically confined plasma contamination and first wall erosion. This thesis investigated possible links between energy coupling and one of these microscopic interactions, unipolar arcing.

1. Mechanisms of Plasma-Surface Interactions

Evaporation of surface material has already been mentioned as a process in which thermal energy through radiation and conduction from the plasma removes additional surface material. While a major problem, evaporation can be partially controlled through the use of higher melting temperature materials.

The high temperature plasma ions, having considerable velocity, can impart a significant amount of kinetic

energy to the lattice atoms when they strike the material surface. This initiates a collision cascade within the crystal lattice which can knock atoms from the structure if the binding energy is exceeded, resulting in sputtering.

2. Unipolar Arcing

Unipolar arcing has been shown to cause erosion two orders of magnitude greater than sputtering in DITE and Russian Tokamaks [35,36]. Consequently, its effect on plasma contamination has resulted in increased investigation into its initiation, development, and means of prevention. Several workers at NPS have studied different aspects of the problem. Keville and Lautrup [6] first studied the process at NPS, and along with Barker and Rush[7], and Hoover [9], investigated the susceptibility to arcing of several metals, insulators, semiconductors, and metallic glasses. Ryan and Shedd [8] investigated arc initiation and arc motion. Ulrich and Seelby [10] experimentally determined the threshold level of power density for initiation of unipolar arc-ing. These works should be consulted for specific discussions of cited aspects of the phenomenon.

Unipolar arcing was first described by Robson and Thoneman [4]. Schwirzke and Taylor [5] furthered the theory

in 1980. It is their model which is briefly outlined in the following discussion.

Figure 9 from Reference 36 provides a good summary of the individual events of the mechanism. The higher Maxwellian thermal velocity of electrons in a dense plasma results in a higher number density of electrons, n_e , striking a nearby surface than ions, n_i . This leads to a positive potential or sheath in the plasma with respect to the wall. This potential serves to inhibit further electron losses, regulating the charge balance. The sheath has a width proportional to the Debye shielding length [38]:

$$\lambda_D = \sqrt{\frac{kT_e}{4\pi ne^2}} \quad (18)$$

where T_e = electron temperature

$n = n_e = n_i$ = plasma density

The positive plasma potential has a magnitude given by the floating potential:

$$V_f = \frac{kT_e}{2e} \ln\left(\frac{M_i}{2\pi m_e}\right) \quad (19)$$

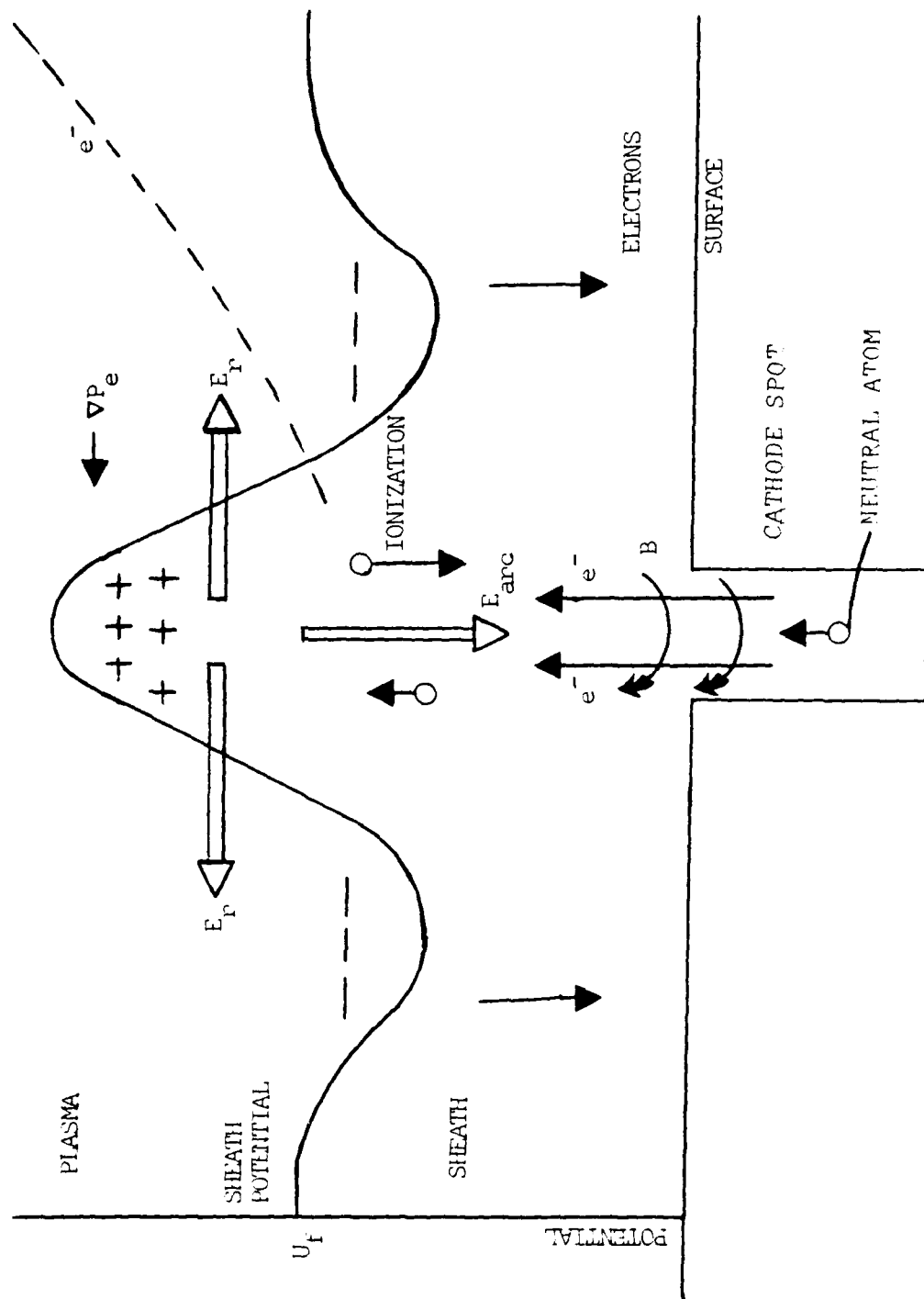


Figure 9. Unipolar arc model.

Two conditions are now necessary for arcing to initiate. First, the floating potential must be high enough to sustain an arc. There must also be a mechanism to close the current loop and maintain the flow of ions and electrons. Schwirzke's and Taylor's model accounts for this by a locally increasing plasma pressure above the arcing site, or cathode spot. Metallurgical inhomogeneities, surface protrusions, or whiskers from processing operations can serve as protrusions to enhance the local electric field strength, increasing the ion flux to the surface. Sputtering can occur, as well as increased neutral evaporation from a higher surface temperature due to increased ion-electron recombination. It can be shown that only about 2% of these neutrals will be ionized within the sheath width, but that is sufficient to increase the local plasma density by three orders of magnitude. The increased density leads to additional ion bombardment enhancing the process. From equation 19, we see that an increasing n_e leads to a decreasing sheath width and, consequently, an increasing electric field to drive the arc, $E_{ARC} = V_f / \lambda_D =$

$$\left(\ln \frac{m_i}{2 m_e} \right) \sqrt{n_e \pi k T_e} \quad (20)$$

The grad-p above the cathode spot leads to a radial electric field, E_r , which decreases the sheath potential in a rim around the arcing site. This enhances the electron flow to the surface, thus providing the required loop for a continuation of the current.

The increased surface heating through recombination, increased material ejection from the arc craters, and increasing plasma pressure are the factors which concentrate the plasma energy towards the arc site. This concentration of plasma energy should enhance the coupling of energy to the target. The significance of this enhanced coupling was the question which motivated the experiments conducted for this research.

III. EXPERIMENTAL DESIGN

A. EQUIPMENT

The three types of experiments performed in this thesis each required a different set of experimental apparatus. The Nd-glass laser, the energy meter, the target chamber, and the microscopy equipment were common to each phase. Temperature measurements also required a thermocouple, meters, and a recorder. Momentum determinations were made using a simple pendulum, He-Ne laser and photographic equipment. The velocity measurements employed a dual-tipped electrostatic probe and high speed oscilloscope. A fuller description of some of the equipment follows.

1. Laser System

A Korad K-1500 neodymium-glass laser with a wavelength of 1.06 microns was used to irradiate the targets. The laser (diagrammed in Figure 10) was operated in the Q-switched mode using a Pockel's cell, yielding a nominal 25 nanosecond pulse width at half maximum (FWHM). As seen in Figure 11, the beam has an approximately Gaussian shape. The output energy varied from 0.2-15.0 joules of energy with an average output energy of about 7.5 joules.

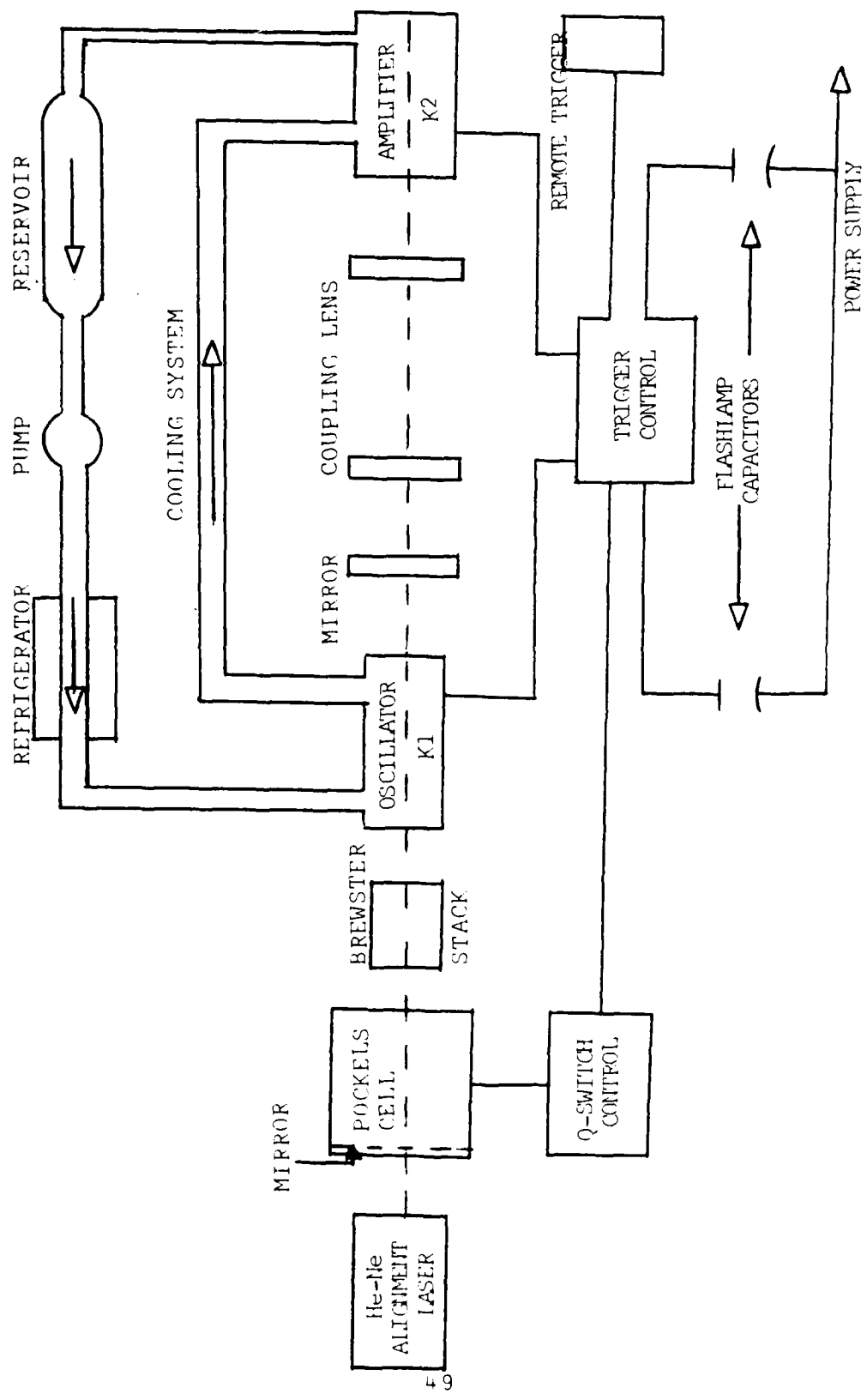


Figure 19. The laser system.

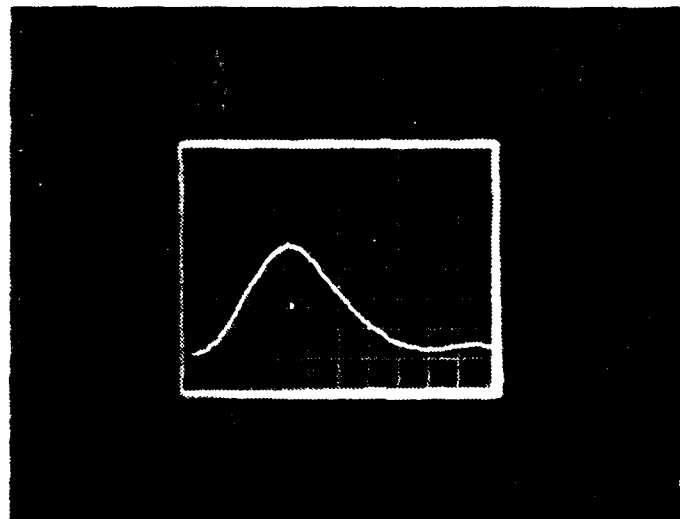


Figure 10. Depth profile of the water surface with a current meter, plotted on a photographic film.

The voltage settings on the Korad laser were not varied, but the output would randomly vary about $\pm 25\%$ during a firing series. Consequently, repetition of a set of measurements at the same energy level could not be accurately performed. The beam was then focused using a 30.0 cm focusing lens for a focal spot size on target of $0.5 \times 10^{-2} \text{ cm}^2$. The beam was also focused using a 40.0 cm lens giving a spot size of 0.2 cm^2 . The output energy was measured by reflecting 8% of the beam from a beam splitter onto the detector of an RK 3230 Laser Precision Energy Meter. This meter, calibrated to an accuracy of $\pm 4\%$, integrates input power signals from 1.0 nsec-1.0 msec duration and gives a direct readout of the incident laser energy. This reading is then corrected to account for the transmission filters and the reflectivities of incident surfaces. The average power flux is given by:

$$F = \frac{ET}{At} \quad (22)$$

where F = flux given in watts/ cm^2

E = energy read by RK 3230 in joules

T = transmittance of optics and filters

t = 3.0 db pulse width in secs

A = beam focal area in cm^2

More detailed information on the actual operation of the laser can be found in Reference 38.

2. Target Chamber

The target test chamber used in these experiments was fabricated locally of unbaked aluminum and had an internal volume of 12.9 ± 0.3 liters. The chamber could be evacuated using a standard forepump and diffusion pump to a pressure of down to 10^{-6} torr. The chamber had eight access ports around and above the chamber to allow for the insertion of targets and diagnostic equipment. The laser was aligned to an angle of 30 degrees from the normal of the rotatable target holder to allow probes to be placed in the path of the expanding plasma. A diagram of the chamber is included in the discussion of the thermocouples.

3. Microscopes

Both optical and scanning electron microscopes were used in examining the target surfaces. A Bausch and Lomb Balplan stereoscopic optical microscope with available magnification of 100-1000x was used to examine the targets, and by adjusting the calibrated focal micrometer, determine the depth of laser and arc produced craters. A Cambridge Stereoscan S4-10 Scanning Electron Microscope with a range of magnification of 20 to 100,000x was also used to examine the

target surfaces. This device uses secondary electrons to provide excellent resolution and depth of field. A schematic of this device is given as Figure 12. The Princeton Gamma Tech energy dispersive x-ray analyser component of the SEM system was not required during this research.

4. Temperature and Measuring Equipment

Temperature increases at the back surface of the target were measured using copper-constantan thermocouples placed between the target and the target holder. The thermocouples were permanently affixed to the target holder to relieve tension during rotation of the target holder. Figure 13 shows these thermocouples connected through electrical jacks to the chamber exterior where it was connected to a Fluke Digital Thermometer which had a precision of 0.1 ± 0.05 degrees C. The reading could be taken visually or the output coupled to a Honeywell Electronik 193 chart recorder. This recorder could provide a temporal profile of the temperature increase and the subsequent cooling. A second thermocouple was connected to a Doric Trendicator 412A digital thermometer (with the same precision) which could provide simultaneous readings with the first thermometer, but at different locations under the target or target holder.

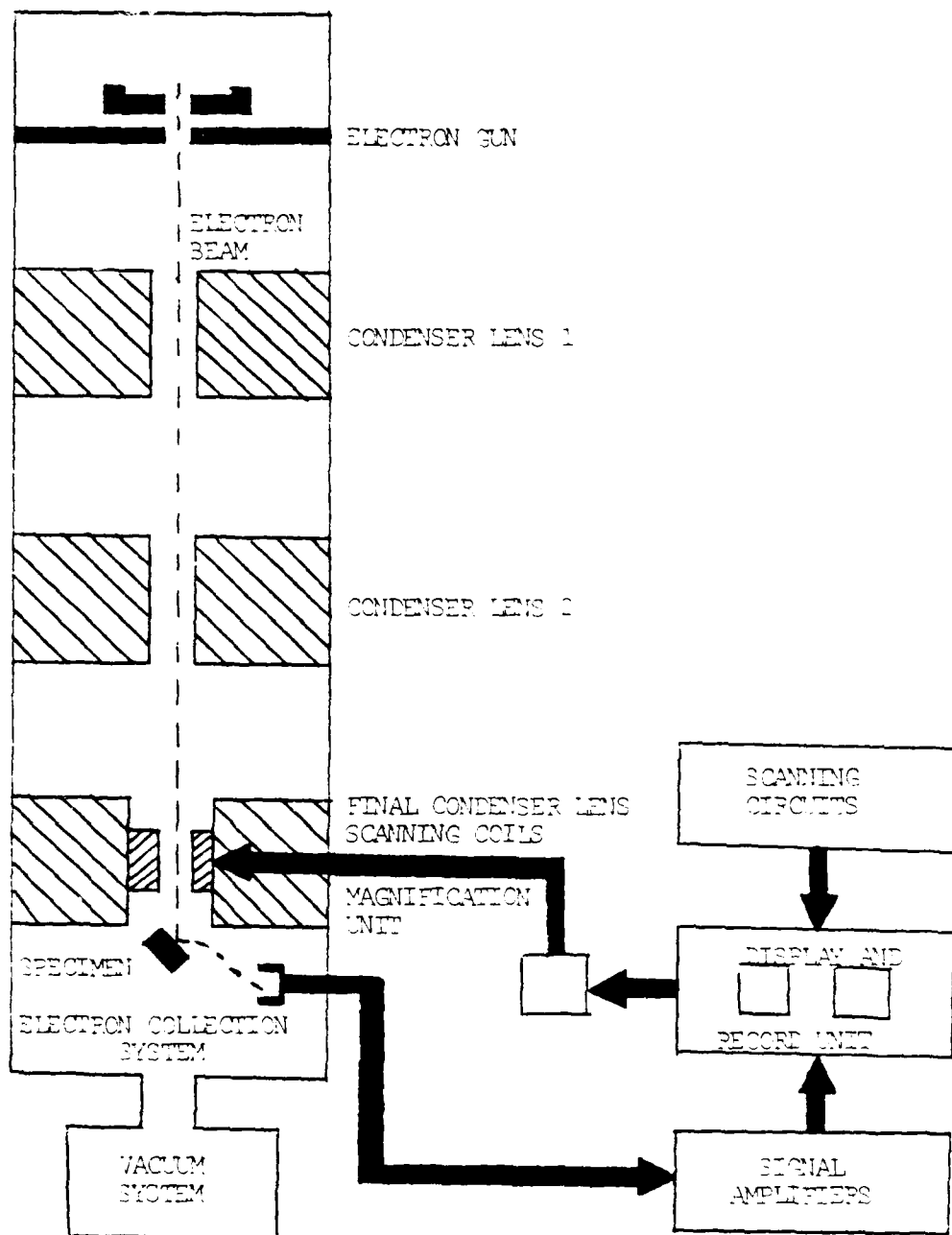


Figure 12. Diagram of scanning electron microscope.

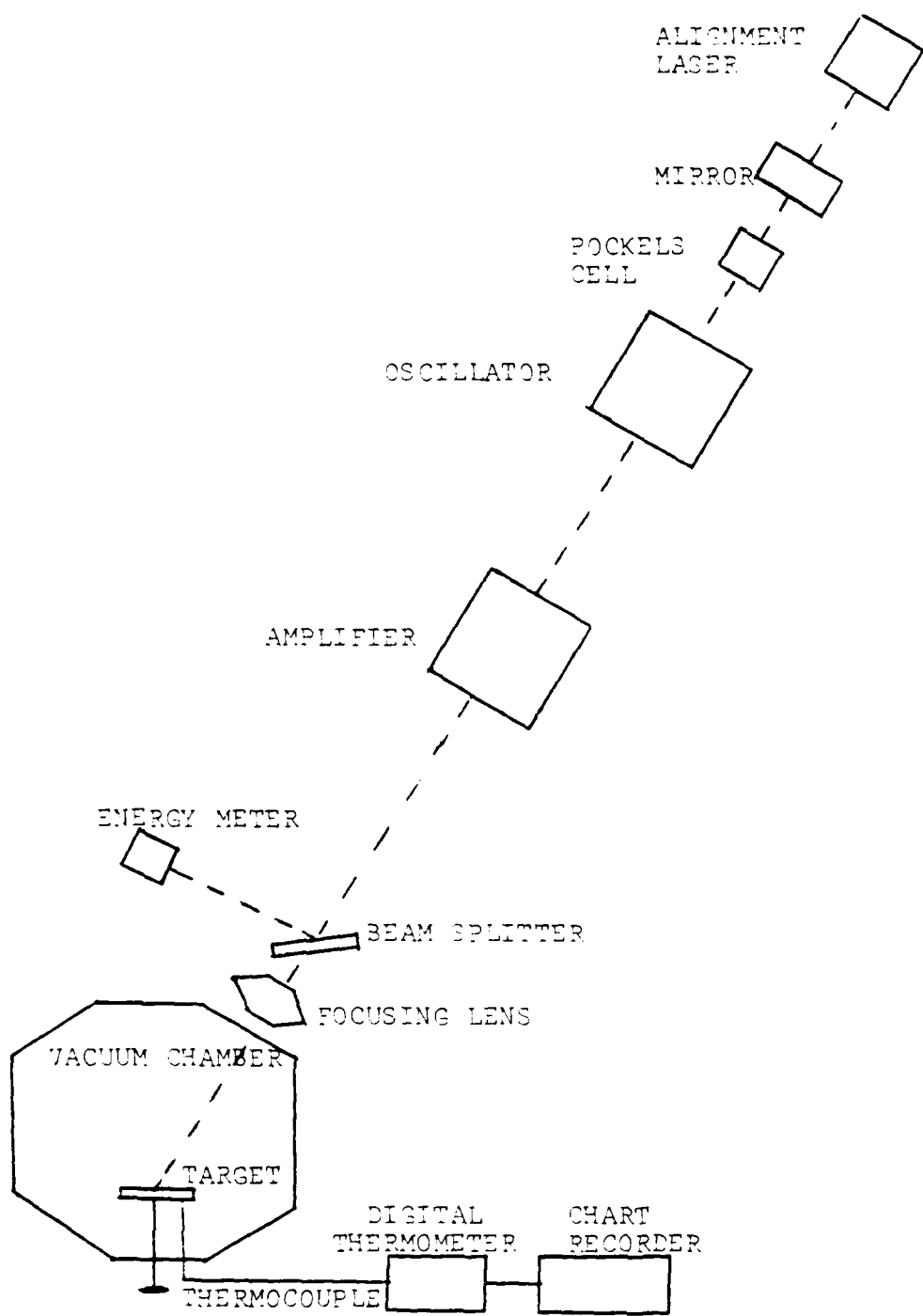


Figure 13. Laser and test chamber arrangement for temperature measurement.

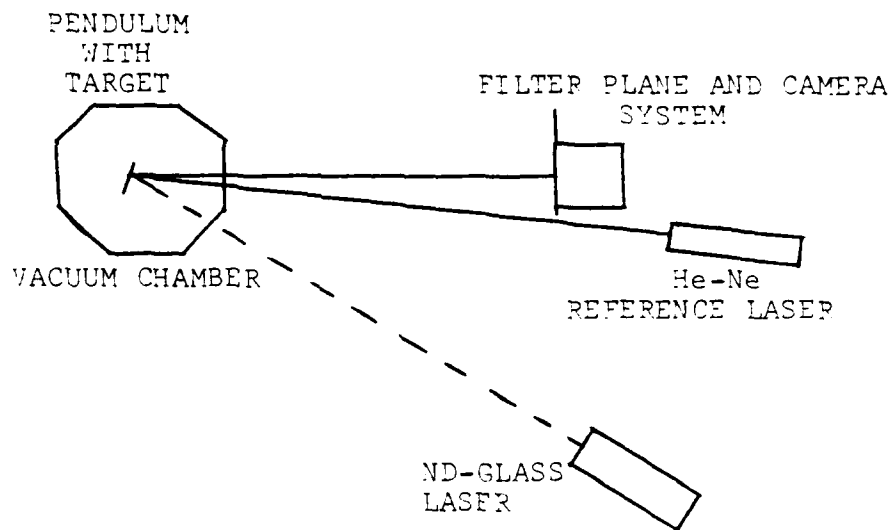
5. Momentum Measurements

A simple metal pendulum was locally fabricated to hold the target and a reflecting mirror. This pendulum was suspended within the chamber from the top port. A Spectra Physics He-Ne laboratory laser provided the reflected beam for these measurements. Standard darkroom filters were used to block out any reflected 1.06 micron radiation from the Nd-glass laser and radiation from the laser produced plasma. A Polaroid CU-5 Camera System was used with a 5 inch oscilloscope hood to record the reflected He-Ne laser beam. Figure 14 shows the arrangement of this equipment.

6. Velocity Measurements

The velocity measurements performed used a floating double tipped electrostatic probe. This probe contains two tungsten electrodes with a diameter of 0.013cm, length of 0.10 cm, and set 0.08 cm apart. The electrodes and related circuitry appears in Figure 15. The electrodes were biased to a voltage of -20.0 volts using a Hewlett-Packard 6200B DC Power Supply. The signal from the probe was then sent to a Tektronix model 7104 oscilloscope with a 7B10 time base allowing measurements down to 2.0 nsec/div, and a 7A24 dual trace amplifier.

TOP VIEW



SIDE VIEW

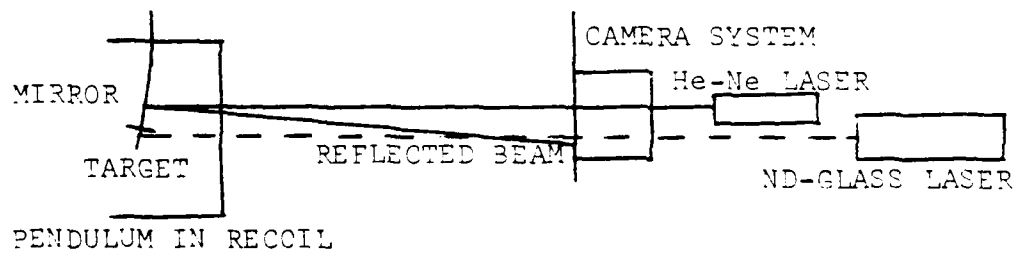


Figure 14. Layout of equipment for momentum measurements.

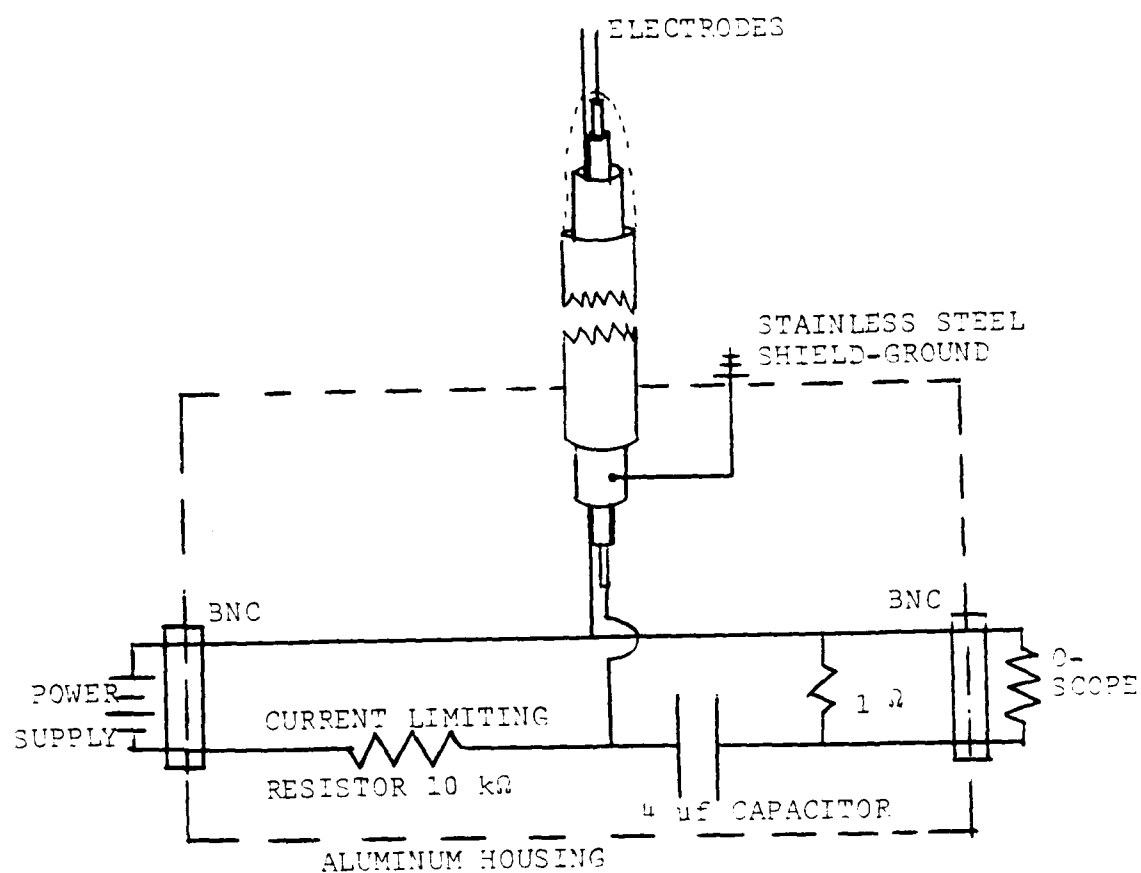


Figure 15. Double probe circuit.

The oscilloscope was triggered by the Nd laser pulse by using a separate Lasermetrics model 3117 power supply and Photodetector. The probe theory and construction techniques are given by Brooks [40].

B. PROCEDURES

The procedures for conducting these experiments can be divided into three phases; sample preparation, laser-plasma surface interaction, and surface damage evaluation. The surface interaction phase can then be further subdivided into experiments to determine the temperature increases, the recoil momentum , and the velocity of the expanding plasma.

1. Sample Preparation

The experiments described herein all use thin sheets of the target material, making use of standard polishing techniques impractical. The TiC and TiN films were deposited on the SS 304 substrates at UCLA using the Activated Reactive Evaporative (ARE) process described by Keville and Lautrup [6]. These sheets were then cut to target size, 13.0 x 13.0 mm, ultrasonically cleaned in acetone, and placed in a dessicant container until mounting in the target chamber. The reverse sides of these sheets were used as the arc prone SS 304 targets to provide targets of comparable thickness and mass for comparison to the titanium-carbide

coatings. The tantalum foil surface was already smooth while the tantalum sheet was rough and somewhat porous and required polishing using standard metallurgical techniques with a final polishing slurry of 0.05 Al₂O₃ to provide a surface suitable for examination.

2. Laser-Plasma Surface Interaction

Different procedures were used in each of the three experiments performed to determine the temperature and momentum coupling.

a. Temperature increases

The thermocouple was centered on the target holder and the target fastened to the holder. The chamber was then evacuated and the temperature recorded after the system had stabilized. The laser was then fired and the temperature profile of the back surface recorded and/or maximum temperature of the readout recorded.

b. Recoil Momentum

A Sartorius model 2403 Electrobalance was used to measure the weight of the target and pendulum target holder. The pendulum was then placed in the vacuum chamber and aligned with the reference beam of the He-Ne laser as illustrated in Figure 14. The chamber was then evacuated and the system allowed to stabilize. The shutter on the

camera system was then opened and the Nd-glass laser fired. The laser radiation produced a blowoff plasma which imparts a recoil momentum to the target and pendulum, causing them to swing. The amplitude of this swing is then measured by the deflection of the reflected reference laser beam on the glass plate as recorded by the camera system. The shutter is closed after several oscillations of the pendulum. All distances are then carefully measured and simple geometry used to determine the amplitude of swing. The target was reweighed and laser energy, as recorded by the photodetector, recorded.

c. Velocity Measurements

The double tipped electrostatic probe was carefully placed within the chamber and positioned 2.0 cm from and normal to the target surface. The chamber was evacuated and the probe biased to -20.0 volts DC. The laser was then fired and the probe response recorded by the oscilloscope's camera system. The oscilloscope is triggered by the laser pulse as detected by the Lasermetrics detector. Distances of laser path and electrical leads are measured to determine the temporal delay of the signal as described by Brooks [40]. Photographs are then analyzed to determine the velocity and relative magnitude of the expanding plasma cloud.

3. Surface Damage Investigation

Selected targets were examined under the optical and scanning electron microscopes without further surface treatment. This surface examination was used to determine the nature of the laser and/or plasma surface interactions, presence and nature of arcing, or other damage phenomenon.

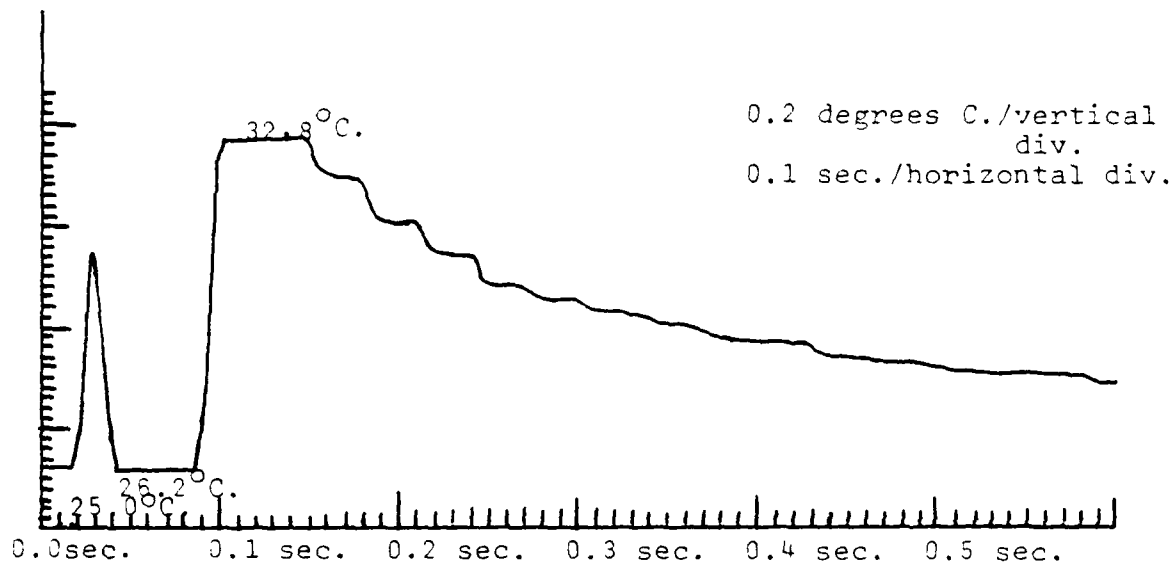
IV. EXPERIMENTAL RESULTS

Approximately 500 laser shots were fired in obtaining 350 data points on the coupling of energy to the target surface of various materials. The results of these interactions will be divided into presentations of the thermal coupling results, momentum coupling results, and examination of the blow-off plasma characteristics. Each of these sections will contain figures of typical data collected, plots of resulting data, and a summarizing table. The last section will contain some scanning electron micrographs of the resulting damaged surface features. A discussion of the results, including problems encountered, will be presented in the next chapter.

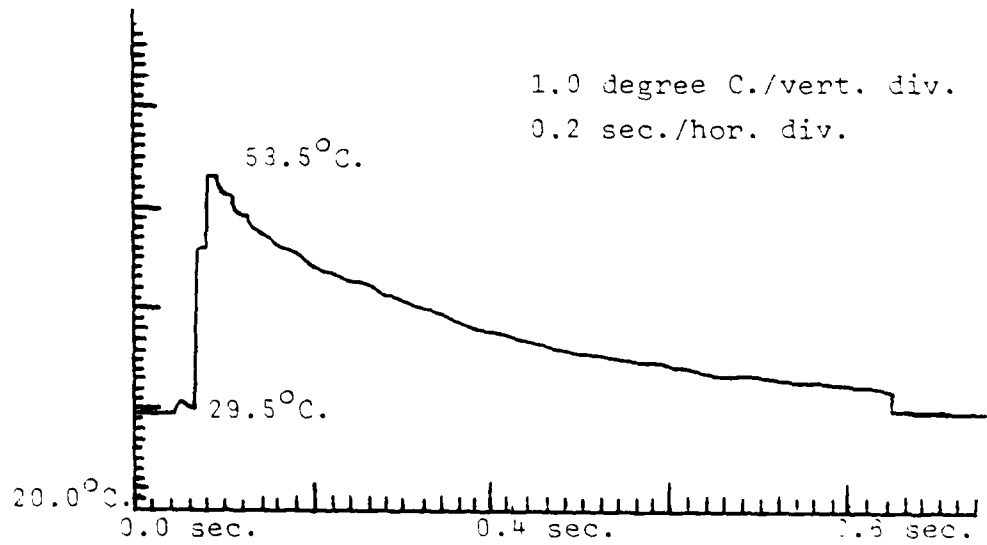
A. THERMAL COUPLING RESULTS

1. Temporal Response

The thermal response on the back surface of the target was used as a measure of the thermal coupling of energy to the target. Typical temporal plots of the temperature are shown in Figure 16. The early spike on each graph was noted on almost all the graphs and it is believed to be a noise signal generated by the initial firing of the laser.



Stainless Steel 304 target struck by 9.34 J. laser pulse



Tantalum target struck by 6.08 J. laser pulse

Figure 16. Typical temp. pulse shape. Reproduction of chart recording of temperature on back surface after laser illumination.

This was substantiated by the fact that a spike was recorded when the recorder was switched to a thermocouple behind a target which was not hit by the laser light. The spike does serve as a rough reference point for when the laser was fired. As expected, there is a brief interval before the temperature rises due to the time required for the heat to conduct through the material. The temperature then rises to its maximum value (with changes ranging from 1 to 20 degrees C.) in less than 0.2 sec. for most cases. The actual laser pulse lasts less than 0.1 microsecond while the plasma separates from the surface after a few microseconds. Hence, there is no heat source after the initial pulse and the temperature begins to decrease quickly. An exponential curve was fitted to several of the graphs, verifying an exponential drop in the back surface temperature. The steps in the graph are apparently due to the digital nature of the Fluke Digital Thermometer rather than the temperature decline itself. Attempts were made to view the thermocouple signal directly on the 7104 oscilloscope. This was unsuccessful as the noise from the line voltage on the unshielded thermocouple leads hid the thermocouple signal. Filtering attempts were also unsuccessful. Readings from the second thermocouple were taken to check the radial conduction of

heat. In each case, readings taken under the securing screws were less than one third the primary readings. The maximum temperature noted by the primary thermocouple was then used in calculating the thermal coupling coefficient.

2. Thermal Coupling Coefficient

The thermal coupling coefficient given in equation 6 was used to calculate the results for the data obtained in this research. The results of the shots using a 30.0 cm focusing lens are plotted in Figures 17-21. A linear regression routine was used to fit a line to the data for each target. Figure 17 shows the relative temperature rise at the back surface of each target while Figures 18-21 are the thermal coupling results. The 30.0 cm lens resulted in damage from the laser-plasma-surface interaction to an area of about 0.116 cm^2 on the surface. Only the lines are plotted in Figures 17 and 22 as the scatter of individual target data overlap a great deal. The lines are not extended significantly beyond the range of initial data. Further discussion of the results is reserved for the next chapter.

A 40.0 cm lens defocused the laser energy somewhat and almost doubled the damaged area to an average size of 0.229 cm^2 . Figure 23 shows the temperature increase on the back surface.

BACK SURFACE TEMPERATURE RISE

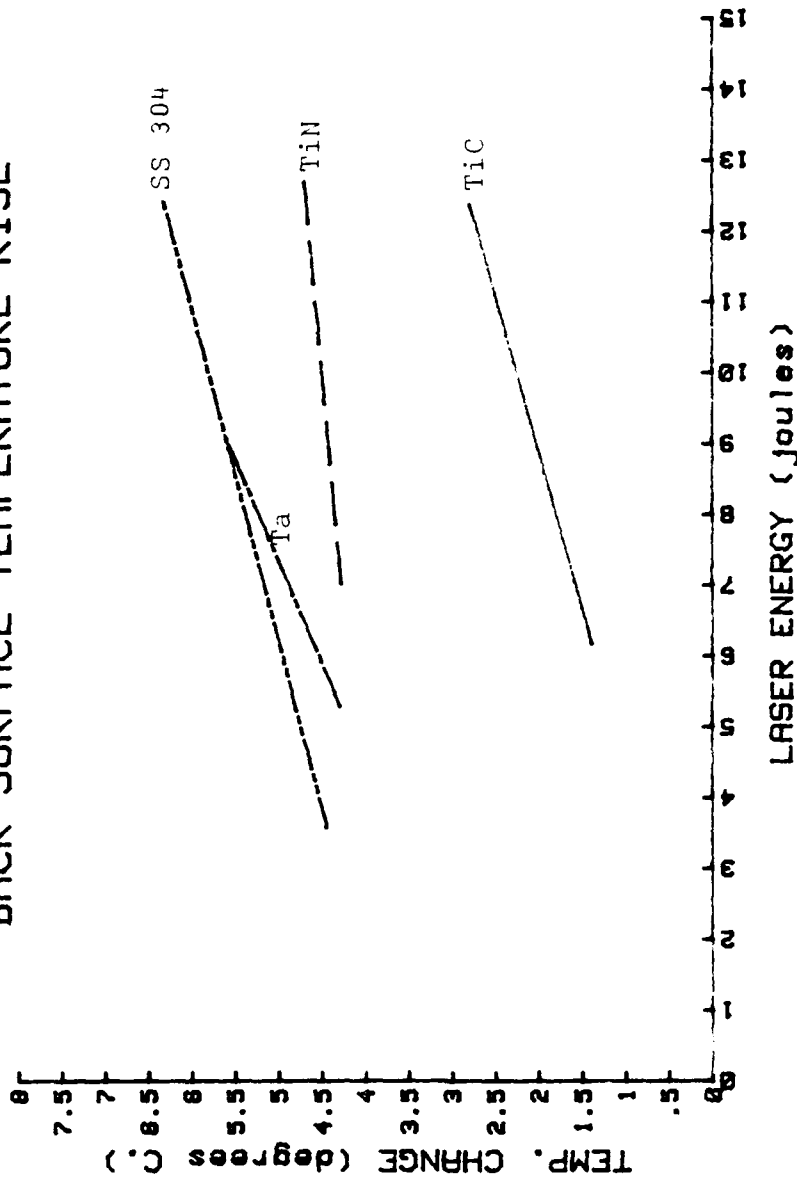


Figure 17. Back surface temperature rise for 30.0 cm. lens.

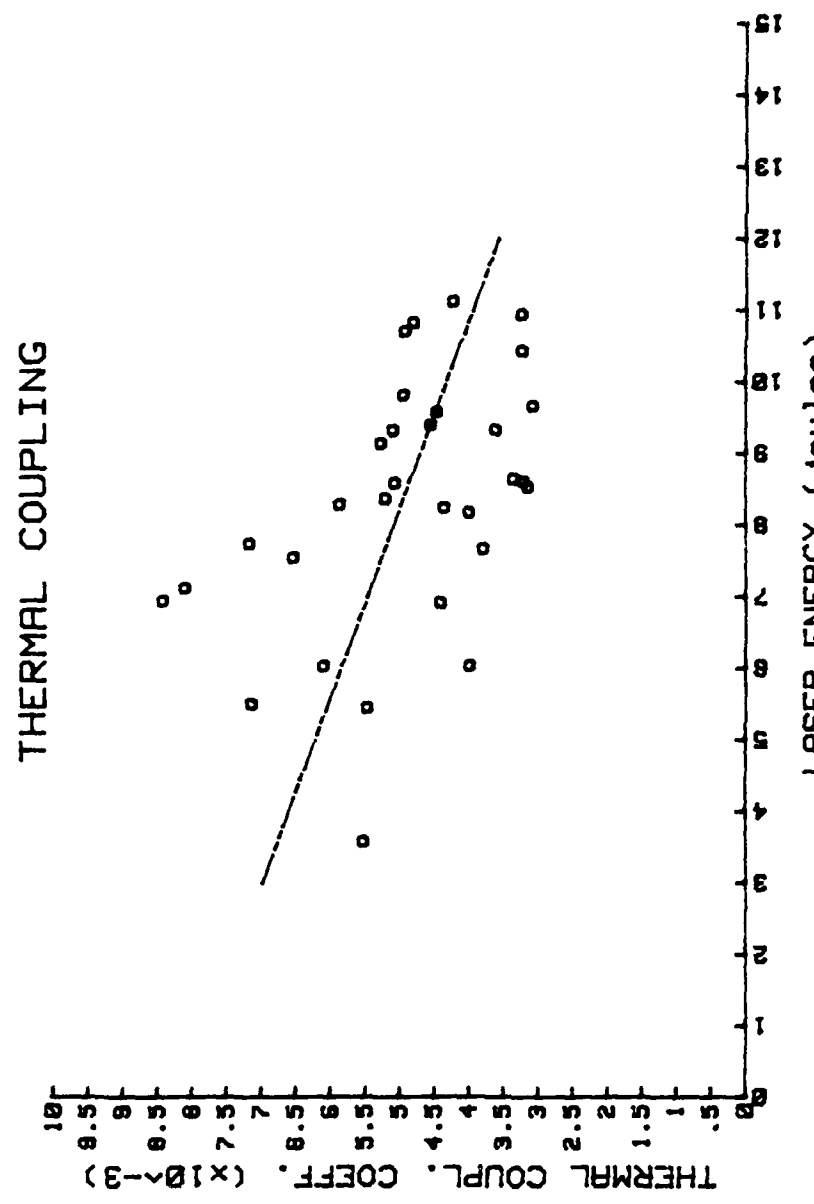


Figure 18. Thermal coupling of SS 304 targets.

THERMAL COUPLING

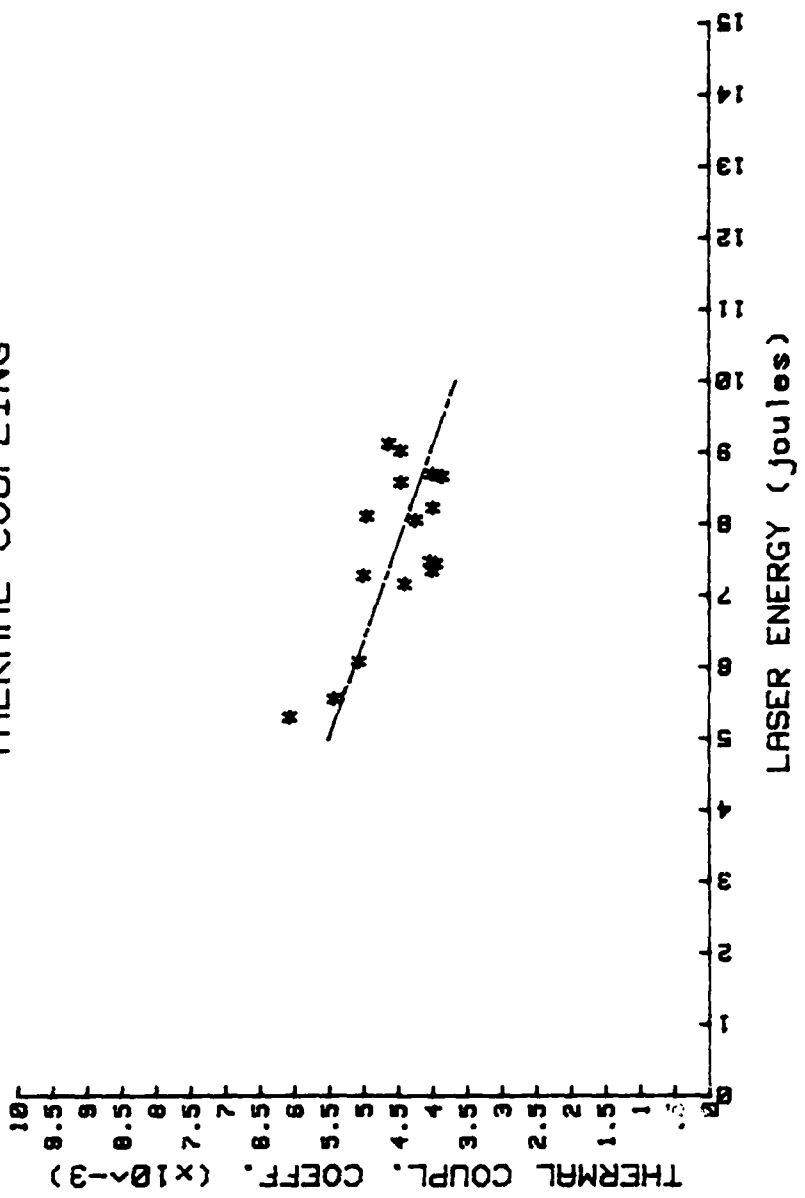


Figure 19. Thermal coupling of tantalum targets.

THERMAL COUPLING

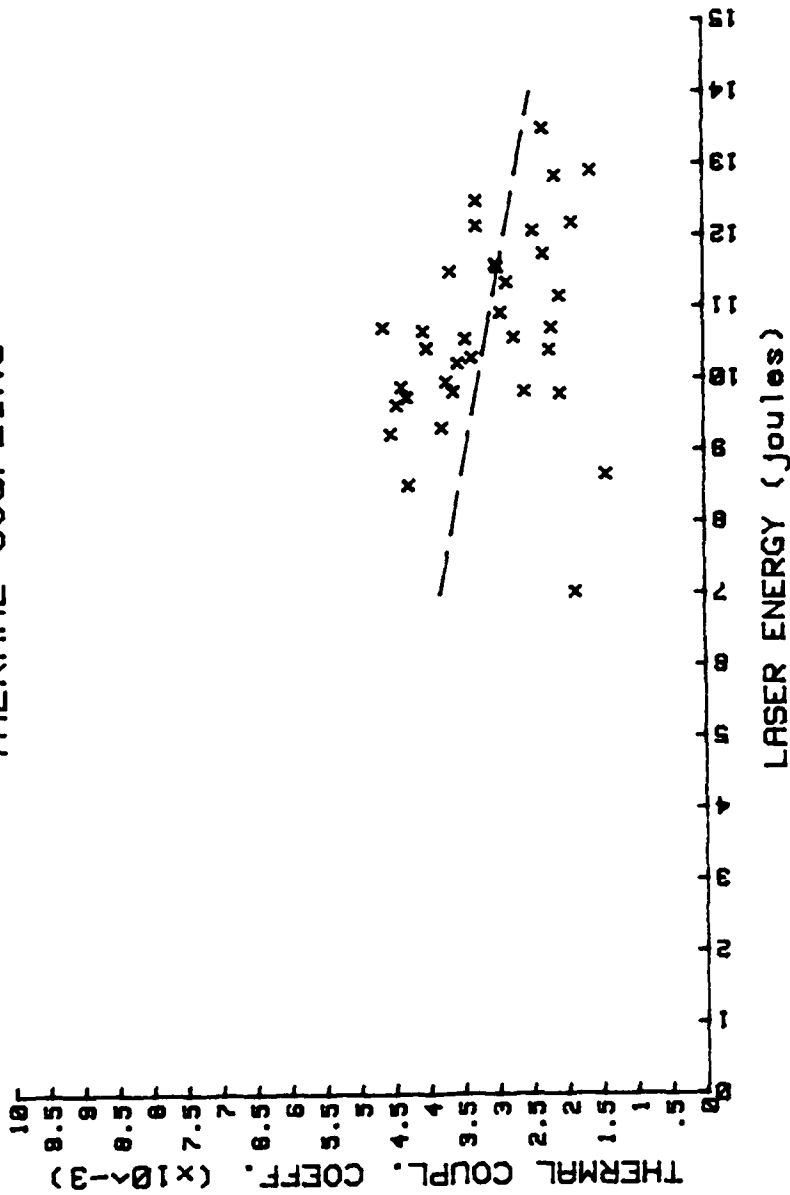


Figure 20. Thermal coupling of TiN targets.

THERMAL COUPLING

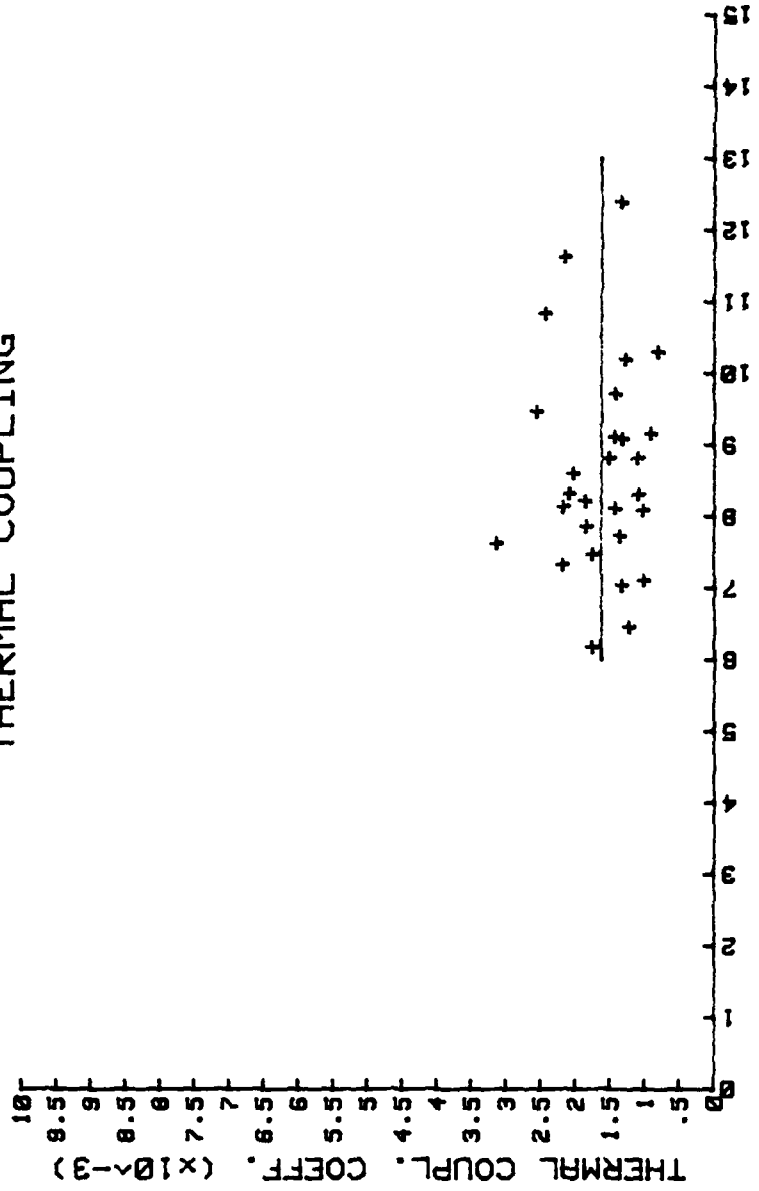


Figure 21. Thermal coupling of TiC coated targets.

THERMAL COUPLING

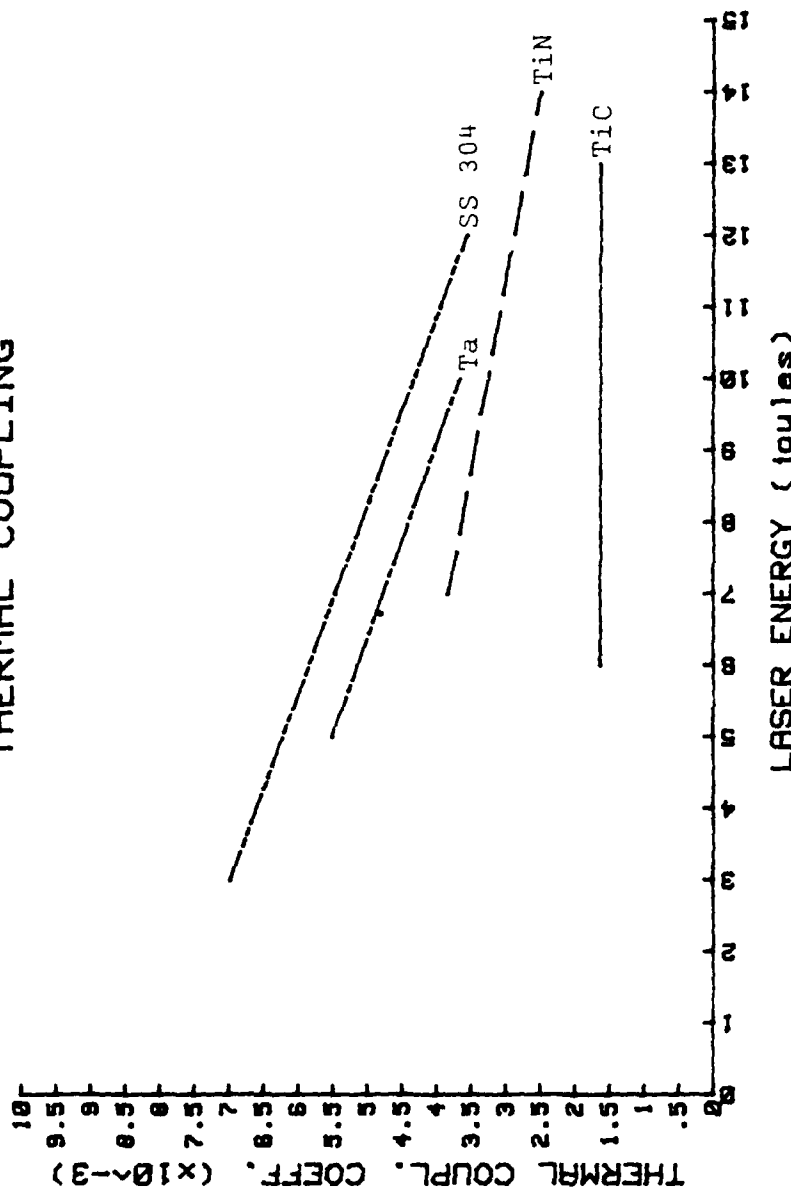


Figure 22. Comparison of thermal coupling of all target materials.

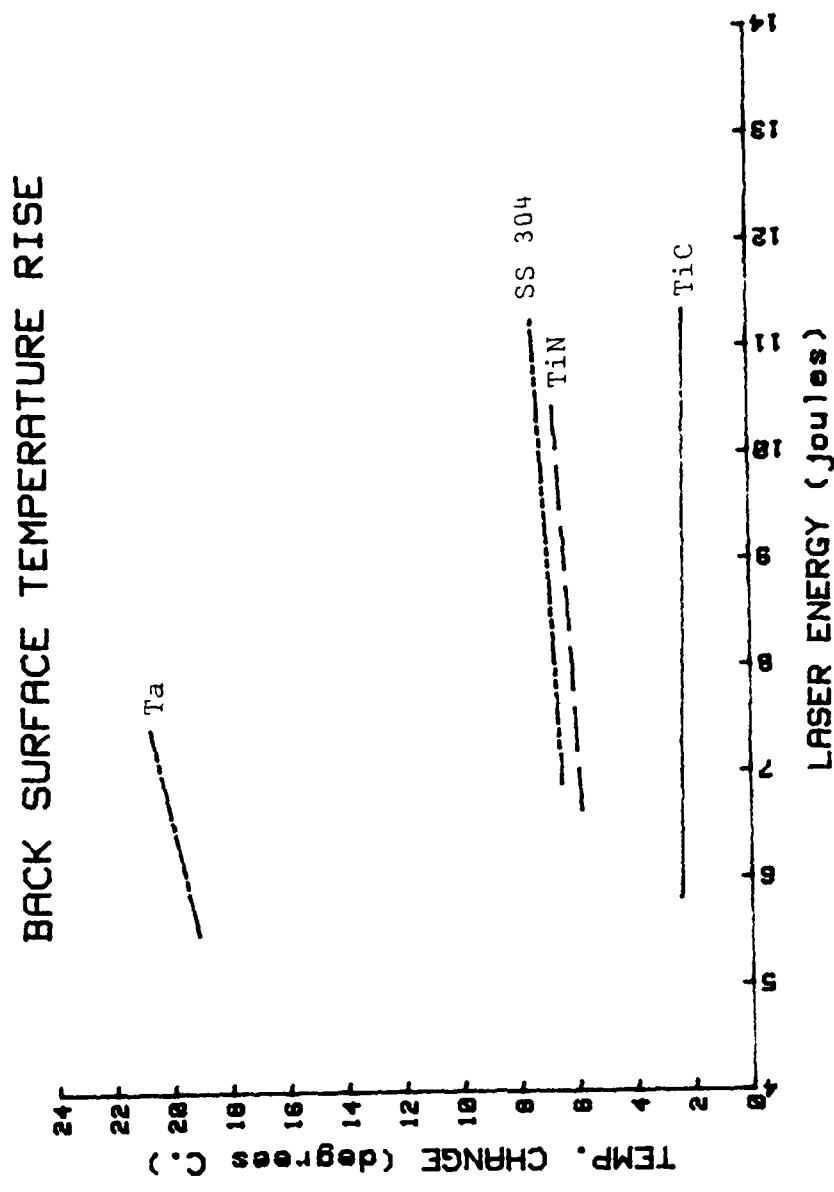


Figure 23. Back surface temperature rise for 40.0 cm. lens.

Figures 24-28 show the coupling coefficients vs. energy for these defocused shots. One possibility for the higher values is the greater likelihood that the thermocouple was under the larger laser damaged area. Centering and aiming errors with the first lens could easily result in the thermocouple being outside the area of direct interaction. Another possibility is that the thermal coupling between the plasma and the surface is actually more efficient at this lower energy density.

Table 1 provides a summary of the results for the thermal coupling measurements for both sets of measurements averaged over the range of energy measurements. Figures 17, 22, 23, and 28 are consistent with each other in the relative positions of lines with the exception of tantalum in the defocused case. Two factors are relevant. There is a smaller data base than with the other materials and the material was only 1/5 as thick. Hence, the change in temperature was almost three times as great as with the other targets (as seen in Figure 23), but there is no reference for the accuracy or response time of the thermometer for increases approaching a rate of 100 degrees per second. Using these results, the calculated coupling coefficient for tantalum is much smaller than for the other materials.

Thermal Coupling

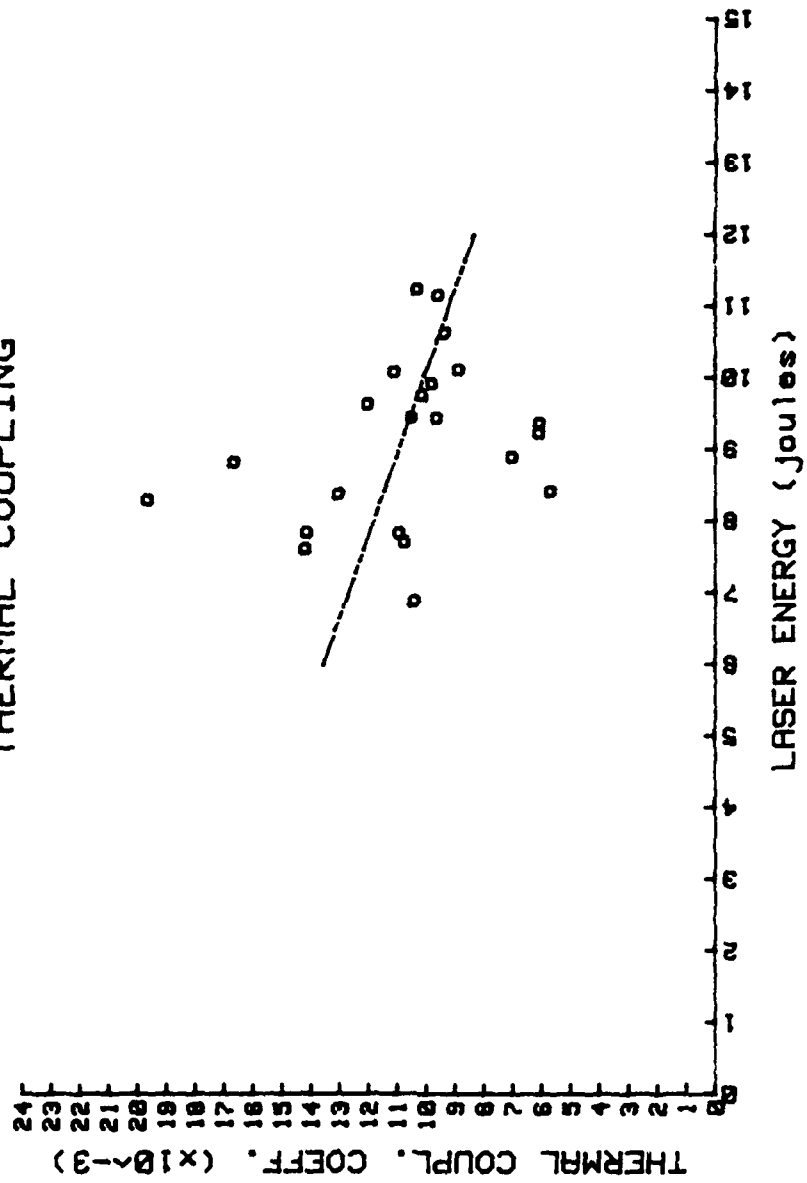


Figure 24. Thermal coupling of SS 304 targets (laser defocused).

THERMAL COUPLING

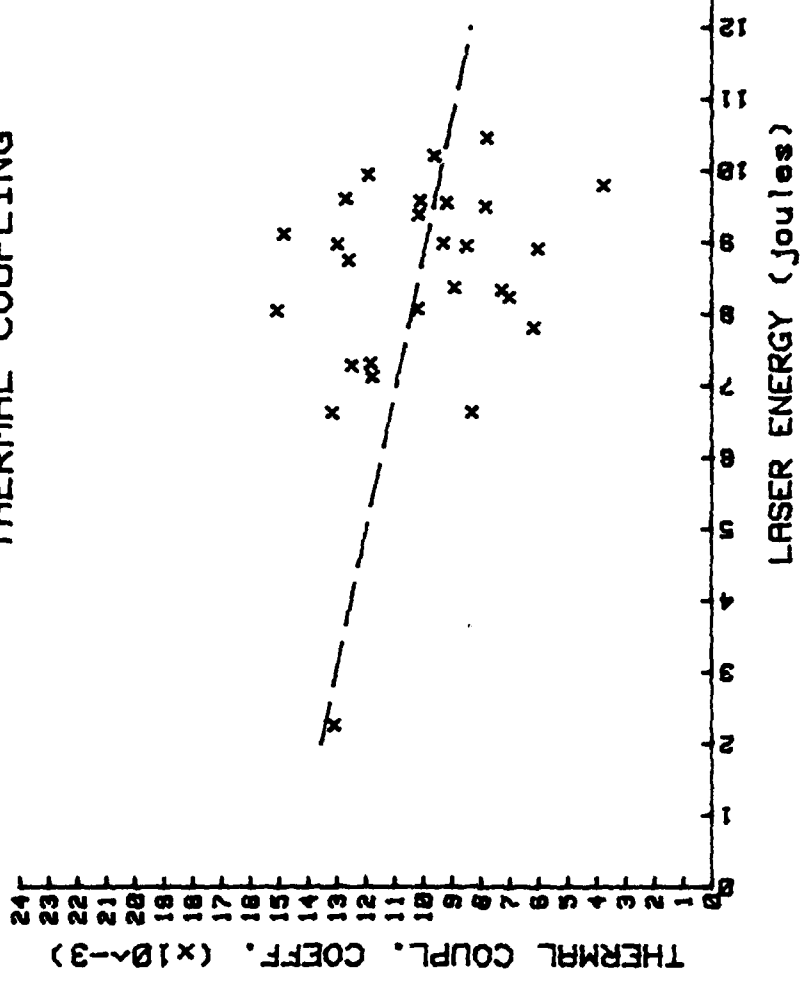


Figure 25. Thermal coupling of TiN coated targets (laser defocused).

THERMAL COUPLING

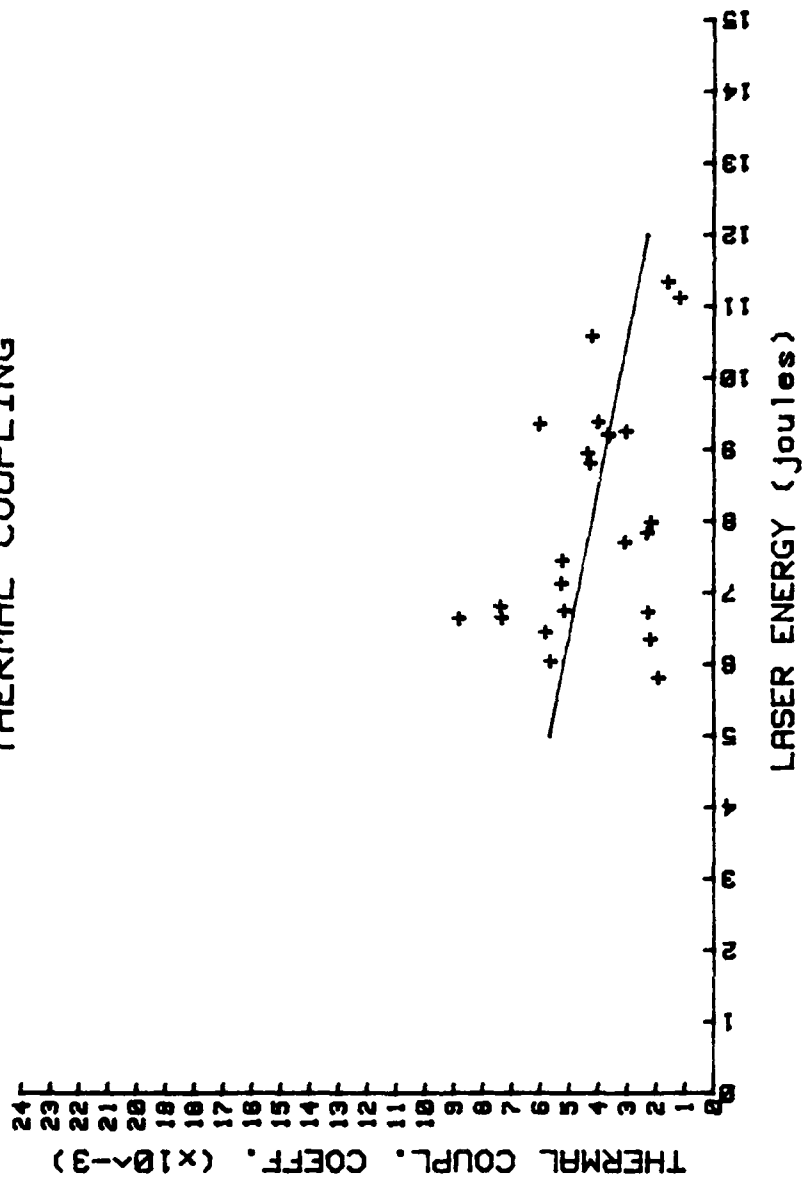


Figure 26. Thermal coupling of TiC coated targets (laser defocused).

THERMAL COUPLING

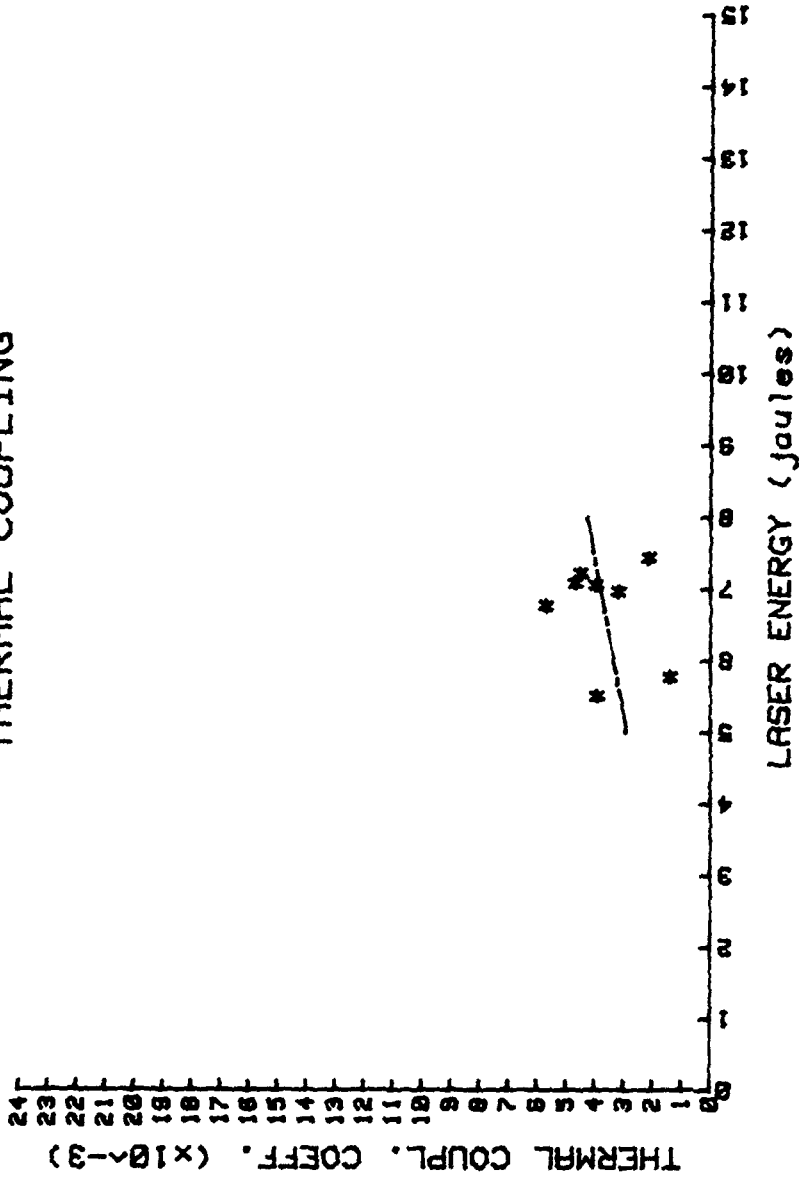


Figure 27. Thermal coupling of tantalum targets (laser defocused).

THERMAL COUPLING

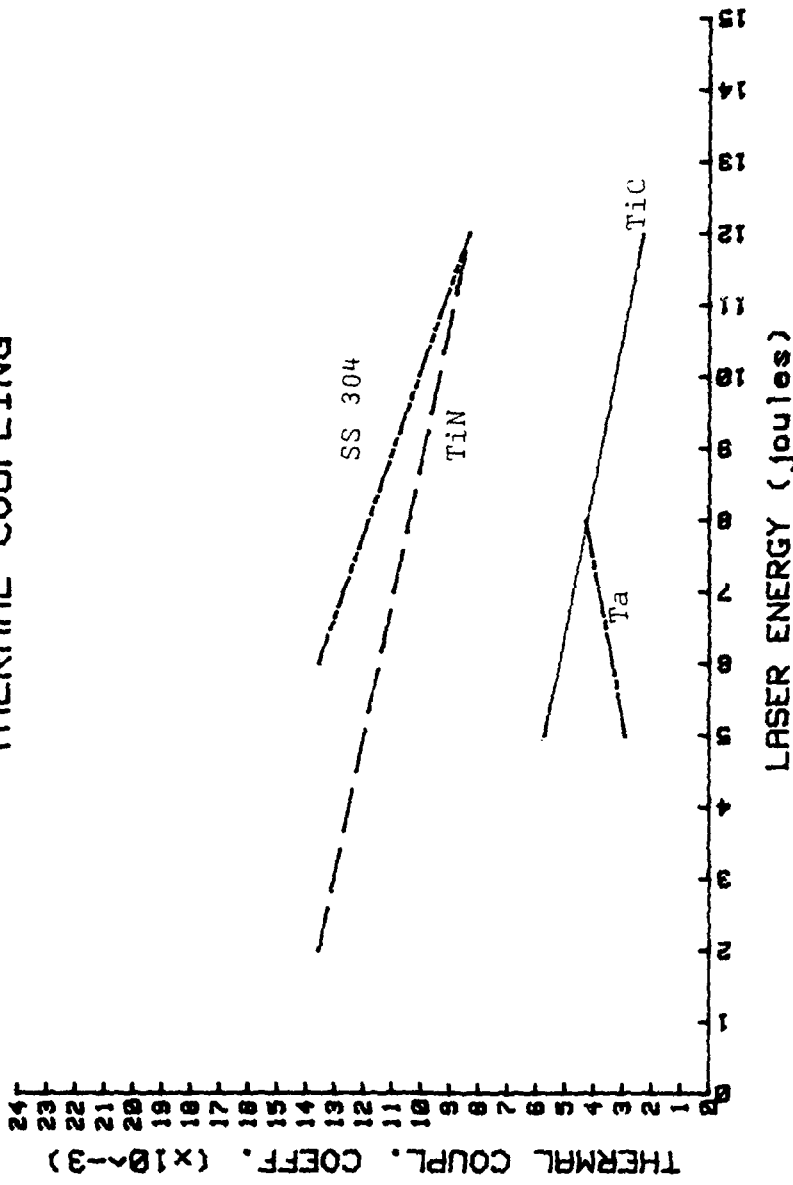


Figure 28. Comparison of thermal coupling of all target materials with defocused laser.

Table 1: Thermal Coupling Results

	TiC	TiN	Ta	SS 304
Thickness of coating	10 microns	10 microns	N/A	N/A
Thickness of target (focused/defocused) (mils)	5.0/5.0	5.0/5.0	9.5/1.0	5.0/5.0
Value of specific heat (J/gram degree C.)	0.565	0.582	0.14	0.60
Heat conduction coeff. (BTU/ft.hr.degree F.)	20.0	12.0	35.0	10.0
Density (gram/cm ³)	4.93	5.43	16.65	8.0
Number of data points (focused/defocused)	28/24	35/27	16/8	31/22
Average laser energy (J's) (focused/defocused)	8.65/8.07	10.70/8.57	7.63/6.72	8.47/9.13
Average temp. increase (degrees C.)	1.94/2.43	4.65/6.08	5.16/18.33	5.72/7.08
Average coupling coef. (x 10 ⁻³)	1.63/4.20	3.15/9.90	4.53/3.70	4.90/10.82

B. MOMENTUM COUPLING

1. Features of Photographic Results

Figure 29 contains two typical photographs taken by the CU-5 camera system positioned as illustrated in Figure 14. Several features deserve mention. The spots having no vertical trace were reflections from the chamber window of the reference laser beam before it struck the pendulum mirror. The vertical trace from the swinging pendulum is almost symmetric about the central bright spot (shutter opened before firing of laser). The initial backward swing results in the maximum downward reflection trace. The maximum upward trace had an amplitude of about 90.0% of the downward trace, indicating that the unavoidable damping of the simple pendulum device was small.

In all cases, it is observed that the trace is not centered on the bright spot. This is a result of the laser not being aimed at the horizontal center of the target. Any deviation results in the impulse producing a slight twisting torque on the pendulum which was designed to rotate to allow irradiation of both sides of the target. In most cases the swing then occurs in essentially the same plane as evidenced by the thinness of the trace during several oscillations.

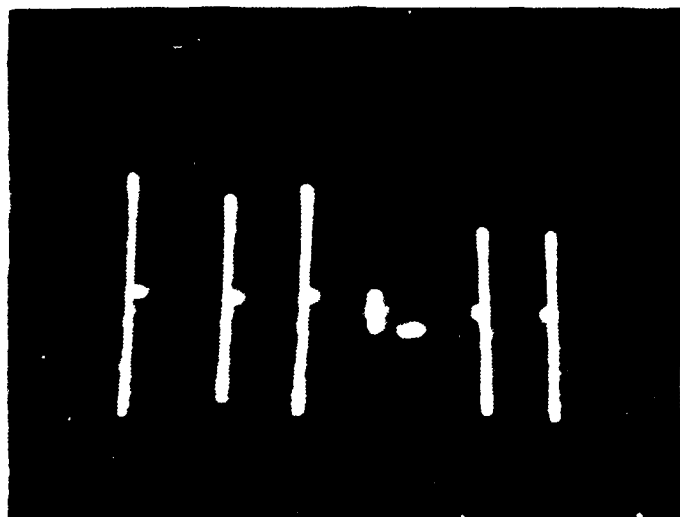


Fig. 1. 10 μ m and 10 μ m targets with laser energies of 1.1-1.2 mJ, reflecting from 0.114 degrees to 0.336 degrees.

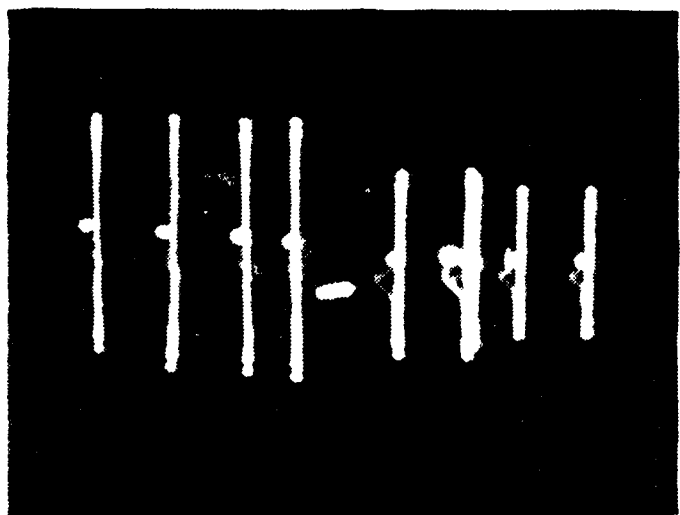


Fig. 2. 10 μ m targets with laser energies of 1.1-1.2 mJ, reflecting from 0.113 degrees to 0.336 degrees.

Fig. 3. 10 μ m targets with laser energies of 1.1-1.2 mJ, reflecting from 0.113 degrees to 0.336 degrees.

The slight deviation of the trace slope from the vertical is a result of the swing plane not being exactly normal to the filter plane. This was due to (as illustrated in Figure 14) the physical requirement to have the reference laser beside the filter plane, resulting in an angle of about 7.0 degrees. The need to conserve film by multiple exposures was accomplished by rotating the pendulum to reflect onto a different spot on the filter plane, again deviating from a normal reflection.

The pendulum weight of over 13.4 grams was almost two orders of magnitude greater than the target weights. Initial experiments showed that this much larger mass was necessary to prevent excessive swing which would have reflected the reference beam outside the limits of the chamber window, ie., the reflected trace would have been cut off. Greater pendulum mass would have decreased the reflection angles reducing the relative differences between targets. The larger mass also helped to minimize the differences of varying target weights. Similar to Johnson's results [41], efforts to measure the mass of target material removed after single and multiple shots were unsuccessful. The Sartorius electrobalance could measure down to 0.1 milligrams, but no mass difference was detected consistently

enough to attribute it to the mass loss of the blow-off material.

2. Momentum Coupling

The maximum amplitude of the downward trace was then measured along with the other distances to calculate the momentum imparted by the blow-off plasma. These resulting momenta, divided by the incident energy, are plotted in Figures 30-33 for the various materials. Again, the spread of data makes the best fit lines of Figure 34 the most convenient means of viewing the results. As with the thermal coupling, no significant difference was evident from the first shot and succeeding shots in the coupling observed. The prominent feature is the opposite slopes of the lines from the two sets of targets indicating a change from a factor of two difference of coupling at the lower end of the energy obtained to almost no difference at the higher energy. Table 2 summarizes the averaged results of the momentum coupling experiments. Further discussion of the results is deferred to Chapter V.

MOMENTUM COUPLING

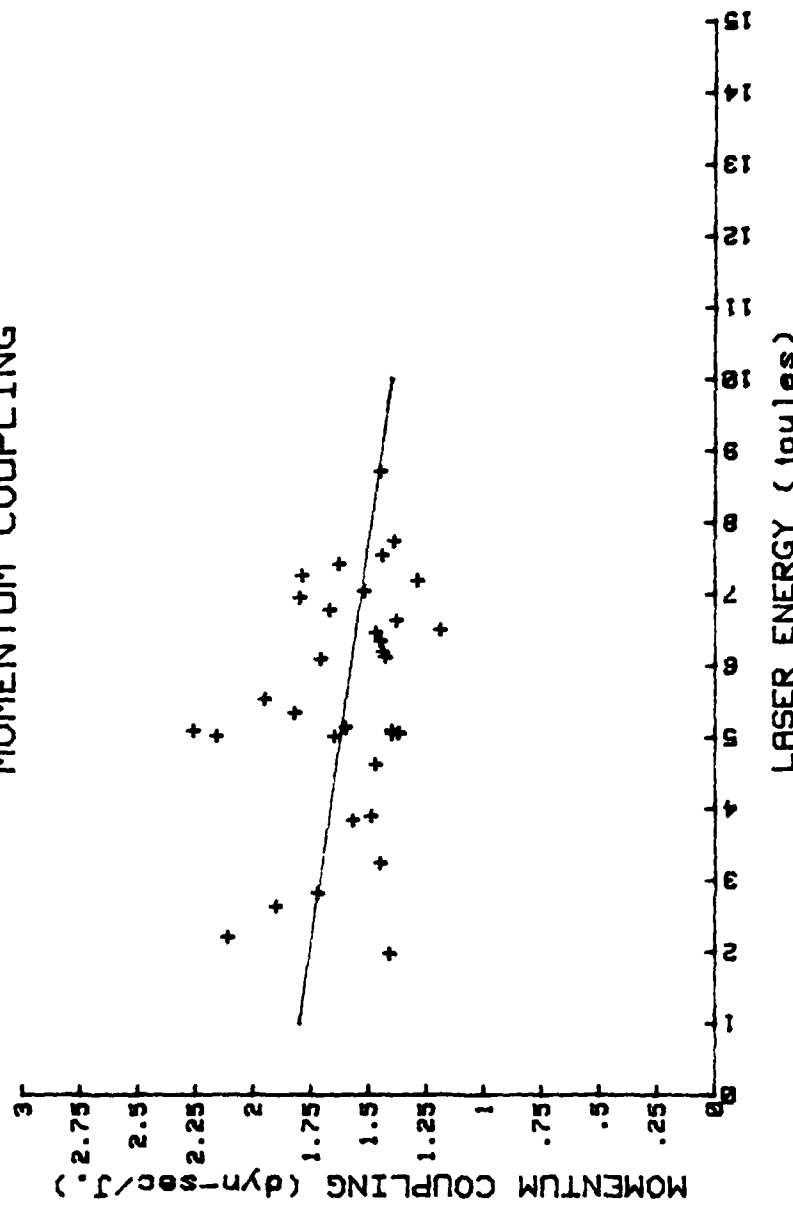


Figure 30. Momentum coupling of TiC coated targets.

MOMENTUM COUPLING

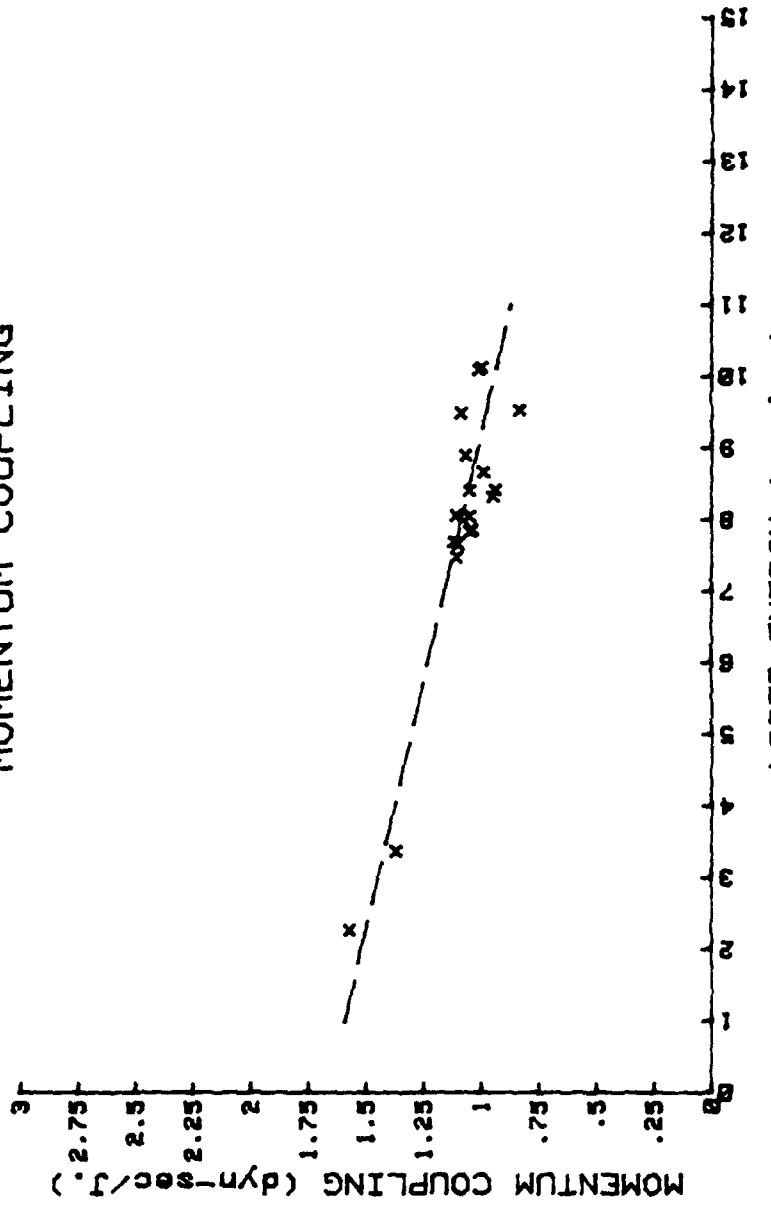


Figure 31. Momentum coupling of TiN coated targets.

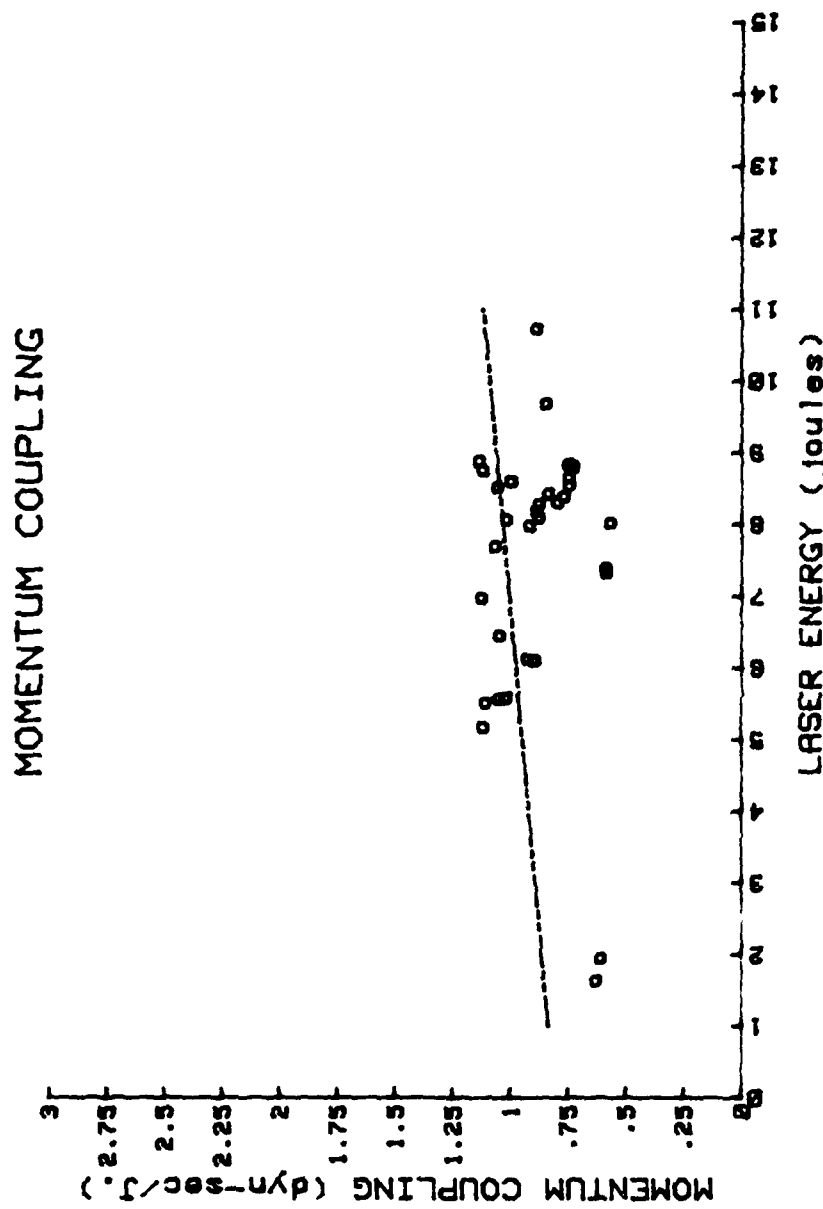


Figure 54. Momentum coupling of SS 304 coated targets.

MOMENTUM COUPLING

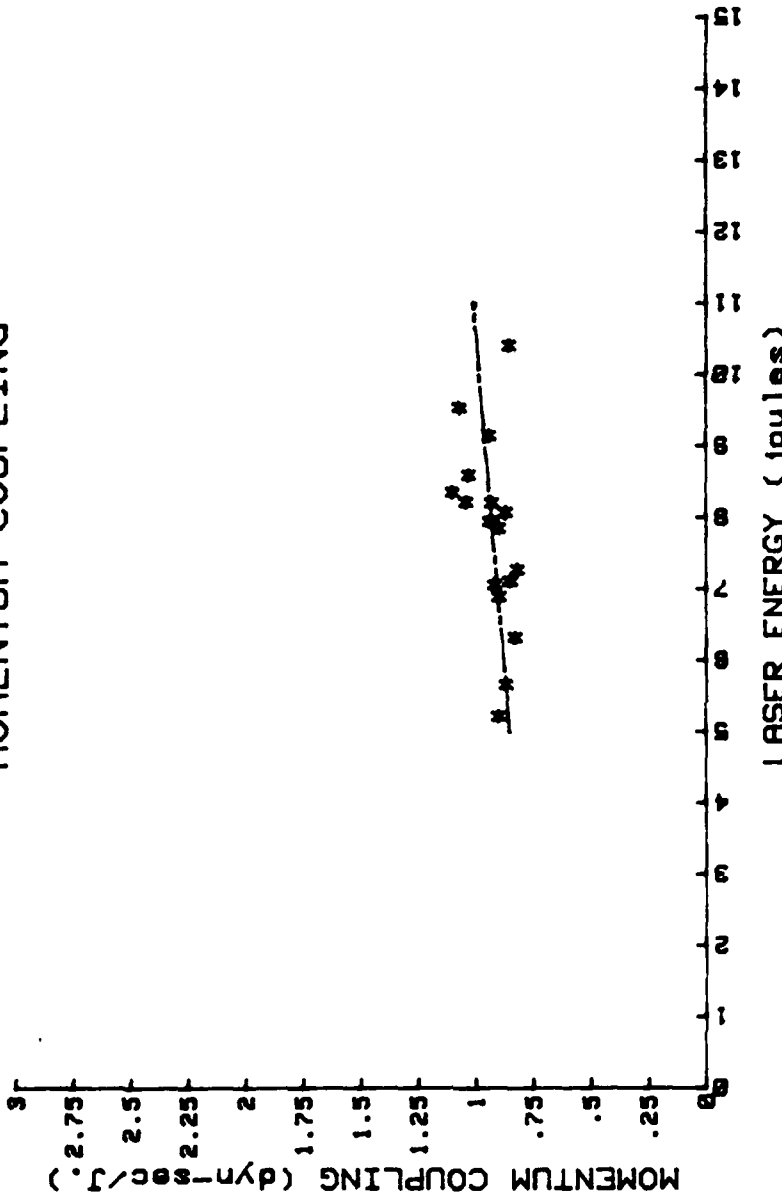


Figure 33. Momentum coupling of tantalum targets.

MOMENTUM COUPLING

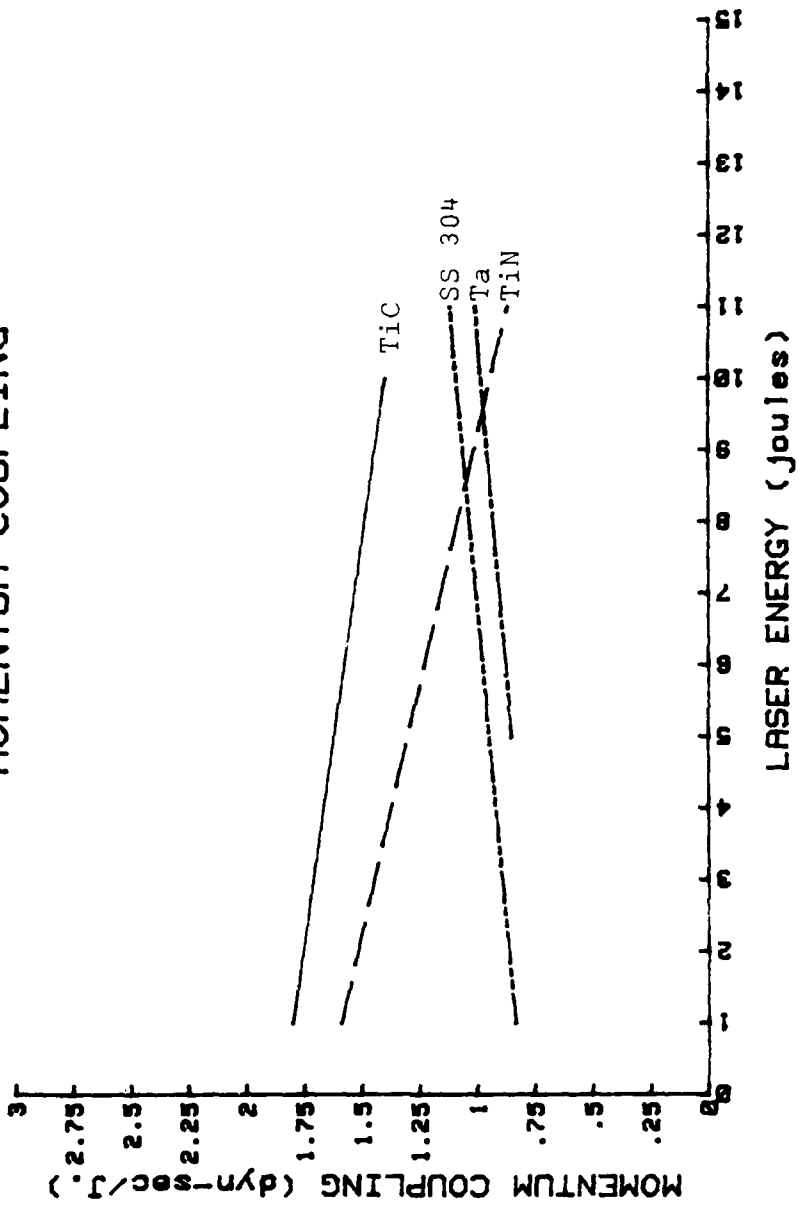


Figure 34. Comparison of momentum coupling of all target materials.

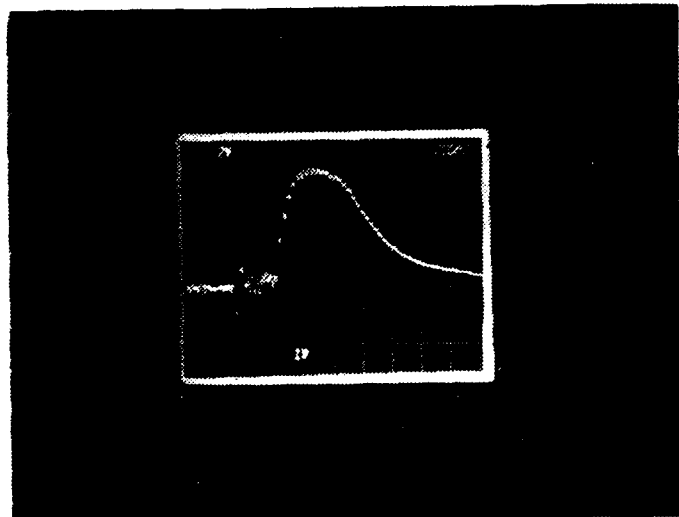
Table 2: Momentum Coupling Results

	TIC	TIN	Ta	SS 304
Number of data points	34	18	18	32
Avg. laser energy (J)	5.75	7.92	7.77	7.43
Avg. angle of deflection (degrees)	1.115	1.046	0.869	0.811
Avg. momentum imparted (dyn-sec)	9.20	8.63	7.23	6.69
Avg. momentum coupling (dyn-sec/J.)	1.60	1.09	0.93	0.90
Avg. mass of targets (gr.)	0.177	0.177	0.294	0.177
Mass of pendulum	13.424	gr.		

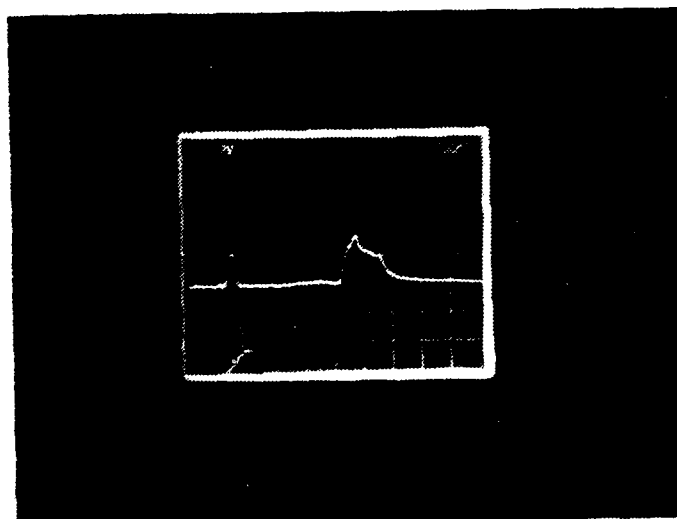
C. LASER PRODUCED PLASMA MEASUREMENTS

1. Oscilloscope Trace Characteristics

The following measurements were taken with the electrostatic probe located 2.0 ± 0.1 cm from the target surface and normal to the surface with a probe bias of -20.0 volts. Trace photographs similar to those in Figure 35 were then obtained. Unlike Brooks' results [40], only two plasma pulses were detected in the time scale and sensitivities used. These two were detected in all of the photographs. The upper trace in Figure 35 shows additional signals between the initial, early pulse and the main pulse. These additional signals were not present in all photographs and were not consistent enough to obtain meaningful data. The significant features analyzed were the time of flight (or arrival) of initial (also called "fast") and main pulses, the height or magnitude of both pulses, and the duration of the main pulse. The duration of the fast pulse was about 90.0 nsec, independent of target material or laser energy. The time of flight is related to the ion expansion velocity while the area under the curve is related to the amount of blow-off plasma. Both are related to the initial pressure of the plasma. The expansion velocity will also be proportional to the kT of the plasma ions.



Electrostatic probe signal from oscilloscope trace of plasma pulse from TiC coated target with energy of 7.63 J. (2 MV.
vert. div., 200 nsec./horiz. div.).



Oscilloscope trace from tantalum target with energy 31
J (1V.vert. div., 100 nsec. horiz. div.).

Figure 10. Typical traces of probe signals.

2. Trace Characteristic Results

The 57 traces obtained were analyzed and the results displayed in Figures 36-44 and in Table 3. Figures 36-39 contain the individual results of the time of flight to the probe of the main pulse for each material. This datum is most significant in the energy determination since the velocity term is squared. The fast pulse is almost twice as fast, but the amount of material in the fast pulse is one to two orders of magnitude less than in the main pulse, except for the tantalum. Only the comparative results for all the targets for the various measurements are displayed in Figures 40-44. The most striking feature of these figures is the difference of the tantalum results from the similarity of the other targets results. A discussion of this observation and a discussion of the relation of these results to those obtained in the momentum coupling is deferred to the next chapter. Table 3 contains the averaged values for this data and the calculated velocities for the expanding plasmas.

TIME OF FLIGHT OF PLASMA PULSE

1500

1400

1300

1200

1100

1000

900

800

700

600

500

400

300

200

100

PULSE ARRIVAL (nsec)

94

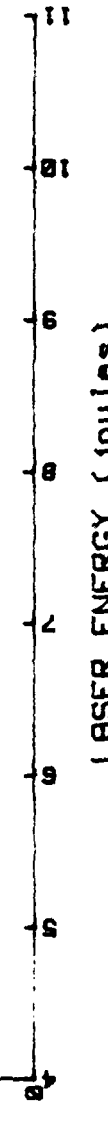
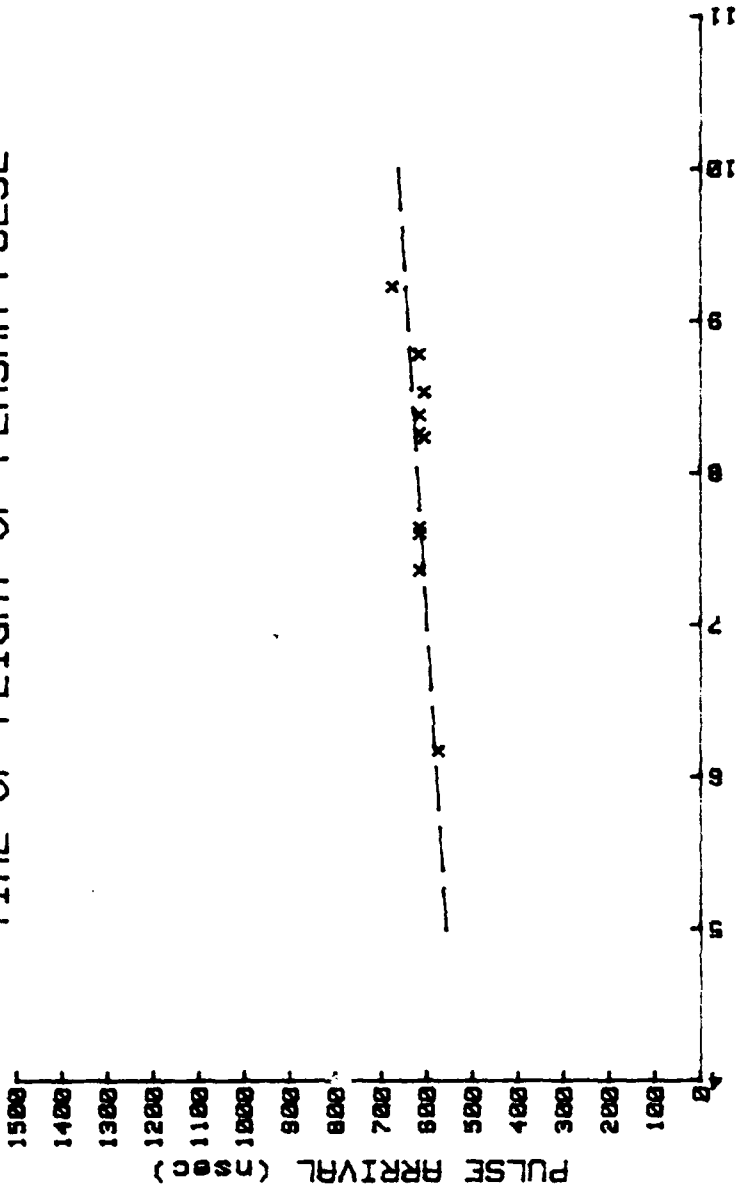


Figure 3b. Time of flight for TiC coated targets. Main plasma pulse over 2.0 cm. distance.

TIME OF FLIGHT OF PLASMA PULSE



LASER ENERGY (joules)

Figure 37. Time of flight for TiN coated targets. Main plasma pulse over 2.0 cm. distance.

AD-A119 332

NAVAL POSTGRADUATE SCHOOL MONTEREY CA
AN INVESTIGATION OF ENERGY COUPLING IN VARIOUS ARC SUSCEPTIBLE --ETC(U)
JUN 82 R M METHENY

F/B 20/5

NL

UNCLASSIFIED

2 OF 2
ADA
149332

END
DATE
FILED
10-82
DTIC

TIME OF FLIGHT OF PLASMA PULSE

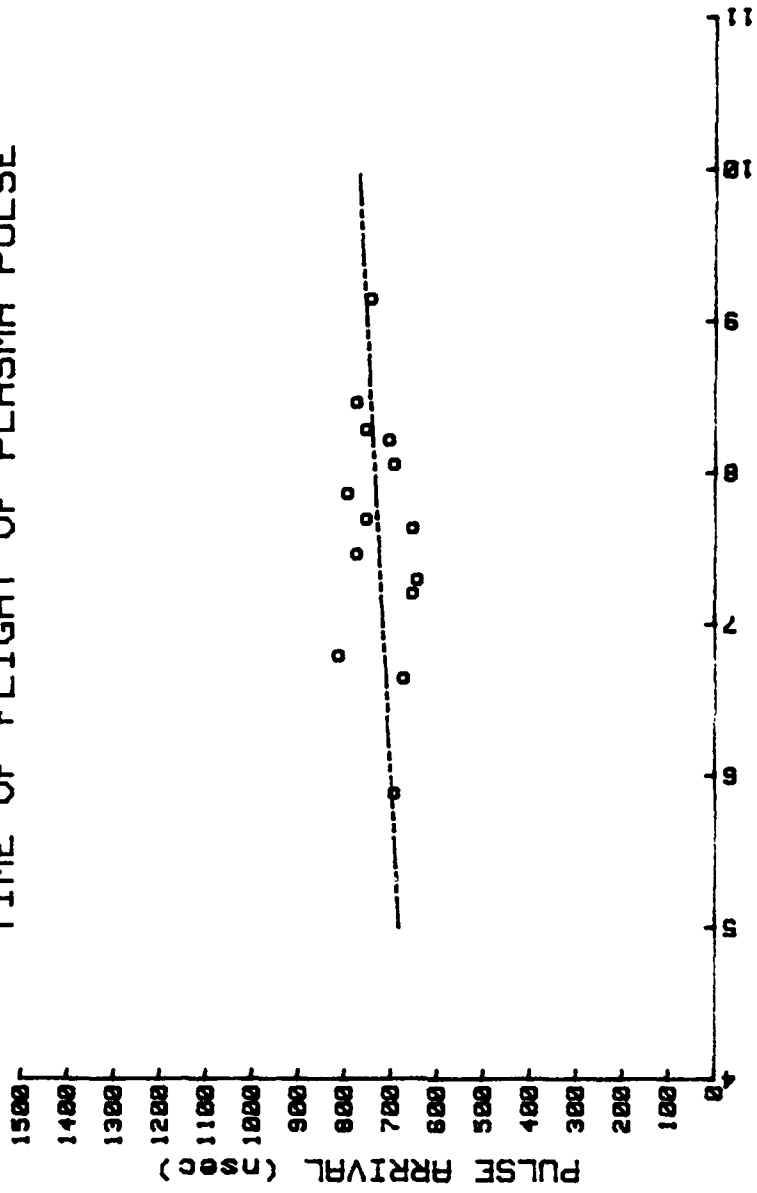


Figure 38. Time of flight for SS 304 targets. Main plasma pulse over 2.0 cm. distance.

TIME OF FLIGHT OF PLASMA PULSE

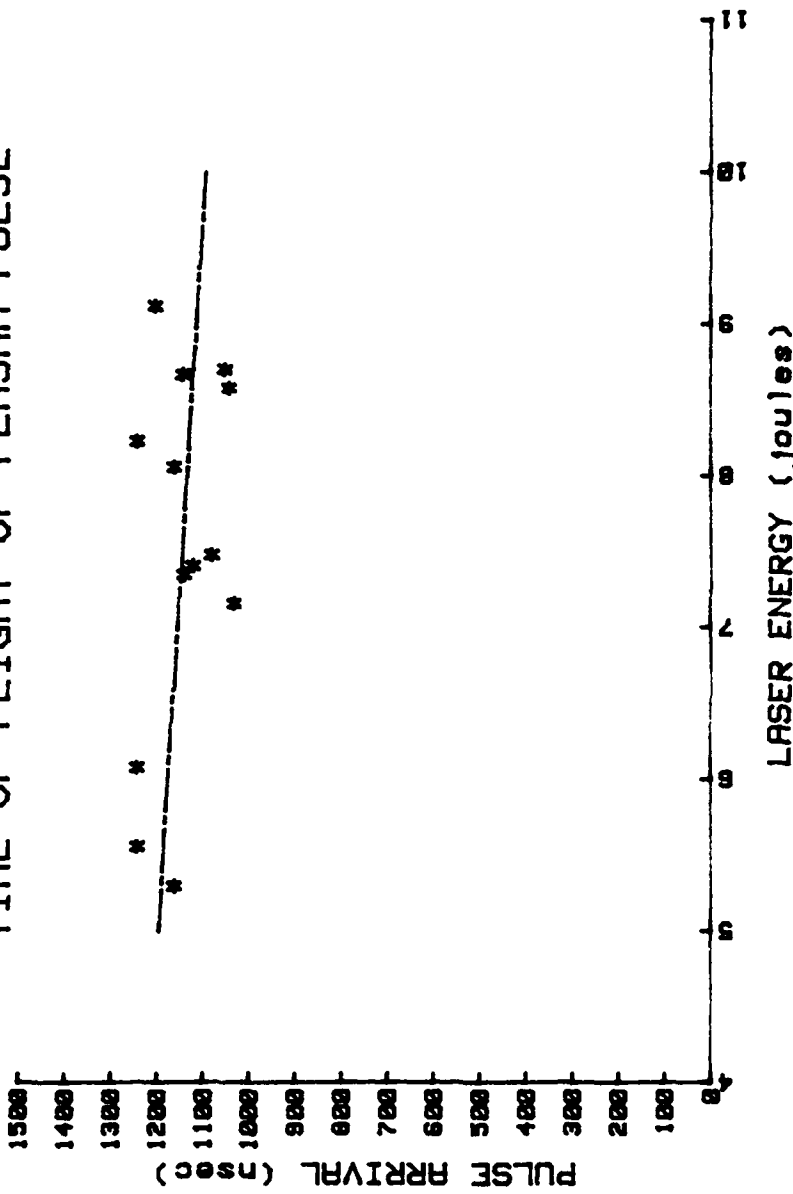


Figure 39. Time of flight for tantalum targets. Main plasma pulse over 2.0 cm. distance.

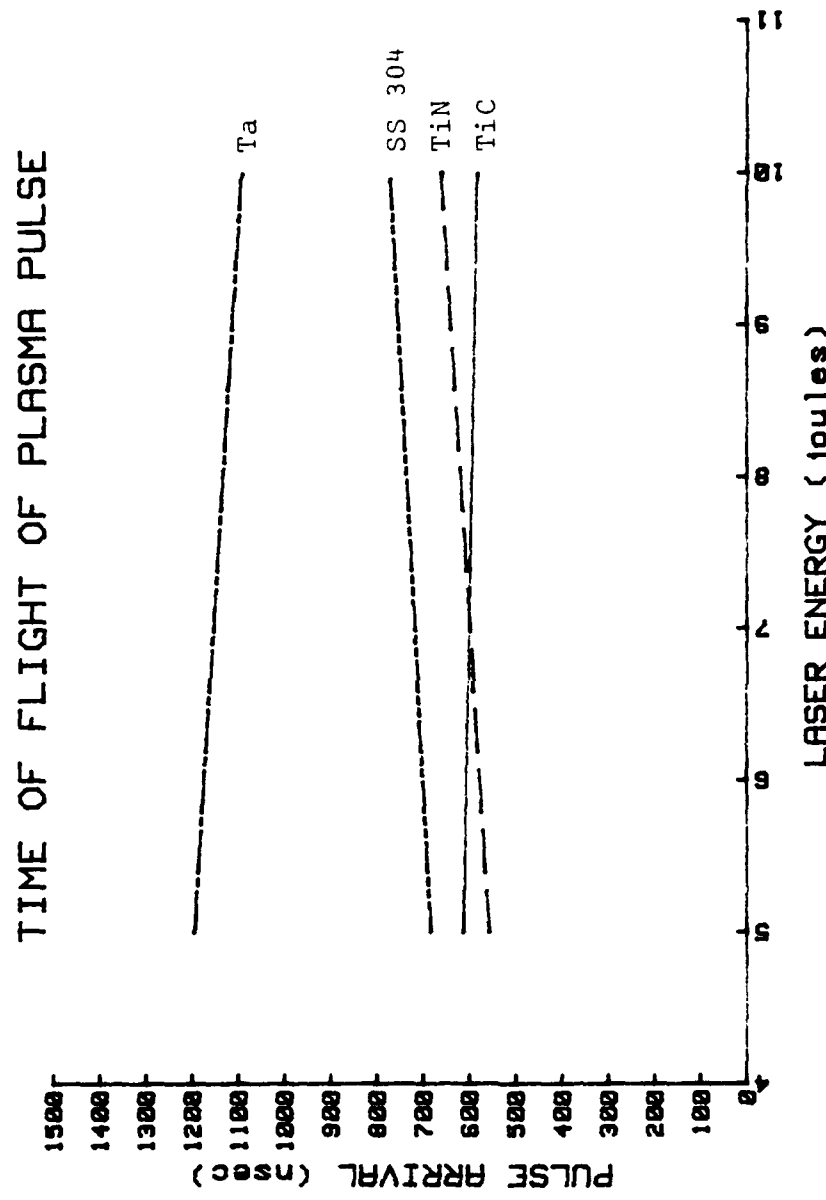


Figure 40. Time of flight for all targets. Main plasma pulse over 2.0 cm. distance.

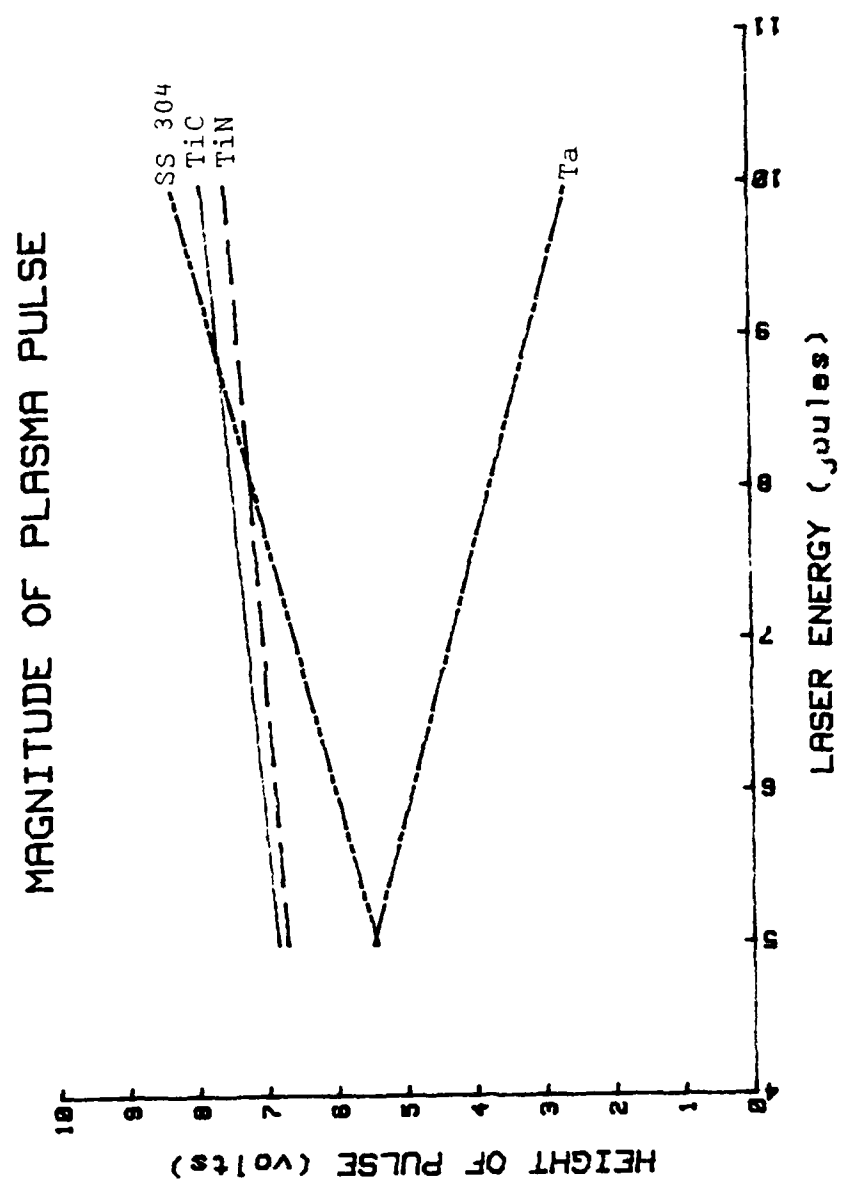


Figure 41. Height of main plasma pulse from various targets.

DURATION OF PLASMA PULSE

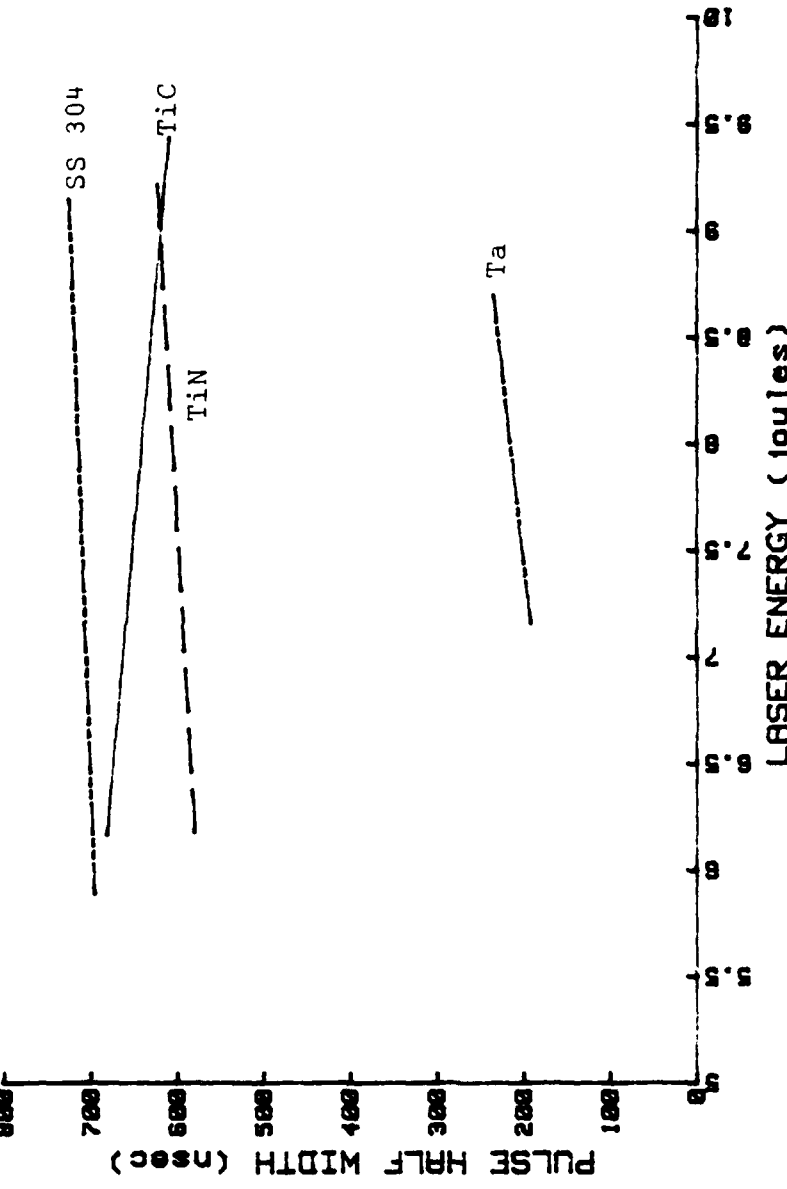


Figure 42. Comparison of temporal length of main plasma pulse from various targets. Pulse width measured at half of maximum amplitude.

TIME OF FLIGHT OF PLASMA PULSE

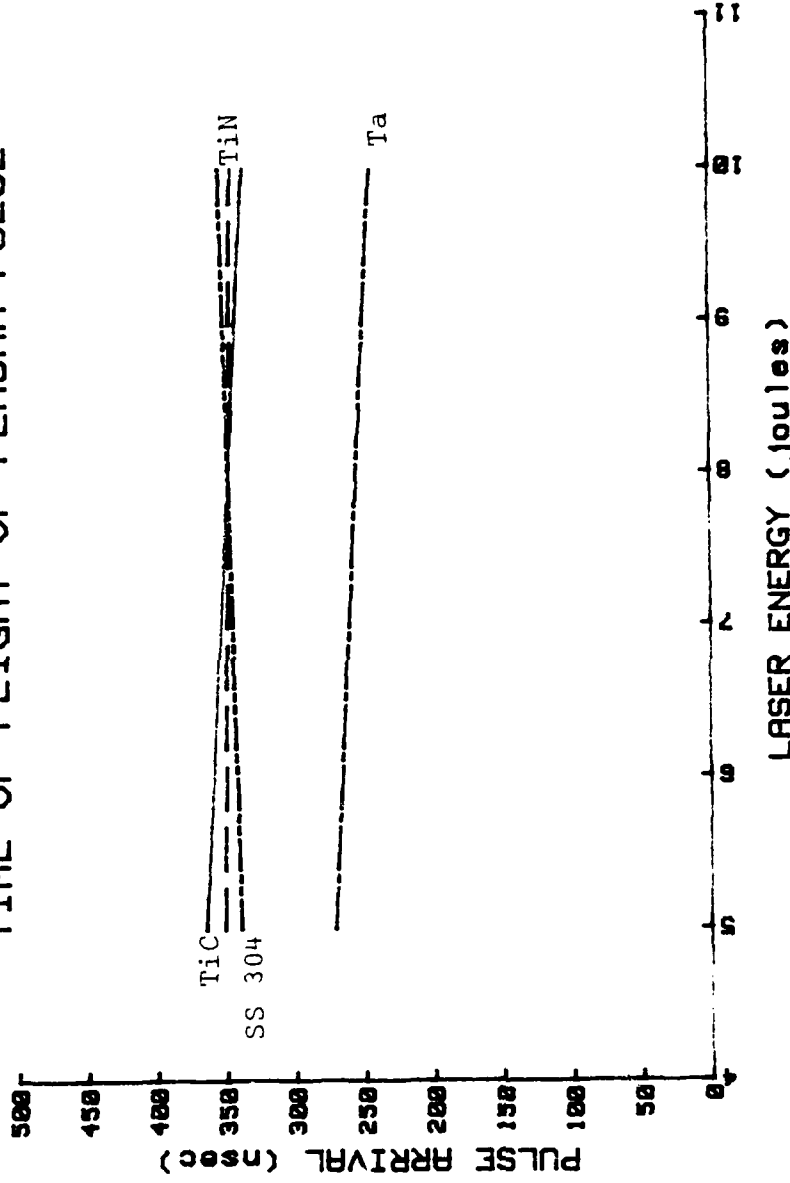


Figure 43. Comparison of time of flight for fast plasma pulse from various targets. Measured over 2.0 cm. distance.

MAGNITUDE OF PLASMA PULSE

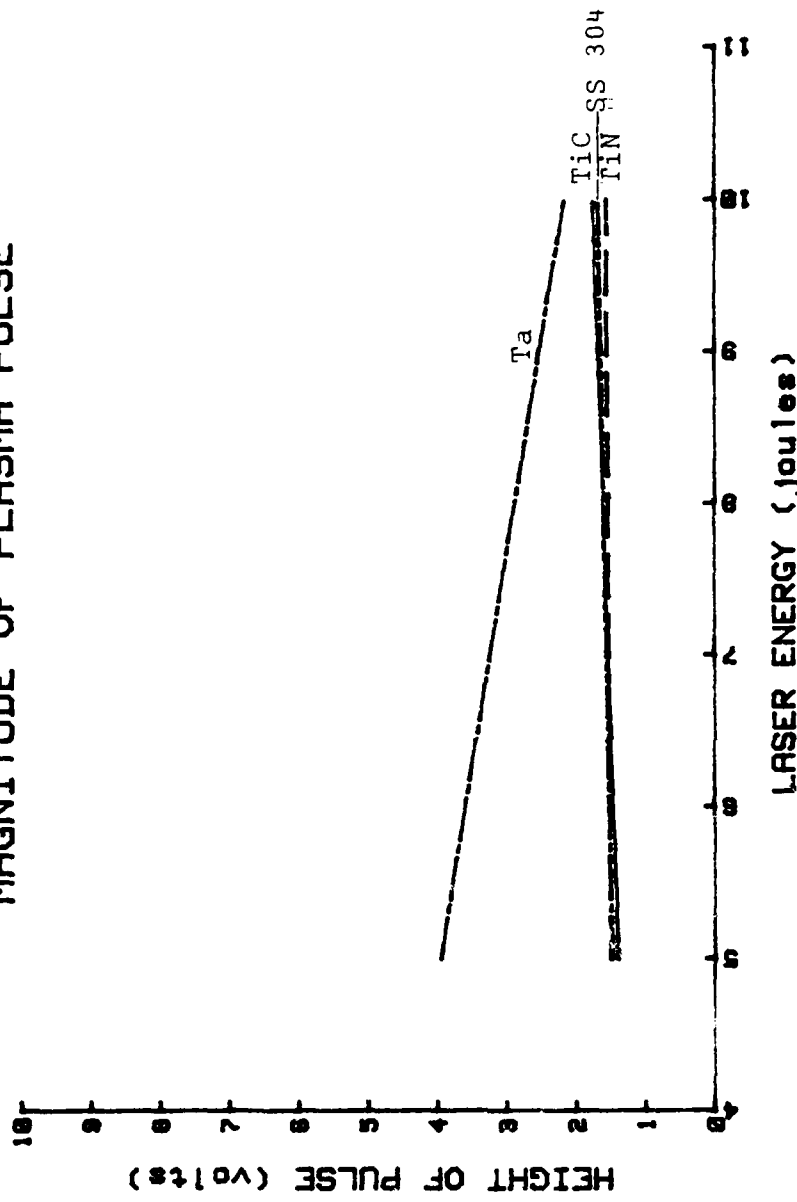


Figure 44. Comparison of heights of fast plasma pulse from various targets.

Table 3: Electrostatic Probe Results.

	TIC	TiN	Ta.	SS 304
Number of data points	20	10	13	14
Avg. laser energy (J.)	7.90	8.03	7.63	7.62
Avg. velocity of main pulse ($\times 10^6$ cm/sec)	3.36	3.23	1.80	2.74
Avg. magnitude of main pulse (volts)	7.45	7.21	4.0	6.94
Avg. length of main pulse (nsec)	642	605	213	710
Avg. velocity of initial pulse ($\times 10^6$ cm/sec)	5.76	5.78	7.79	5.79
Avg. magnitude of initial pulse (volts)	1.61	1.54	3.05	1.59

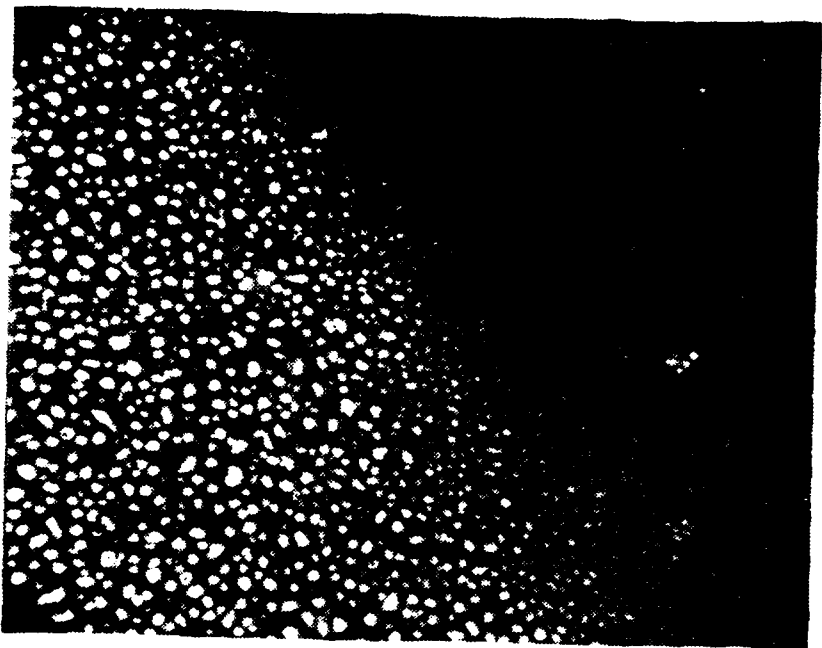
D. SURFACE DAMAGE

Unipolar arcing has already been described as a plasma-surface interaction which is a major surface damage mechanism for many types of materials. This thesis looked at the energy coupling from heat and momentum transfer on four surfaces. A microscopic examination of the surfaces was necessary to verify whether arcing was taking place on the targets. Similar examinations have been performed by many previous workers at NPS [6-10] in the investigation of the unipolar arcing process. Repetition of their results will be avoided.

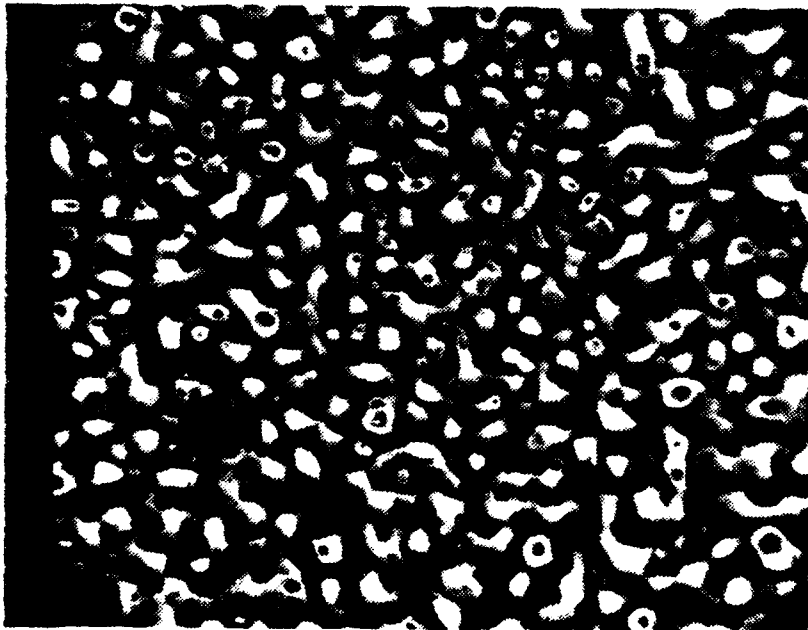
1. Arc Resistant Materials

Both titanium alloys proved to be resistant to unipolar arcing damage. Figures 45 and 46 show typical SEM micrographs of the target surface after irradiation by the Nd-glass laser. The TiC coated surfaces showed the same "honeycomb" appearance as described in References 6 and 44. No evidence of unipolar arcing was seen on any of the TiC coated targets.

The TiN target surface had a very different appearance, as shown in Figure 46. The dominant feature on the TiN coated surfaces was the cracking over the entire interaction area.

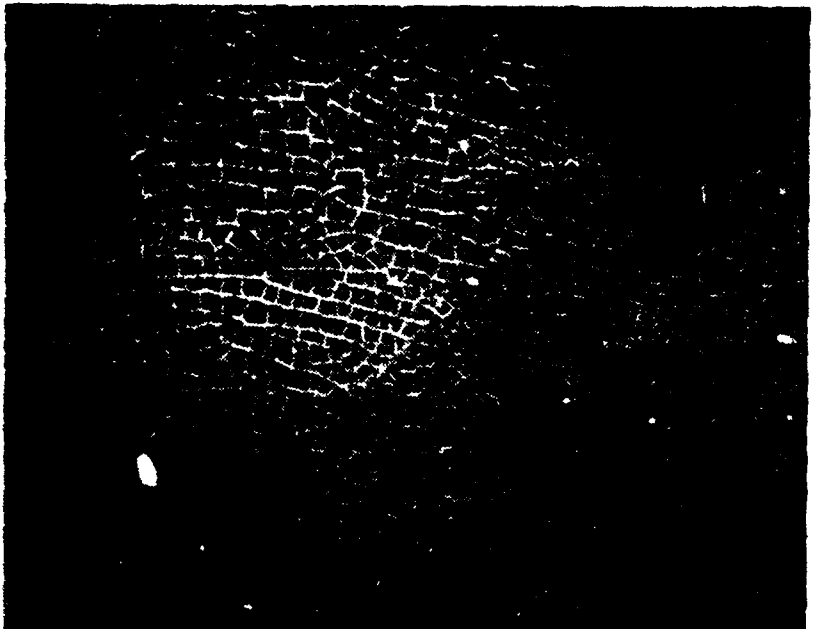


Edge of damaged area of TiC coated target (8.31 J., SEM x1000).

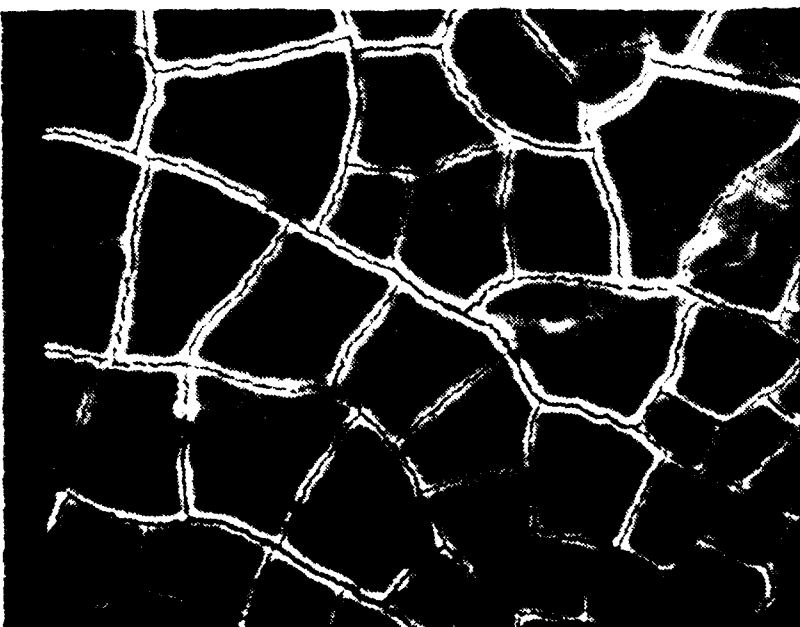


Center of damaged area of TiC coated target (8.31 J., SEM x1000).

Figure 4. Typical surface damage to TiC coated targets.



Center and rim of damaged area of TiN coated target
(2.13 J., SEM x100).



Center of damaged area of TiN coated target (2.13 J.,
SEM x100).

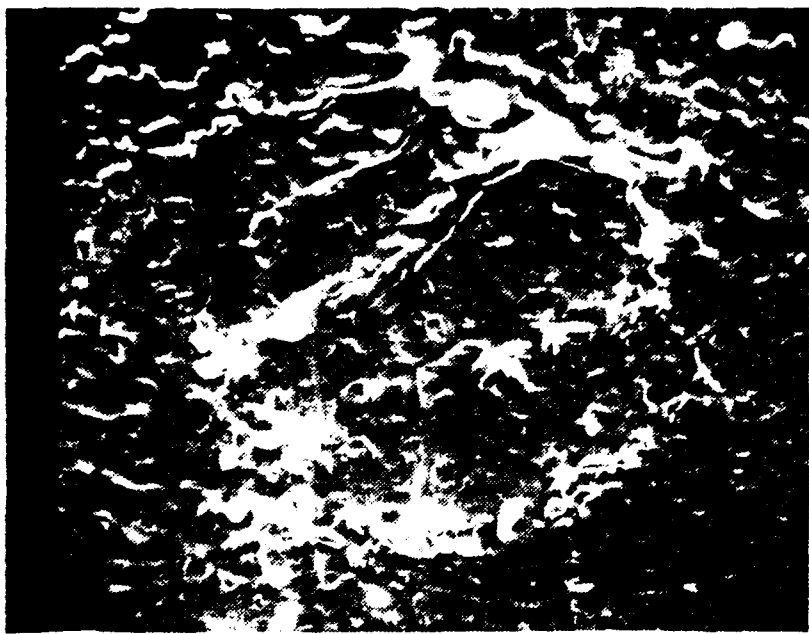
Figure 44. Physical surface damage to TiN coated targets.

Cracking into irregular shapes starts at the edge of the damaged area and breaks the surface into areas of less than 100 microns². The areas increase towards the center of the impact area to a maximum size of about 400 microns². Complete removal of the surface material was not evident in any sample and no unipolar arcs were seen on any of the TiN coated targets.

2. Arc Prone Materials

The unpolished SS 304 did exhibit unipolar arcing as evidenced by the craters in the lower photo of Figure 47. Several references [6-10] contain descriptions and similar photographs of unipolar arcing on the SS 304 targets.

Tantalum foil also showed evidence of a significant amount of damage by unipolar arcing. The lower photo in Figure 48 shows one area where arcing occurred in a track with a linear density of about 1000 arcs/cm. They have the typical crater diameter of 10-15 microns and the central cathode spot of about 1-2 microns diameter and 3-6 microns deep. There was evidence of overlapping of craters on multiple shot targets and a smoothing effect similar to that observed on SS 304 targets. The unipolar arc craters and the wavelike ridges produced from the cooling molten material were the dominant features of the tantalum surface.

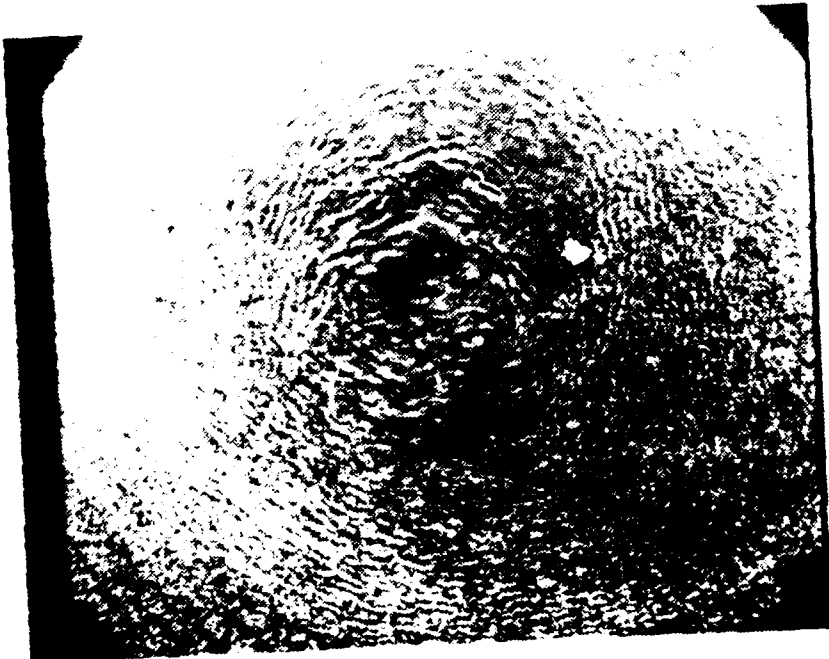


Left: center impact area on SC 804 target 11.10 & 9.47 J., 10M x 100.

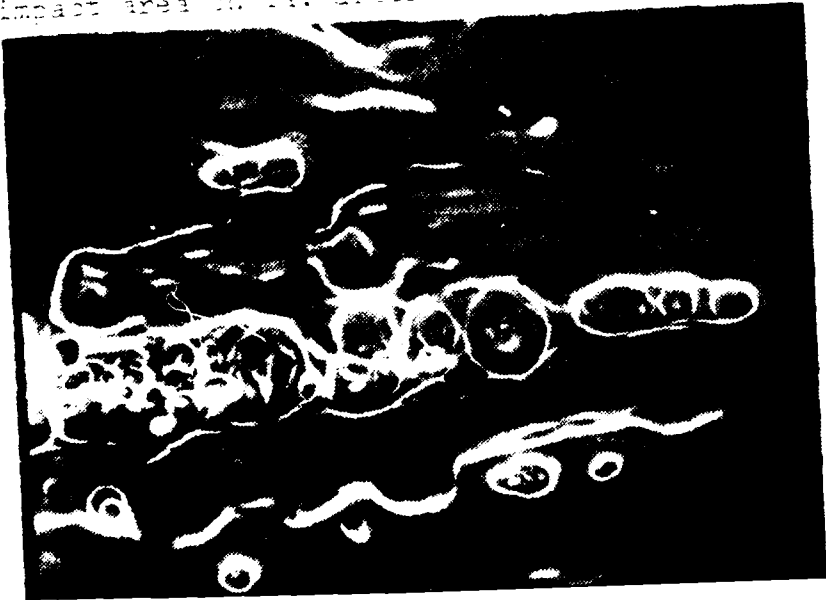


Right: off center impact area on SC 804 target (11.10 & 9.47 J., 10M x 100).

Figure 4. Typical surface damage to SC 804 targets.



Liner impact area on Ti. after 3 shots (avg. 7.16 J., 30° R.L.).



V. DISCUSSION AND CONCLUSIONS

A. RELIABILITY OF RESULTS

The purpose of this thesis was a comparison of two mechanisms of energy coupling between materials which were unipolar arcing resistant and those which are susceptible. Such a comparison does not require that the absolute values of the quantities be accurate; their relative values in relation to each other is of primary interest. However, some check of the absolute values is desirable to verify the experimental procedure and theory of the process. Each major procedure had many sources of possible error, but their results compared reasonably with previously published works.

1. Thermal Coupling

The thermal coupling coefficient was given in equation 6 as a function of two physical properties, the specific heat and density; and four measured quantities, target thickness (estimated fractional error of 5.0%), laser energy (estimated error of 4.0%), laser interaction area (estimated error of 10.0%), and temperature increase (estimated error of 20.0%). The large temperature error estimate is due to

the visual recording of data from the digital thermometer and the unknown reliability of the thermometer for such sudden rates of increase. Another factor in the use of equation 6 is that this experiment required a weighted average be used for the titanium coated targets. However, the thinness of the coating essentially reduced it to the consideration of a homogeneous material. This neglects any consideration of the boundary effects on heat conduction. Table 1 shows that the heat conduction coefficients of the materials do vary by a factor of three. The specific heat was taken as a constant value (stated for 25 degrees C.), although specific heat is actually temperature dependent by the Neumann-Kopp empirical relations. The specific heat value varies throughout the material by about 10%. With these considerations, an overall error in the thermal coupling coefficient of 50-60% is possible. These errors would be typical for each material and the relative positions of the thermal coupling lines should be accurate. The anomaly of tantalum in Figure 28 was discussed previously.

For the intensities used in this experiment (about 50 J./cm² or 10⁹ W./cm²) it is expected that the coupling coefficient line would have a negative slope. From the data points contained in Reference 19 and Figure 5, it appears

that a reasonable value would be 5% or less. Figures 22 and 28 show that the values are decreasing and never exceed 2%. The experimental results do seem to conform to previous results.

2. Momentum Coupling

Many sources of possible error exist in the calculation of a momentum coupling coefficient. Relevant measurements included the weights of the target and pendulum, friction factor, distances of filter plane from target, length of pendulum to laser impact spot, distance from reference laser spot on mirror to target impact spot, length of trace on photograph, and angle between reference and reflected beams. A correction factor to the trace length is also required due to photographic reduction. The possible errors also become nonlinear as arctangent and cosine functions are involved. It was assumed that no damping occurred in the first half swing and that the pendulum mass was uniformly distributed, although it contained circular holes cut throughout its length. Possible energy meter error was again present. A 100% error or greater is possible in the absolute value of the coefficient. Careful repetition of the procedures for each target material should again make the relative positions of the momentum coupling reliable.

Figure 6 and other figures from the same reference show momentum transfer maxima in the same intensity range as that in these experiments and having a value of 2-7 dyn-sec/J. The values shown in Figure 34 have the same order of magnitude. The opposite slopes simply indicate that the momentum transfer coupling curves have different shapes for the energy range under consideration for the different target materials. Again, the absolute values obtained for the momentum coupling in this experiment seem reasonable.

3. Velocity Measurements

The procedures used in determining the velocity of the laser plasma particle velocities followed those of Callahan [43] and Brooks [40], who estimated a possible error of 47% in the velocity measurements. Sources of error include measurement of target to probe distance, cable/equipment delay times, accuracy of triggering, and interpretation of photographs. The relative values between materials should again be reliable.

The speed of the fast and main plasma pulses in this experiment (displayed in Table 3) was less than that determined by Callahan for aluminum by a factor of 2-3. The results for aluminum in References 40 & 43 differed by even more, so individual experimental conditions such as laser

energy, focal spot size, mass, etc., will produce significant differences. Varying materials and energy intensities are the dominant factors. No data were available for a comparison of the probe signal characteristics displayed in Figures 41-44 and Table 3.

B. COMPARISON OF ENERGY COUPLING OF TARGET MATERIALS

1. Thermal Coupling

Figures 22 and 28 and Table 1 summarize the thermal coupling coefficient results. Figure 22 and 28 agree in the order of increasing coefficients with the exception of tantalum in Figure 22 which was discussed earlier. The average value for TiC coated targets is about 35% that of SS 304 while that of TiN targets is 64% and 91% for the focused and defocused cases respectively. Tantalum's value is 92% that of SS 304 in the focused case, which is considered more accurate for tantalum. These values are only average values valid only in a narrow energy range, and additional points over a wider range could change the relative order.

2. Momentum Coupling and Plasma Pulse Characteristics

TiC coated targets had the maximum momentum coupling in the range under consideration. The average values for the TiN, SS 304, and tantalum targets was 68%, 58%, and 56%, respectively, that of the TiC targets. Unlike the thermal

coupling however, the slopes of the lines differ and the average values are less meaningful. As seen in Figure 34, the lines cross and indicate that the momentum coupling for these two arc resistant materials decreases over the energy range while the arc prone materials have an increasing momentum coupling.

Analysis of Figures 40-44 aids in understanding the relative momentum coupling of the targets. As previously mentioned, the momentum imparted is related both to the expansion velocity of the plasma and the quantity of blow-off material. This quantity is related to how much of a probe signal is produced for how long a period or the magnitude and length of a pulse. The nearly horizontal slopes in Figures 40 and 43 indicate that the velocity is not very energy dependent in this range. In increasing order, the average speeds for the targets follow the same order as increasing momentum. The lengths (the full width at half maximum amplitude) and magnitudes of the main pulse in Figures 41 and 42 show this same order with the exception of the reversed order of SS 304 and TiN in Figure 42. They also indicate a crossover point in which the SS 304 blowoff plasma quantity increases beyond that of the coated targets. This leads to an increase in the relative momentum compared

to the coated targets as pictured in Figure 34. The tantalum has the least speed and quantity in the main pulse, but the fastest and greatest amount in the initial pulse. Tantalum does have 2-3 times the weight and density of the other targets which would lead to more rapid cooling and more recombinations during its slower expansion rate. The cause of its increasing momentum coupling is not evident from these figures, but is presumably related to the larger atomic mass.

3. Role of Unipolar Arcing

These experiments indicate that the effect of unipolar arcing on thermal coupling is to increase it. This is evidenced by the higher coupling on the SS 304 and tantalum targets. The increased ion bombardment, recombinations, and local heating around the cathode spot are likely causes for the continued coupling of thermal energy from the plasma to the surface after the plasma shields most of the remaining laser energy from reaching the target surface.

The momentum coupling and the dissimilarity of plasma characteristics of tantalum and SS 304 are harder to relate to unipolar arcing. The increased target material fed into the plasma from the arc craters would indicate a greater momentum imparted, which is the case for SS 304 at

higher energies. The role of increasing crater number density and the decoupling of thermal energy from the possible onset of LSD waves should be investigated in the observation of a uniformly higher value of thermal coupling. The tantalum (a high Z material) pulse characteristics are much different from the other materials and difficult to compare to them.

In conclusion, it must be remembered that the microscopic unipolar arcing process cannot be isolated from all the other microscopic and macroscopic processes taking place in the laser-plasma-surface interaction. Each material has different surface roughnesses, inhomogeneities, reflectivities, thermal and electrical properties, and other physical characteristics which all effect the coupling of energy. These experiments did show that two arc-prone materials had a higher thermal coupling coefficient and a different slope for the momentum coupling curves through the energy intensities investigated. It has not been conclusively shown that the unipolar arcing process plays a significant role in the momentum coupling.

VI. RECOMMENDATIONS

The last statement in the preceding chapter leads to several recommendations. A larger sampling of different materials, both arc susceptible and resistant, should undergo similar experimentation. Also, the data base and range of energies for the four surfaces tested should be expanded to verify these results and extend them to larger and smaller energy intensities.

Continued research into energy coupling would benefit from the acquisition of additional diagnostic equipment. The lone electrostatic probe broke during target removal. A new probe or alternate technique will be needed for future velocity measurements. Some piezoelectric crystals would be more accurate than the shopmade pendulum for momentum measurements. A means of accurately determining the mass removed from the surface is still needed. The new mass spectrometer will aid in the determination of the relative amounts and composition of the blow-off plasma. Some means of determining the reflectivity vs. time would also be of benefit in the energy balance bookkeeping. It is also recommended that two students normally be assigned to thesis work in this area since concurrent operation of diagnostic

equipment and laser firing often required the presence of
the lab technician, who has many other responsibilities.

LIST OF REFERENCES

1. Behrisch, R., "Surface Erosion From Plasma Materials Interaction," Journal of Nuclear Materials, V. 85, 86, p. 1047-1061, 1979.
2. Goodall, D.H.J., Conlon, T.W., Scofield, C., and McCracken, G.M., "Investigation of Arcing in the DITE Tokamak," Journal of Nuclear Materials, v. 76, 77, p. 492-498, 1978.
3. McCracken, G.M., and Goodall, D.H.J., "The Role of Arcing in Plasma Produced Metal Impurities in Tokamaks," Nuclear Fusion, Culham Laboratory, 1977.
4. Robson A.P. and Thonemann, P.C., "An Arc Maintained on an Isolated Metal Plate Exposed to a Plasma," Institution of Electrical Engineering, V. 106, PT. A, SUPP. Z, April 1959.
5. Schwirzke, F., and Taylor, R.J., "Surface Damage by Sheath Effects and Unipolar Arcing," Journal of Nuclear Materials, V. 93, 94, p. 740-748, 1980.
6. Keville, M.T., "An Investigation of Unipolar Arcing Damage on Stainless Steel and TiC Coated Surfaces," MS Thesis, Naval Postgraduate School, Monterey, Ca., June 1980.
7. Barker, J.H., and Rush, R.J., "An Investigation of Plasma-Surface Interactions on Selected Conductors and Semiconductors and Insulators," MS Thesis, Naval Postgraduate School, Monterey, Ca., June 1980.
8. Ryan, F.T., and Shedd, S.T., "A Study of the Unipolar Arcing Damage Mechanism on Selected Conductors and Semiconductors," MS Thesis, Naval Postgraduate School, Monterey, Ca., June 1981.
9. Hoover, T.J., "An Investigation of Unipolar Arcing in Various Conductors and Metallic Glasses," MS Thesis, Naval Postgraduate School, Monterey, Ca., September 1981.
10. Beelby, M.H., and Ulrich, H.G., "A Study of the Breakdown Mechanism of AISI 304 SS, AISI 2024 Aluminum and Various Titanium Coatings," MS Thesis, Naval Postgraduate School, Monterey, Ca., December 1981.
11. Naval Research Lab Report 7728, "Response of Materials to Laser Radiation: A Short Course, by Schriempf, J.T., p. 11, 10 July 1974.
12. Chun, M.K., and Rose, K., "Interaction of High Intensity Laser Beams with Metals," Journal of Applied Physics, v. 41(2), p. 614-620, 1970.
13. Ready, J.F., Effects of High Power Laser Radiation, p. 116, Academic Press, 1977.

14. Randall, C. and DeGroot, J.S., "Effect of Crater Formation on the Absorption of Focused Laser Light," Physics Review Letter, v. 42(3), p. 179-182, January 1979.
15. Hughes, T.P., Plasmas and Laser Light, p. 281, John Wiley and Sons, 1975.
16. Anthes, J.P., Palmer, M.A., Gusinow, M.A., and Matzen, M.K., "Absorption of Laser Radiation by Al, Fe, and Al Planar Metallic Targets," Applied Physics Letter, v. 34(12), p. 841-843, June 1979.
17. Kaganov, M.I., Lifshitz, I.M., and Janatarov, L.V., "Relaxation Between Electrons and the Crystalline Lattice," Soviet Physics-JETP, v. 4, p. 173-178, March 1957.
18. Harrach, R.J., "Analytical solutions for laser heating and burnthrough of opaque solid slabs," Journal of Applied Physics, v. 68(6), p. 2370-2383, June 1977.
19. Metz, S.A., Hettche, L.R., Stegman, R.L., and Schriempf, J.T., "Effect of beam intensity on target response to high intensity pulsed CO₂ laser radiation," Journal of Applied Physics, v. 46(4), p. 1634-1642, April 1975.
20. McKay, J.A., Bleach, R.D., Nagel, D.J., and Schriempf, J.T., "Pulsed CO₂-laser interaction with aluminum in air," Journal of Applied Physics, v. 50(5), p. 3231-3240, May 1979.
21. Marcus, S., Lowder, J.E., and Mooney, D.L., "Large-spot thermal coupling of CO₂ laser radiation to metallic surfaces," Journal of Applied Physics, v. 47(7), p. 2966-2968, July 1976.
22. Maher, W.E., and Hall, R.R., "Experimental coupling of laser beams," Journal of Applied Physics, v. 49(4), p. 2254-2261, April 1978.
23. Ready, J.F., Effects of High Power Laser Radiation, p. 188, Academic Press, 1977.
24. Ibid, p. 138.
25. Harrison, D.E., and Neighbors, J.R., Laser Effects Handbook, 3. Laser Absorption Wave phenomena, p. 8-10, Naval Postgraduate School Technical Report, December 1975.
26. Gregg, D.W., and Thomas, S.J., "Momentum transfer produced by focused laser giant pulses," Journal of Applied Physics, v. 37(7), p. 2787-2789, June 1966.
27. Chen, F.F., Introduction to Plasma Physics, p. 1, Plenum Press, 1977.
28. Cooper, A.H., and Crittenden, E.C., Laser Physics and Applications to High Energy Lasers, p. 65, Classroom Notes, Naval Postgraduate School, Monterey, Ca., Summer 1981.
29. Zweigenbaum, S., and Gazit, Y., and Komet, Y., "Momentum Measurements of Laser Produced Plasma," Plasma Physics v. 19, p. 1035-1042, 1977.

30. Harrison, D.E., and Neighbors, J.R., Laser Effects Handbook, 3 Laser Absorption Wave Phenomena, p. 8-10, Naval Postgraduate School Technical Report, December 1975.
31. Hettche, L.R., Tucker, T.R., Schriempf, J.T., Stegman, R.L., and Metz, S.A., "Mechanical response and thermal coupling of metallic targets to high intensity 1.06 micron laser radiation," Journal of Applied Physics, v. 47(4), p. 1415-1421, April 1976.
32. Cooper, A.W., and Crittenden, E.C., Laser Physics and Applications to High Energy Lasers, p. 82, Classroom Notes, Naval Postgraduate School, Monterey, Ca., Summer 1981.
33. Hettche, L.R., Schriempf, J.T., Stegman, R.L., "Impulse Reaction resulting from the in-air irradiation of aluminum by a pulsed CO₂ laser," Journal of Applied Physics, v. 44(9), p. 4079-4085, September 1973.
34. Metz, S.A., "Impulse loading of targets by subnanosecond laser pulses," Applied Physics Letters, v. 22(5), p. 211-213, March 1973.
35. Culham Laboratory (UKAEA) Report CLM-P 573, "Plasma-Surface Interactions in Tokamaks," by McCracken, G.M., and Stott, P.E., 1979.
36. Nedospasov, A.V., and Petrov, V.G., "Model of the Unipolar Arc on a Tokamak Wall," Journal of Nuclear Materials, v. 76-77, p. 490-491, September-October 1978.
37. Schwirzke, F., Beelby, M.H., and Ulrich, K.G., Basic Mechanisms that Lead to Laser Target Damage, Naval Postgraduate School Technical Report, October 1981.
38. Chen, F.F., Introduction to Plasma Physics, p. 10, Plenum Press, 1977.
39. Davis, J.D., "Self Generated Magnetic Fields Produced by Laser Bombardment of a Solid Target," MS Thesis, Naval Postgraduate School, Monterey, Ca., 1971.
40. Brooks, K.M., "An Investigation of Early Disturbances Found in Association with Laser produced Plasmas," MS Thesis, Naval Postgraduate School, Monterey, Ca., 1973.
41. Johnson, B.C., "Induced Evaporation of Metal from an Aluminum Surface by a Normal Pulse Neodymium Laser," MS Thesis, Naval Postgraduate School, Monterey, Ca., 1979.
42. Schwirzke, F., Bunshah, R.F., and Taylor, R.J., The Observation of Unipolar Arcing Damage on Stainless Steel and TiC Coatings on Stainless Steel, paper presented at the International Conference on Metallurgical Coating, San Francisco, Ca., 6-10 April 1981.
43. Callahan, D.J., "Laser Plasma Particle Velocities," MS Thesis, Naval Postgraduate School, Monterey, Ca., 1976.

INITIAL DISTRIBUTION LIST

	No. Copies
1. Defense Technical Information Center Cameron Station Alexandria, Virginia 22314	2
2. Library, Code 0142 Naval Postgraduate School Monterey, California 93940	2
3. Deputy Under Secretary of the Army for Operations Research Room 2E261, Pentagon Washington, D.C. 20310	2
4. Department Chairman, Code 61Dy Department of Physics Naval Postgraduate School Monterey, California 93940	1
5. Assoc. Professor F.R. Schwirzke, Code 61Sw Department of Physics Naval Postgraduate School Monterey, California 93940	3
6. Professor A.W. Cooper, Code 61Cr Department of Physics Naval Postgraduate School Monterey, California 93940	1
7. CPT Robert M. Metheny 429 Fiddlers Green Dover, Delaware 19901	2

DATTE
ILME